Journal of New Technology and Materials
JNTM
Vol. 03, N°01 (2013) 08-11

OEB Univ. Publish. Co.

# Polymer coated quartz crystal microbalance sensors for the detection of volatile organic compounds

*Ali BOUGHAROUAT[1], Azzedine BELLEL[1], Salah SAHLI[2], Yvan SEGUI[3] and Patrice RAYNAUD[3]*
*Laboratoire des Etudes de Matériaux d'Electronique pour Applications Médicales (LEMEAMED),*
*Faculté des Sciences de l'Ingénieur, Université Mentouri de Constantine*
*[1]Laboratoire de Microsystèmes et Instrumentation (LMI), Faculté des Science de l'Ingénieur,*
*Université Mentouri de Constantine*
*[2]Laboratoire Plasmas et Conversion d'Energie (LAPLACE), Université Paul Sabatier,*
*118 route de Narbonne - 31062 Toulouse-France*
** tel: 00 213 079632647, email : ali_boug@live.fr*

*Received: February 18, 2012, revised: January 02, 2013, accepted: April 10, 2013*

***Abstract***

*In this work, plasma polymerization of tetraethoxysilane (TEOS) has been used for producing QCM chemical sensors. The sensor was exposed towards the methanol and chloroform molecules. The measured isotherms on modified QCM electrode showed a good reproducibility and reversibility. Generally, the frequency shift (Δf) of QCM increases linearly with the vapor concentration. The evolution of sensor response showed clearly an improvement of the QCM sensibility. However, the film elaborated from 50% of TEOS and 50% of $O_2$ was found to be significantly more sensitive than film deposited from high proportion of oxygen due to dense structure. Concerning the selectivity, the results revealed a good affinity of the layer to methanol molecules. Fourier transform infrared spectroscopy (FTIR) analysis showed that VOCs molecules interact via hydrogen bonding due to the presence of the –OH group in the elaborated layers.*

***Keywords:*** *Quartz crystal microbalance; TEOS film; Volatile organic compounds; sensor*

## 1. Introduction

The detection of volatile organic compounds (VOCs) in environmental protection, health care and industrial processing has been a subject for research and development over the last decades. Alcohols such as methanol and ethanol are used in many workplaces and laboratories, medicine and food industry [1].The development of sensors with selectivity, rapidly, reliability and reproducibility to VOCs becomes more interest. A number of electronic devices and chemical sensors based on the use of different polymer coatings such as, mass sensitive quartz crystal microbalance (QCM) and surface acoustic wave (SAW) devices have been developed. Amongst the various types of chemical sensors, there is a considerable interest in QCM [2–3] for detection of VOCs. Quartz crystal microbalance (QCM) sensors coated with various sensing films have been useful for gas/vapor detection and analysis [4]. Polymers are widely used as chemically sensitive coating materials on quartz crystal electrodes and are particularly suitable for detecting VOCs, because of the ability of the polymer to sorb vapour reversibly. The chemical structure and physical properties of polymeric coatings and the nature of interaction between polymer coatings and vapour molecules determine the selectivity, sensitivity, signal kinetics and reversibility of the sensors [5]. QCM is extremely sensitive to mass change. The surface of a quartz crystal electrode is coated with a sensitive polymeric material, capable of interacting with the environment of interest and able to adsorb vapour reversibly [6]. The changes in mass ($m'$) of the polymer film can be measured by the oscillating frequency of the quartz electrode. The frequency change ($\Delta f$) to the mass loaded is calculated from Sauerbrey equation [7]:

$$\Delta f = -\left(\frac{2 f_0^2}{\sqrt{\rho_Q \mu_Q}}\right) m'$$

Where $f_0$ (Hz) is the natural frequency of the quartz crystal, $\rho_Q$ is the quartz density (2.649 g cm $cm^{-3}$) and $\mu_Q$ is the shear modulus (2.947×1010 $N/m^2$). In this work, a simple coating method has been used for producing QCM chemical sensors. The method is based on plasma polymerization of TEOS (PPTEOS). The sensor was exposed towards a wide range of VOCs molecules (polar and non polar), such as methanol and chloroform. The paper presents results on the effect of some discharge parameters on sorptive properties of the coated QCM. We investigated the correlation between the interaction of the analyte with the sensitive layer and the chemical structures of the elaborated layers by means of Fourier transform infrared spectroscopy (FTIR) analysis.

## 2. Experimental

### 2.1. Chemical products and instrumentation

Tetraethylorthosilicate (TEOS) was purchased from Merck and used without further purification. The response of the sensor was tested using methanol and chloroform as the analyte species. Six megahertz, AT-cut QCM with polished gold electrodes (diameter 5 cm) were purchased from International crystal Manufacturer (ICM). The frequency change of the sensor (adsorption measurements) was monitored by QCM measurement equipment.

### 2.2. Polymeric film production

TEOS thin films were deposited using plasma enhanced chemical vapor deposition (PECVD) at low frequency power from pure vapor of TEOS or diluted with oxygen. The power during the polymerization was controlled by a 19 kHz generator. The system consisted of a bell-jar chamber (310 mm diameter, 450 mm high), a pair of parallel symmetrical electrodes (120 mm diameter) separated by a distance of 2.5 cm, vacuum system (composed of Alcatel primary pump) and a monomer inlet system. The pressure in the reactor was monitored by a pressure measurement system (Pirani). Substrates were placed in the grounded lower electrode and the reactor chamber was pumped down to 1 Pa in few minutes. The plasma polymerized films were deposited simultaneously on QCM and on intrinsic silicon wafers for FTIR analysis. Chemical structure and composition of PPTEOS films were characterized by FTIR spectroscopy. All spectra were acquired in absorbance mode in the 400-4000 $cm^{-1}$ range using a Nicolet Avatar 360 FTIR spectrometer. The film thickness was measured using a Tencor profilometer.

### 2.3. Measurement systems of the QCM gas sensors

The experimental set-up is shown in Fig. 1. Organic vapor was generated by continuously heating the solution and are introduced to the testing cell by pressure difference. An automatic mass flow controller monitored the target analyte gas concentrations that were fed to the chamber and upon attaining the desired concentration, the shift frequency was simultaneously recorded and the data were transferred to a computer via RS232 interface. Between measurements, the chamber was evacuated to desorb analyte.

## 3. Results and discussion

### 3.1. Reproducibility and reversibility of the sensor

To investigate the reproducibility of the sensor, the response signals of QCM sensors coated with 693 nm layers thickness, deposited from pure TEOS exposed to methanol and chloroform vapors at concentration of 300 ppm were recorded. The sensor was repeated for three times to insure a good reversibility and reversibility Fig.2. After reaching steady state, the film was exposed to dry air until full desorption of the crystal was obtained and it was then exposed to previously used analyte concentration. Moreover, the sensor is found to be reasonably selective and significantly sensitive to methanol vapor than the chloroform vapor.

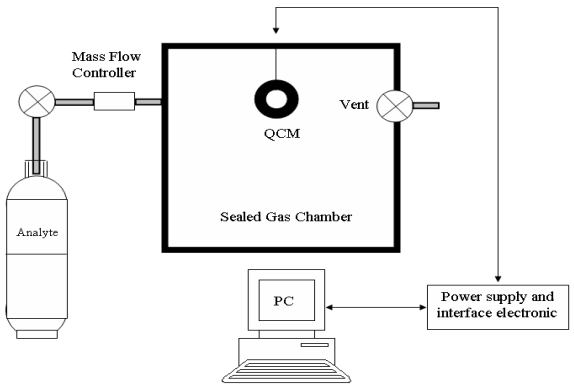


Figure 1. A schematic diagram of QCM experimental cell.

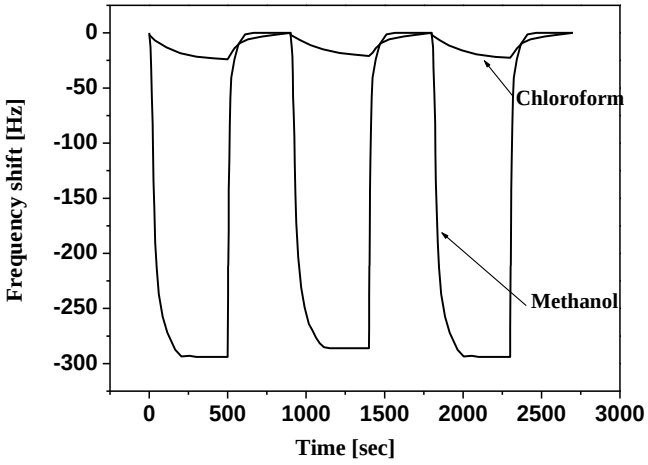


Figure 2. Reproducibility and reversibility of coated QCM electrode when exposed to organic vapors

### 3.2. Coating the electrode of QCM with TEOS/$O_2$ film for organic vapor sensing

During films deposition, the partial pressure of TEOS/$O_2$ and discharge power were kept constant equal to 0.4 mbar and 8 W, respectively. The proportion of oxygen in the mixture was varied from 0 % to 80 %. The QCM sensors coated with 693 nm layers thickness was exposed to methanol and chloroform vapors with various concentrations. Fig. 3 presents the plots of shift frequency ($\Delta f$) as a function of analyte concentration for different oxygen proportion in the mixture. We observe over the whole explored domain of concentrations a good linearity of the sensors responses for both virgin and coated quartz. Moreover, it clearly noticed that the use of a thin PPTEOS film deposited on quartz crystal improves considerably the sensibility of the sensor. For a concentration of methanol of about 250 ppm, the shift frequency recorded on virgin quartz is in the order of 5 Hz. This later value passes to about 250 Hz when the QCM electrode is functionalized with pure TEOS film. This improvement of the sensitivity can be explained either by an increase of the surface adsorption sits of the coated electrode and\or by the physico-chemical

properties of the elaborated layer. This variation of the sensitivity of the QCM with increasing target concentration suggests the existence of a diffusion process of the organic molecules into the bulk of the coating and the increase in film thickness would encourage at first the multiplication of the absorption sites resulting in increased sensitivity of the QCM [8]. For film elaborated from 50% of oxygen and 50% of TEOS, the shift frequency increases significantly to reach a value of about 900 Hz when the sensor was exposed towards 250 ppm. The sensibility improvement of the coated QCM exceeds 180 times the sensibility recorded on virgin quartz crystal. However, we notice that beyond a certain proportion of oxygen in the mixture, the sensitivity decreases significantly. For films elaborated with 80 % of oxygen in the mixture, the response towards 250 ppm of methanol vapors falls to reach 160 Hz, but remained still higher than recorded on virgin quartz crystal. The deposited films became inorganic in character with $SiO_x$ as type chemical composition closer to thermal silica (vitreous, more rigid, are less permeable).

In fig 3b, we notice that the sensitivity to chloroform molecules is much lower than that recorded for the methanol molecules: for 250 ppm of chloroform, the frequency shift is only 20 Hz for quartz coated with pure TEOS film and hardly exceeds 43 Hz when the film elaborated from 50% of oxygen and 50% of TEOS. This difference in sensitivity of quartz covered with the same film thickness and same proportion of oxygen in the mixture can explained by the difference in the molar weight between methanol and chloroform: The molecules of chloroform having a molar weight much more important than that of methanol molecules which have much difficulty to pass through the pores existing in the thin films.

The infrared spectra obtained for different percentages of oxygen in the mixture TEOS/$O_2$ are shown in Fig.4. We notice that for strong proportions of oxygen (80%) the recorded infrared spectrum becomes close to that of thermal silica with its three principal peaks attributed to SiOSi biding group around 400, 800 and 1070 $cm^{-1}$ [9]. Indeed, we observe a total disappearance of the peaks assigned to the element carbon. For film deposited with 50% of oxygen, the $CH_n$ group (2962 $cm^{-1}$) appears with low and we observe a total disappearance of the SiH group (2250 $cm^{-1}$). Table 1 shows the variation of peak intensities ratio of $CH_n$ and SiOH relative to SiOSi peak. With 50% of oxygen, the small decease of $CH_n$ peak is compensated by an increase of hydroxyl groups. A low dense film structure with high proportion of hydroxyl groups promote gas sorption, which is consistent with large sorption capacity of the film elaborated with 50% of $O_2$.

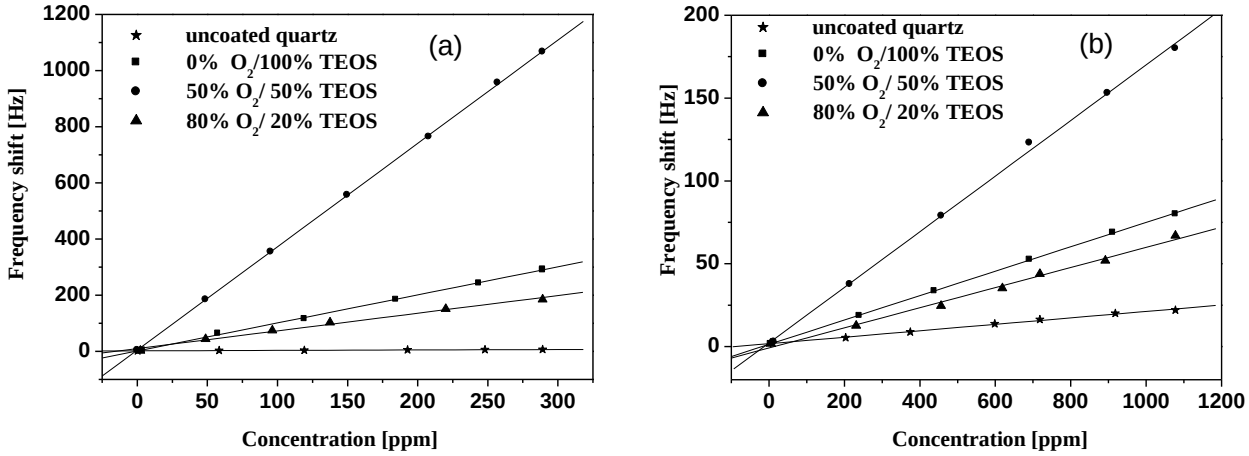


Figure 3. Variation of shift frequency with the concentration of: (a) methanol and (b) chloroform for different oxygen proportion

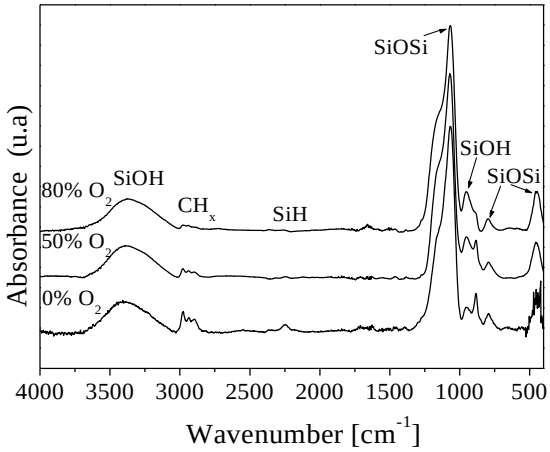


Figure 4. FTIR spectra of the deposited layers elaborated from a mixture of TEOS and oxygen

| Proportion of oxygen [%] | Peak ratio SiOH / SiOSi | Peak ratio $CH_n$ /SiOSi |
|---|---|---|
| 0 | 0.13043 | 0.08261 |
| 50 | 0.15092 | 0.03736 |
| 80 | 0.14384 | 0.01712 |

Table.1 Variation of the SiOH and $CH_n$ relative peak intensity as a function oxygen proportion in the mixture.

## 4. Conclusion

In case of coated QCM electrode with a sensitive layer elaborated from pure vapor of TEOS, the evolution of sensor response showed clearly an improvement of the sensor sensibility for both types of analyte. The frequency shifts versus analytes concentrations exhibited satisfactory linear relationship. The results showed that smaller molar weight VOC molecules are more absorbed than greater molar weight VOC molecules indicating a strong affinity of PPTEOS film for methanol gas. Film elaborated from 50% of TEOS and 50% of $O_2$ was found to be significantly more sensitive than film deposited from high proportion of oxygen due to dense structure. FTIR analysis suggests that the presence of $CH_n$ groups in the film structure (which increases the film microvoides) and OH groups (which provide a main source for hydrophylic capability to interact with foreign molecules) increase the gas sorption capacity of the elaborated layer.

## References


[1] G. Ziem, J. Metamney, *Environmental Health Prospectives* 105 (1997) 417.

[2] G.J. Price, A.A. Clifton, V.J. Burton, T.C. Hunter, "Piezoelectric chemical sensors based onmorpholine containing polymers", *Sens. Actuators B: Chem.* 84 (2002) 208.

[3] N.E. Agbor, M.C. Petty, A.P. Monkman, "Polyaniline thin films for gas sensing", *Sens. Actuators B* 28 (1995) 173.

[4] Bartosz Wyszynski, Agustin Gutierrez Galvez, Takamichi Nakamoto, "Improvement of ultrasonic atomizer method for deposition of gas-sensing film on QCM", *Sens. Actuators B* 127 (2007) 253–259

[5] Mohamad M. Ayad, Gad El-Hefnawey, Nagy L. Torad, "Quartz crystal microbalance sensor coated with polyaniline emeraldine base for determination of chlorinated aliphatic hydrocarbons", *Sens. Actuators B: Chem.* 134 (2008) 887–894

[6] G.G.Wallace, G.M. Spinks, L.A.P. Kane-Maguire, P.R. Teasdale, "Conductive Electroactive Polymers: Intelligent Materials Systems", second ed., CRC Press, Boca Raton, 2003.

[7] G. Sauerbrey, "The use of quartz oscillators for weighing thin layers and for microweighing", *Z. Phys.* 155 (1959) 206.

[8] Jennifer UBRIG, "Encapsulation de dispositifs sensibles a l'atmosphère par des dépôts couches minces élaborés par PECVD", Doctorat thesis, Polytechnic school, 28 November 2007,

[9] K. Kim, D. Kwon, G. S. Lee, "properties of low dielectric constant fluorinated silicon oxide films prepared by plasma enhanced chemical vapor deposition ", *Thin Solid Films* 332 (1998) 369-374.

Journal of New Technology and Materials
JNTM
Vol. 03, N°01 (2013) 12-17

OEB Univ. Publish. Co.

# A comprehensive nonlinear model for GaAs MESFET transistor

*S. Mellal, C. Azizi, M. Zaabat, T. Ziar, C. Kaddour and M. Azizi*
*Faculty of Exact sciences and natural and life sciences*
*Active Devices and Materials Laboratory*
*Larbi Ben M'Hidi university, Oum El Bouaghi -Algéria-*
*saida_mellal@yahoo.fr*

*Received: March 04, 2012, revised: November 14, 2012, accepted: November 24, 2012*

***Abstract***

*An analytical two-dimensional (2D) model to accurately predict the channel potential and electric field distribution in sub-micron GaAs MESFET based on (2D) analytical solution of Poisson's equation using superposition principle is presented. The results so obtained for current voltage characteristics, Transconductance and drain conductance, are presented and validated against both experimental I-V curves and various Models of the submicron MESFET GaAs. The model is then extended to predict the effects of parasitic resistances Rs and Rd, carriers mobility according to the electric fields and the edges effects on the performance. This model will allow more significant simulation of the component characteristics, with a precision improved for various conditions of Schottky barrier.*
***Key words:*** *MESFET- GaAs ; Submicrom nonlinear model ; comparative study*
*PACS: 85.30.TV*

## 1. Introduction

The field-effect transistor to Schottky gate on gallium arsenide says GaAs MESFET is a basic component in the telecommunication systems such as cellphones, computers and in the majority of microwave apparatuses which needs components being able to operate at more high frequencies, in order to obey the desires for the new generations. In this context, a simple and an accurate analytical two-dimensional (2D) model for GaAs MESFET is presented. In modelling the short channel effects in a short gate length MESFET, the 2D Poisson's equation satisfying different surface boundary conditions has been solved to get 2D electrostatic potential and electric field distribution.

The solution of Poisson's equation is accomplished by a technique proposed by Ratnakumar and Meindl [1]. The closed form analytical expressions for channel potential and electric field are derived and the results so obtained are approved by a comparative study drawn up with the experimental results, as well as with three different models (Materka, Mc Camant and Ahmed) [2]. The effect of reducing the gate length on the device output characteristics has also been studied. The important parameters for the modelling of drain current are calculated which provide the foundation for an accurate model. The resulting current-voltage (I-V) characteristics, Transconductance $g_m$ and drain conductance $g_d$ shows good agreement with the experimental curves.

## 2. MESFET models

To describe the operation and the characteristics of the field-effect transistors, various models were developed by different authors [3] rest on analytical equations for the simulation of the current Ids=f(Vgs,Vds). And as comparison us, we have selected three models, Materka, McCamant and Ahmed; who rest on the expressions appearing afterwards for each model.

### 2.1. Materka Model ( 1983) [11]

The current source $I_{ds}$ controlled by the voltages (Vgs,Vds) is described by the formula (1) [11].

$$I_{ds} = I_{dss}\left[1-\frac{V_{gs}}{V_T+\gamma V_{ds}}\right]^2 \times tanh\left(\frac{\propto V_{ds}}{V_{gs}-V_T-\gamma V_{ds}}\right) \qquad (1\text{-}1)$$

Where: $I_{dss}$ , $V_T$ , $\propto$ and $\gamma$ are the model parameters.
($\propto$), describe the transition from the linear region to the saturation region due to velocity overshoot.
($\gamma$), is used to simulate effective threshold voltage displacement as a function of $V_{ds}$.
By derivation the drain current with respect to drain-source voltage and gate-source voltage individually, transconductance and output conductance are obtained and they are formulated below:

$$g_m = 2I_{ds}\left[\frac{\sinh\left(\frac{2\propto V_{ds}}{V_{gs}-V_T-\gamma V_{ds}}\right)-1}{(V_{gs}-V_T-\gamma V_{ds})\sinh\left(\frac{2\propto V_{ds}}{V_{gs}-V_T-\gamma V_{ds}}\right)}\right] \qquad (1\text{-}2)$$

$$g_d = 2I_{ds}\left[\left(1+\frac{1}{V_{gs}-V_T-\gamma V_{ds}}\right)+\frac{\gamma V_{gs}}{(V_T+\gamma V_{ds})(V_{gs}-V_T-\gamma V_{ds})}\right] \qquad (1\text{-}3)$$

### 2.2. McCamant Model (1990) [5]

In 1990, McCamant et al. [5] proposed an improved FET model for the device simulator [McCamant-1990] in which the variation of $I_{ds}$ is given by (2)
Where: $I_{ds0}$ , $V_T$ , $\propto, \delta$ and $\gamma$ are the model parameters

$$I_{ds} = \frac{I_{ds0}}{1+\delta V_{ds} I_{ds0}} \quad (2\text{-}1)$$

With:

$$I_{ds0} = \begin{cases} \beta(V_{gs} - V_T - V_{ds})^n \left[1 - \left(\frac{\alpha V_{ds}}{3}\right)^3\right] for\ 0 < V_{ds} < \left(\frac{3}{\propto}\right) \\ \beta(V_{gs} - V_T - V_{ds})^n \qquad for\ V_{ds} \geq \left(\frac{3}{\propto}\right) \end{cases} \quad (2\text{-}2)$$

Here n is an integer

$$g_m = \left\{ \frac{n I_{ds0}}{(1+\delta V_{ds} I_{ds0})(V_{gs} - V_T - V_{ds})} \qquad for\ 0 < V_{ds} \right. \quad (2\text{-}3)$$

$$g_d = \left\{ \frac{I_{ds0}\left[\propto\left(1-\frac{\propto V_{ds}}{3}\right)^2\right]}{(1+\delta V_{ds} I_{ds0})^2\left[1-\left(1-\frac{\propto V_{ds}}{3}\right)^3\right]} - \frac{\gamma n I_{ds0}}{(1+\delta V_{ds} I_{ds0})^2 (V_{gs} - V_T - V_{ds})} - \right.$$
$$\delta {I_{ds}}^2 \qquad for\ 0 < V_{ds} < \left(\frac{3}{\propto}\right) \quad (2\text{-}4)$$

$$g_d = \left\{ -\frac{\gamma n I_{ds0}}{(1+\delta V_{ds} I_{ds0})^2 (V_{gs} - V_T - V_{ds})} - \delta {I_{ds}}^2 \quad for\ V_{ds} \geq \left(\frac{3}{\propto}\right) \right. \quad (2\text{-}5)$$

### 2.3. Ahmed Model ( 1997 ) [2,3]

The Kacprzak-Materka model, which simulates the I-V characteristics of large signal devices, has been modified by Ahmed to predict the behaviour of submicron devices. In this modification the concept of a shift in threshold voltage has been introduced. It has been shown in the formula (3) that without taking into account the shift which is caused by the submicron geometry it is not possible to predict the device characteristics.

$$I_{ds} = I_{dss}\left[1 - \frac{V_{gs}}{V_T + \Delta V_T + \gamma V_{ds}}\right] \times \tanh(1 + \lambda V_{ds}) \quad (3\text{-}1)$$

With: $\Delta V_T = \frac{4a}{3L_g}$ (3-2)

$$g_m = \frac{2(A-1) I_{ds}}{A V_{gs}} \quad \text{with:} \quad A = 1 - \frac{V_{gs}}{V_T + \Delta V_T + \gamma V_{ds}} \quad (3\text{-}3)$$

$$g_d = \frac{\lambda I_{ds}}{1+\lambda V_{ds}} + 2 I_{ds}\left[\frac{\gamma (A-1)^2}{A V_{gs}}\right] + \frac{\alpha}{\sinh(2\alpha V_{ds})} \quad (3\text{-}4)$$

### 3. Proposed model formulation

One of the drawbacks of the previous models is their relative failure to capture the effects of a modulation of the drain-source voltage $V_{ds}$. It is with this consideration in mind that we pose the following model of MESFET with a short gate length.

The channel potential cannot be entirely controlled by the gate bias and will be shifted by the penetration of lateral electric field. Therefore there are two factors which play an important role for the short channel effects [6] in the submicron MESFET. One is the lateral field distribution at the sidewall of the gate edge and the other is the efficiency of the gate metal in terminating the lateral electric field.

Thus solution for 2D Poisson's equation satisfying suitable boundary conditions is required to model the short channel effect. A simplified self aligned GaAs MESFET is shown in Fig.1 [10, 12], over which Poisson's equation is solved for the potential distribution $Vc(x, y)$, where '**L**' is the gate length. '**a**' is the thickness of the active layer.

In order to avoid the problems resulting from different surface boundary conditions, the n-GaAs layer is assumed to contact directly to the gate metal, and the absorption of electric field by the depletion charges near the source/drain is not taken into account.

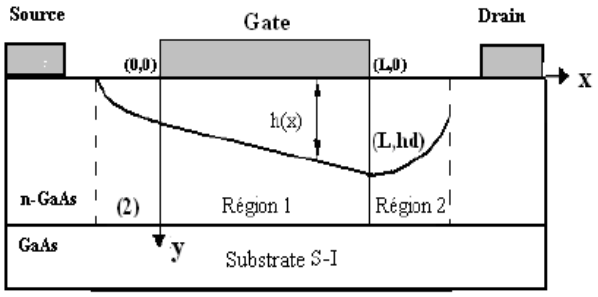


Figure 1. Schematic diagram of a self-aligned GaAs MESFET

### 3.1. 2D analytical model

The 2D Poisson equation for the depletion region, assuming complete depletion, is

$$\nabla^2 V_c(x,y) = \frac{d^2 V_c}{dx^2} + \frac{d^2 V_c}{dy^2} = -\frac{q}{\varepsilon_s} N_d(y) \quad (4)$$

$Vc(x,y)$ is the electrostatic potential, q is electron charge, εs is the dielectric permittivity of GaAs semiconductor, Nd (y) is the doping concentration, The doping is considered to be uniform, with the doping concentration Nd .

According to the superposition technique [1], (4) can be resolved as

$$V_c(x,y) = V(y) + V_l(x,y) \quad (5)$$

Where V(y) is the solution of Poisson's equation (6) for the MESFET structure in one dimension along y-axis near the mid of the channel (region 1). It is this potential profile that would result if the device were completely unaffected by lateral electric fields from the source and the drain; Vl(x, y) is the solution of 2D Laplace (7), it represents the voltage brought by the overflow of the depletion region side source and side drain (region2):

$$\frac{d^2V}{dy^2} = -\frac{q}{\varepsilon_s}N_d \quad (6)$$

$$\frac{d^2V_l}{dx^2} + \frac{d^2V_l}{dy^2} = 0 \quad (7)$$

To solve for $V(y)$ following boundary conditions are used

$$V(y)|_{y=0} = V_{bi} - V_g \quad (8)$$

$$\left.\frac{dV(y)}{dy}\right|_{y=a} = 0 \quad (9)$$

Where $V_{bi}$ is the schottky-barrier built-in potential, $V_g$ is the applied gate-source voltage. Using (8) and (9) in (6), the solution of 1D Poisson's equation is :

$$V(y) = \frac{-qN_d y^2}{2\varepsilon_s} + \frac{qN_d ay}{\varepsilon_s} + V_{bi} - V_g \quad (10)$$

Boundary conditions for $V_l(x,y)$ are derived from the boundary conditions for $V_c(x,y)$, through (5) and (10) as [4].

$$V_c(L,y) = V_{bi} + V_{ds} \ , V_l(L,y) = V_{bi} + V_{ds} - V(y)$$

$$\frac{dV_c(x,a)}{dy} = 0 \quad , \quad \frac{dV_l(x,a)}{dy} = 0 \ , \frac{dV_c(L,a)}{dx} = E_s$$

Where, $\boldsymbol{V_{ds}}$ is the applied drain-source voltage and $\boldsymbol{Es}$ is the saturation electric field.

Applying the standard technique of separation of variables produces a Fourier series solution, only the first Fourier series terms (with coefficient $\boldsymbol{A_1^s}$ and $\boldsymbol{A_1^d}$) are sufficient to represent the potential near the source and drain. Thus the resulting expression for $\boldsymbol{V_l(x,y)}$ is [4]

$$V_l(x,y) = \alpha\left[sinh\big(k(L-x)\big) + sinh(kx)\right]\sin(ky) \quad (11)$$

Where: $k = \frac{\pi}{2a}$

And: $\alpha = \frac{2aE_s}{\pi(\cosh(kl)-1)}$

Following (5), (10) and (11) the expression for the total voltage becomes:

$$V_c(x,y) = \frac{-qN_d y^2}{2\varepsilon_s} + \frac{qN_d ay}{\varepsilon_s} + V_l(x,y) + V_{bi} - V_g \quad (12)$$

The lateral electric field $\boldsymbol{E_x}$ and vertical electric field $\boldsymbol{E_y}$ distribution in the channel can be determined by differentiating (12) with respect to x and y, respectively

$$E_x = \alpha k\left[-cosh\big(k(L-x)\big) + cosh(kx)\right]\sin(ky) \quad (13)$$

$$E_y = \frac{-qN_d}{\varepsilon_s}y + \frac{qN_d a}{\varepsilon_s} + \alpha k\left[sinh\big(k(L-x)\big) + sinhkx\cos ky.\right. \quad (14)$$

### 3.2. Effect of the mobility law

The current-voltage characteristics depend on the variations of the electrons mobility (μ) according to the electric field (E). The choice of a mobility law is important for a correct description of physical phenomena in the submicron gate MESFET's.

The analytical expression of this law that we use is a simplified relation [7] given as follows:

- For the low electric fields: E < Eo

$$\boldsymbol{\mu = 0} \quad (15\text{-}1)$$

- For the electric fields higher than **Eo** : (Eo < E < Em)

$$\boldsymbol{\mu} = \frac{\boldsymbol{\mu_0}}{\left[1+\left(\frac{E-E_0}{E_s}\right)^2\right]^{1/2}} \quad (15\text{-}2)$$

With:

$$E_0 = \frac{1}{2}\left[E_m + (E_m{}^2 - 4E_s{}^2)^{1/2}\right] \quad (15\text{-}3)$$

$Eo$ : is a phenomenological parameter having the dimensions of an electric field

$E_m$: The threshold field, corresponding to the maximum of the overspeed regime.

$E_s$: The critical field for which the speed in linear regime is corresponding to the saturation speed.

### 3.3. Current-voltage characteristics I -V

To calculate the expression of the drain current in function the drain voltage for various values of the gate voltage, we use the following assumptions:

The current in the direction y is neglected; this approximation is valid for short gate devices.

The channel is divided in two regions according to the value of the electric field.

The basic equation used to derive the I-V relationship [8] is given by:

#### - Linear regime

This regime exists as the electric field in the channel is low and the electron mobility is equal to $\boldsymbol{\mu 0}$. Expression of the drain current in this regime can be written as:

$$I_d(V_d,V_g) = \frac{I_p}{V_p}\left\{1 - \sqrt{\frac{V_{bi}-V_g}{V_p}}\right\}V_d \quad (16)$$

Where:

$I_p = \frac{(qN_d)^2 Z\mu_0 a^3}{2\varepsilon L}$ and: $V_p = \frac{qN_d}{2\varepsilon}a^2$

#### - Saturation regime

When the drain voltage increases, the electric field in the channel increases beyond $\boldsymbol{E_0}$ . The electron mobility is given by (15-2).

The saturation current is:

$$I_{dsat} = I_p \left[\frac{1}{3} - \left(\frac{V_{bi}-V_g}{V_p}\right) + \frac{2}{3}\left(\frac{V_{bi}-V_g}{V_p}\right)^{3/2}\right] \quad (17)$$

With: $I_p = \frac{(qN_d)^2 Z\mu a^3}{2\varepsilon L}$

### 3.4. Transconductance and drain conductance

The expression of $I_d$ is used to calculate the two basic parameters of the transistor, which are the transconductance $g_m$ and the channel conductance $g_d$ more commonly known as drain conductance.

The transconductance is the expression of the control mechanism of a transistor: it represents the variation of the current in the channel modulated by the gate voltage at constant drain-source voltage [9].

In the Linear regime

$$g_m = \frac{Z\mu_0}{L}(2\varepsilon qN_d)^{\frac{1}{2}}\left[(V_{bi} - V_g + V_d)^{\frac{1}{2}} - (V_{bi} - V_g)^{\frac{1}{2}}\right] \quad (18)$$

In the saturation regime

$$g_{m_s} = \frac{Z\mu_0}{L}(2\varepsilon qN_d)^{\frac{1}{2}}\left[(V_p)^{\frac{1}{2}} - (V_{bi} - V_g)^{\frac{1}{2}}\right] \quad (19)$$

The conductance reflects the resistance of the channel: it is the variation of the drain current according to the $V_d$ voltage variation, with constant polarization of the gate.

In the Linear regime

$$g_d = \frac{Z\mu_0}{L}(2\varepsilon qN_d)^{\frac{1}{2}}\left[(V_p)^{\frac{1}{2}} - (V_{bi} - V_g + V_d)^{\frac{1}{2}}\right] \quad (20)$$

In the saturation regime

The conductance is perfectly zero, $g_{ds} = 0$ (21)

### 3.5. Influence of parasitic elements

The characteristics that we have presented are those of the internal or intrinsic sizes $(\boldsymbol{I_d, V_d, V_g})$ to obtain the external or extrinsic characteristics of the component $(\boldsymbol{I_{ds}, V_{ds}, V_{gs}})$, it is enough to take into account the effect of parasitic resistances to access of source $\boldsymbol{R_s}$ and drain $\boldsymbol{R_d}$, and also the effect of $\boldsymbol{R_p}$ parallel resistance to the canal on values of the bias voltages **[10]**.

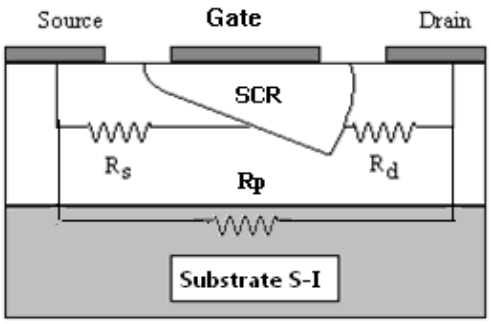


Figure 2. Parasitic resistances in the MESFET GaAs.

To obtain the real expressions of characteristics Ids(Vds, Vgs), it is enough to replace the intrinsic terms by the extrinsic terms in all the preceding relations:

$$\begin{cases} I_d = I_{ds} - (V_{ds}/R_p) \\ V_d = V_{ds} - (R_s + R_d)I_d \\ V_g = V_{gs} - R_s I_d \end{cases} \quad (22)$$

## 4. Results and discussions

In order to validate the characteristics of current I-V, transconductance and conductance of GaAs MESFET transistor witch describe the suggested model and the chosen models, a software of simulation based on the expressions established in the preceding paragraphs is realized in Matlab, as well as the obtained results are represented by curves and are discussed.

### 4.1. Characteristics courant-voltage I-V

The numerical calculation of the drain current according to the polarization voltages calls upon the expressions (16), (17) and (22) for the model suggested thus that the expressions (1), (2) and (3) for the three selected models.

The study was made on a submicron GaAs MESFET transistor which parameters are gathered in table (1):

| **L (µm)** | **a(µm)** | **Z(µm)** | **µo($m^2$/Vcm)** |
|---|---|---|---|
| 1 | 0,153 | 300 | 0,4000 |
| **Nd(At/$m^3$)** | **Vs(m/s)** | **Vbi(V)** | **Vp(V)** |
| 1,17 $10^{23}$ | 3.6 $10^5$ | 0,85 | 1.93 |

Table 1. GaAs MESFET transistor parameters

The figures (3a), (3b), (3c) and (3d) represent the comparison of characteristic *Ids (Vds, Vgs)* measured and calculated using simulation for the four models.

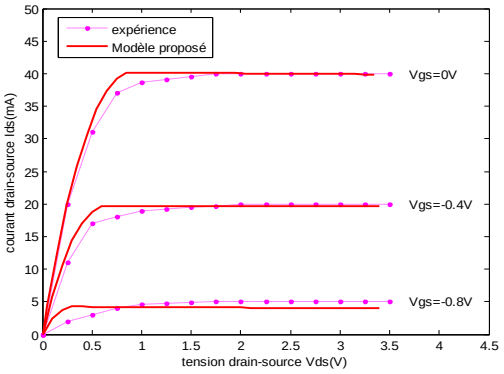


( a )

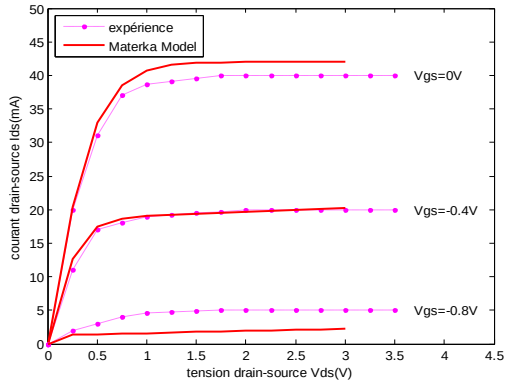


( b )

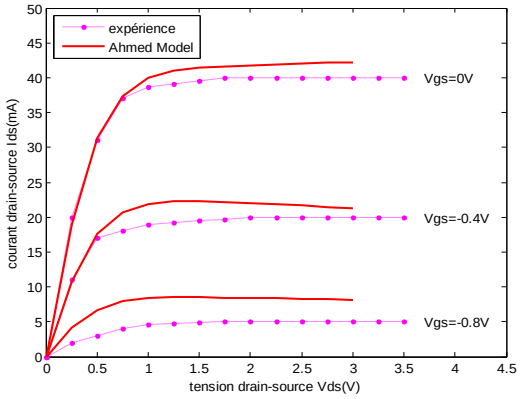


( c )

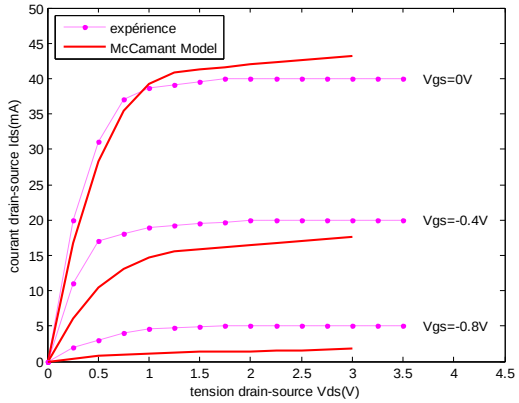


( d )

Figure 3. Variations I-V characteristics of the MESFET 1 transistor according to the model: (a) suggested model, (b) Materka model, (c) Mc Camant model, (d) Ahmed model

The figure (3-a) illustrates **I-V** characteristics of the suggested model and shows that theoretical results and those of the experiment **[8]** have the same behavior towards the tension of drain and coincide well, in particular with the high values of the **Vds** voltage. This shows the good founded of the method. The weak variation observed towards saturation is mainly due to the mobility law used.

The figures (3-b), (3-c) and (3-d) present respectively ***I-V*** characteristics of Materka model , Mc Camant model and Ahmed model, the curves reflect a light shift between the experimental values and the simulated characteristics, in particular to the high values of the $V_{ds}$ voltage, this shows the inaccuracy of these models for the submicron devices. It is mainly about the incapacity of these models to simulate the finished $g_d$ value in the saturation region which is usually observed in the MESFET with short channel.

### 4.2. Transconductance and drain conductance

The variation of $g_m$ and $g_d$ by using the equations of the transconductance and the drain conductance established previously for the four models, in comparison with the experimental data [2], are presented on the figures 4 and figures 5, respectively. The curves show once more the validity of the suggested model and the variation present for the other models in particular in the saturation region.

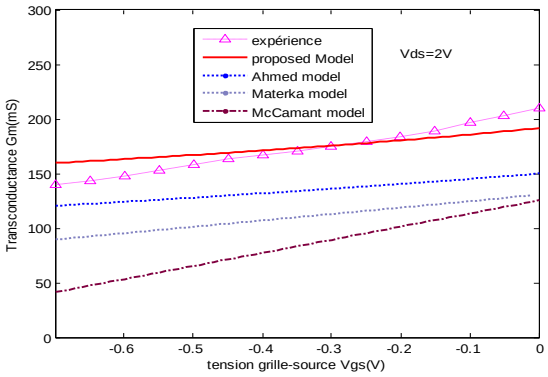


Figure 4. Variation of the transconductance according to the gate voltage for the MESFET

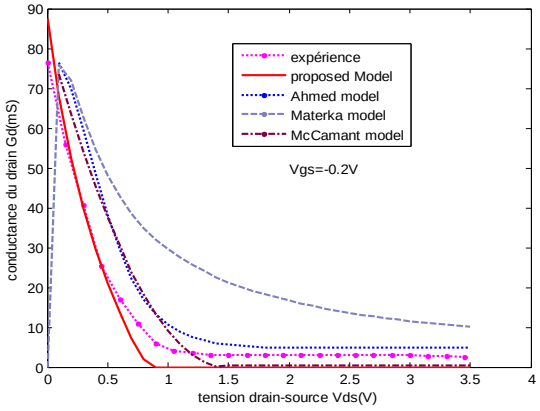


Figure 5. Variation of the conductance according to the drain voltage for the MESFET

### 5. Conclusion

In this paper we have proposed an analytical model of submicron GaAs MESFET based on (2D) solution of Poisson's equation using superposition principle; For developing of the extrinsic characteristics of the component we have introduced the parasitic resistances and edges effects. To check the validity of this model, the I-V

characteristics, transconductance and drain conductance of the MESFET are simulated and compared with three different models of same MESFET. Thy gives similar results; However, there are some differences in the results when compared to the experimental measurements. It has been shown that the proposed model gives improved results at the saturation region, so it represents a good model capable to simulate the characteristics of the MESFET.

## References


[1] K.N. Ratnakumar, J.D. Meindel, Short Channel MOST threshold voltage model, *IEEE J. Solid State Circuits* 17 (1982) 937–947.

[2] Memon N. M. ; Ahmed M. M. ; Rehman F. *Solid-state electronics* vol. 51, no3, 2007.

[3] Noor Muhammad Memon ; Thèse de doctorat ,universite Islamabad October 2008 , Ch. 3.

[4] S.Khemissi, N.Merabtine, C.Azizi, C.Kadour. XIth International Workshop : Symbolic and Numerical Methods, Modeling and Applications to Circuit Design , Tunisia, Oct. 2010.

[5] McCamant,A,J.;McCormack,G.D.; Smith,D.H, *IEEE Transactions* Volume: 38 Issue:6, Jun 1990

[6] Sneha Kabra and all . *Microelectronics Journal* Vol 38, pp 547–555, May 2007.

[7] C.S.Chang, D.Y.Day, *IEEE Trans Electron Devices* Vol 36, N°2, 1989.

[8] C.AZIZI and All . 5th Tunisian International Conference: Sciences of Electronic,Technologies of Information and Telecommunications ,March 22-26, 2009 .

[9] K.Ueno, T.Furutsuka et All International Electron Devices Meeting, Vol 31,pp: 82 – 85, 1985.

[10] S.Khemissi, C Kenzai and all, SPQEO Vol 9 N°2, pp 34- 39, 2006.

[11] D.Resca, J.A.Lonac, *IEEE Trans.* Vol: 58 Issue:4 pp: 719 - 729 , Avril 2010.

[12] S.P.Chin, C.Y.We , *IEEE Trans. Electron Devices* Vol 39, N° 8, pp 1928 – 1937, 1993.

Journal of New Technology and Materials
JNTM
Vol. 03, N°01 (2013) 18-22

OEB Univ. Publish. Co.

# Detection of the Corrosion of Aluminium Alloy by Optical Method

*R. Daïra and B.Boudjema*
*Department of sciences of matter*
*University August 20 1955 of skikda*
*Road of El Hadaiek LP 26*
*Physico Chemistry of Surfaces and interfaces Research Laboratory of Skikda (LRPCSI).*
*ALGERIA*
*daira_radouane@yahoo.fr*

*Received: March 07, 2012, revised: November14, 2012, accepted: November 24, 2012*

***Abstrat***

*The Speckle effect is a discipline with whole share. It is exploited in various scientific fields. On the application plan, it became a very powerful tool for the characterization and the non destructive testing. This technique which makes it possible to control and quantify in real time several parameters such as: the roughness of surface, the vibrations, the constraints, microphone-displacements, the microstructure of surfaces, can be applied, at the same time, with the objects transparent and diffusing, solid or liquids. The development of flexible tools of capture of images to high resolution (camera CCD) coupled to information processing systems, nowadays makes the techniques speckle particularly important and interesting for industrial control. Our work consists in controlling qualitatively and quantitatively the variation thickness extracted the surface of the Duralumin sample (Aluminium alloy) immersed in a Salt water (to 3.5%), by using a camera CCD connected to a computer equipped with a software of image processing PRO-PLUS*

***Key words:*** *DSPI Digital Speckle Pattern Interferometry, Phase Evaluation Method; Phase unwrapping; Non destructive testing, Image processing.*

## 1. Introduction

The speckle effect is the manifestation of the strong space coherence of a source of light. It is observed when one lights an object diffusing by a laser beam. This luminous granularity is not other than the result of the interference of the waves coherent but by chance out of phase (shift of phase) resulting from the object. Consequently, if this shift had been suddenly modified, it means that if surface is deformed, the structure of the speckle would be also modified. By studying the modification of the structure of the speckle (displacement, disappearance or appearance of luminous points), one can go up with one of the parameters (deformation, roughness, microphone-displacement, vibration etc...) of the surface of the object in a qualitative but especially quantitative way. The technique which makes it possible to go up with the parameters quoted above, is digital interferometry speckle. It consists in making the difference or the addition in two figures of fields of speckle before and after having undergone with the object a modification. The result can generate fringes of correlation which correspond exactly to the variation of the state of the object. The present study, consists of controlling qualitatively and quantitatively the variation thickness extracted the surface of a Duralumin sample by interferometry speckle, since the immersion of material in salt solution d until the beginning of the dissolution of metal, while passing by the various stages included in the process of the rupture of the passive film which precedes the pitting. This control is done by collecting the images by a camera CCD connected to a computer equipped with a software of image processing PRO-PLUS [1].

## 2. Theory

Interferometry speckle uses the information of the phase contained in each grain of speckle. To obtain this information of phase, it is necessary to make interfere the wave of speckle with a wave of reference (the device can be assimilated to
The interferometer of Michelson). This requires rather strict conditions on the slope of the wave of reference and the curve of its face of wave. That is to say the image of speckle coded [2, 3, 4]:

$$R + Se^{i\varphi}$$

Either R(x, y) the average amplitude of the wave of reference on the grain to the point (x,y), or S(x, y) that of the wave of speckle and or the difference in average phase between these two waves.
Note: vary by chance from one grain to another because unspecified surface is supposed.
The intensity observed is given by the module to the square of the amplitude [5,6]:

$$I(x,y) = (R + Se^{i\varphi})(R + Se^{-i\varphi}) \quad (1)$$

$$= R^2 + S^2 + 2RS\cos\varphi \quad (1)$$

By posing : $I_0(x,y) = R^2+S^2$
and: $V(x,y) = \frac{2RS}{R^2 + S^2}$
One obtains:

$$I(x,y) = I_0(x,y)(1+V(x,y)\cos\varphi) \quad (2)$$

Will the disturbance of the object create a local dephasing (it means that depend on the point (x,y)) between the wave of speckle and the wave of reference. The intensity is then given by:

$$I_2(x,y) = I_0(x,y)(1+V(x,y)\cos(\varphi+\Delta\varphi) \quad (3)$$

Consequently, the technique applies as follows: one takes an image of the object before disturbance, which gives us $I_1$(x, y). One takes then an image of the object after disturbance, which gives us $I_2$(x,y).

The subtraction of these two images is made pixel by pixel. The result is given by:

$$I_{tot}(x,y) = I_1 - I_2$$

$$= I_0(x,y)V(x,y)[\cos\varphi - \cos(\varphi+\Delta\varphi)] \quad (4)$$

By making a trigonometrically transformation, one finds:

$$I_{tot} = 2I_0 V sin(\frac{\Delta\varphi}{2})sin(\varphi+\frac{\Delta\varphi}{2}) \quad (5)$$

They are fringes of intensity.

Dephasing Δφ on the difference of way optical ΔL depends between the state of reference and the disturbed state, and is expressed as follows [7, 8]:

Δφ=(2π/λ)ΔL = (2π/λ).2Δ(n.e).cosε"(6)

Where « n » is the index of refraction of the medium, « e » the thickness of the extracted layer and « ε" » is the angle of refraction inside the layer.

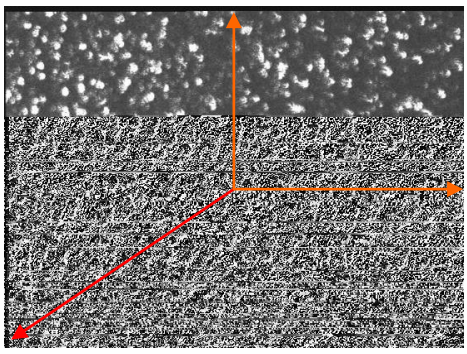

## 3. Principle of the technique

### 3.1. Experimental device

The diagram of the breadboard construction employed to acquire the figures of fields of speckle is represented by figure 1.

Is the source of light used a laser source He-Ne (emitting in the red with λ = 632.8nm), in order to have a length of sufficient coherence and a high brightness. The beam widened by an objective of microscope (OB) of enlargement 10x is filtered spatially (filter of diameter 25 µm) then collimated by a photographic objective ($O.PH_1$)4.5/ 210. The outgoing beam of this last, crosses a first separating cube, which separates it in two parts. A part of the light goes directly on a second separating cube, arrives at the $M_1$ mirror, which it considered on a third separating cube and falls then on the matrix from the CCD. This beam is called beam of reference. The second beam falls on the mirror $M_2$ which it considered on the sample (this one is fixed vertically by its higher end on a metal support using a glue) of Duralumin plunged in a rectangular basin out of glass containing a salt water solution with 3,5%. This beam covers a great part of the sample of dimension 2cm X 1cm. The beam diffused by the sample (called beam object), positioned the plan of capture parallel to, crosses the photographic objective ($O.PH_2$) 4.5/75, then the third cube and is interfered then with the wave of reference on the same matrix of the CCD, connected to a computer making it possible to acquire the images and to digitize them on 256 levels of gray. The images are then sent towards the software to treat them.

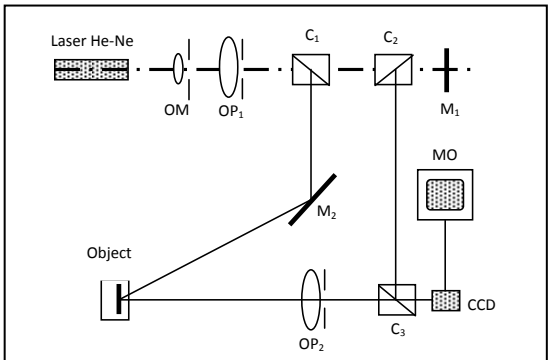


Figure 1. Experimental device for the control of the microstructure of a Duralumin sample plunged in a NaCl solution.

### 3.2. Analyze

Before carrying out the qualitative and quantitative control of the variation thickness extracted from our samples, one takes an initial image with the state of the interference of the two waves of an object plunged in the solution, represented by the equation (2).

Then one takes other images (interferograms) after having immersed the sample during a certain time, and which is represented by the equation (3).

With one Δϕ who varies according to the removed thickness of the sample.

## 4. Results and interpretations

To show the method described previously, one takes image of reference and several images of the same sample immersed in the solution chlorinated to different times: from 2 minutes up to 120 minutes. Figure (2) represents 12 specklogramms, which show the images of each state of variation of the influence of the solution on material to be controlled. These specklogramms is not other than parallel interference rings with a spacing (distance between interference rings) no constant for each image.

On the figure (2), One notices that there is increase in the number of fringes (decorrelation between the fields of speckle), therefore the distance between interference rings « i » decreases. This is explained by the fact that there was a variation of the difference in walk ΔL, therefore formation of a passive film on the surface of the sample. The variation thickness of this film is deduced starting from the equation (6) and the following relation:

i = λ/ΔL.

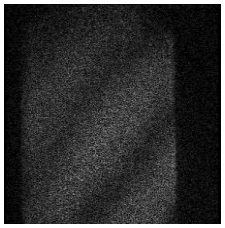

a) Specklogramm taken after 2 min

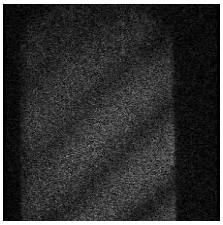

b) Specklogramm taken after 4 min

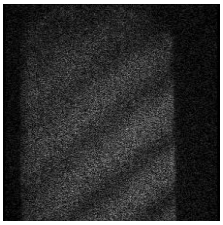

c) Specklogramm taken after 6 min

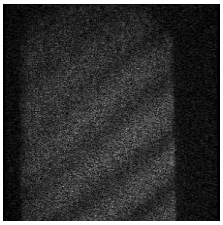

d) Specklogramm taken after 10 min

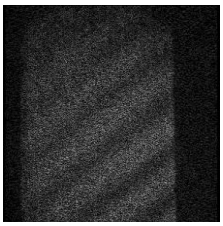

e) Specklogramm taken after 12 min

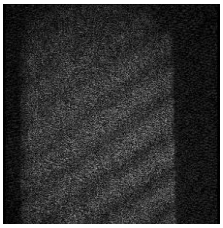

f) Specklogramm taken after 16 min

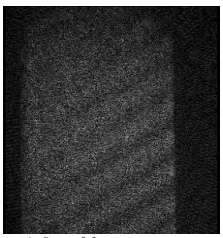

g) Specklogramm taken after 20 min

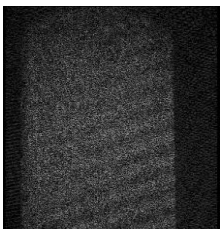

h) Specklogramm taken after 25 min

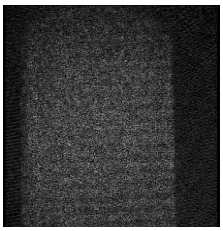

i) Specklogramm taken after 30 min

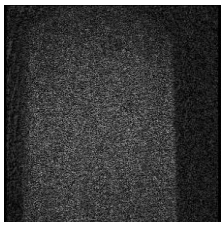

j) Specklogramm taken after 35 min

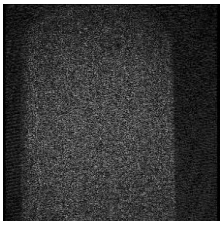

k) Specklogramm taken after 90 min

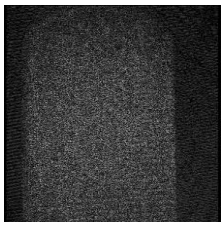

l) Specklogramm taken after 120 min

Figure 2. Representation of specklogramms relating to the states of change of the microstructure of the Duralumin sample plunged in the NaCl solution.

The specklogramms (b), (c), (d), (e), (f) and (g) correspond at the first stage which is the formation of the passive film $Al_2O_3$ with reinforcement starting from the molecules of $H_2O$ (from the point of view chemical or electrochemical, the formation of this film requires at least three stages which correspond to the quoted specklogramms: initial dissolution of the matrix, hydrated oxide formation or $Al_2(OH)_3$ hydroxide then dehydration of this last and obtaining Alumina. (G.Okamoto, T.Shibata, 1978 et C.Vargel,1999).
After the adsorption of Cl on the surface, the passive film will be destroyed according to the following reaction:

$$Al_2O_3 + H_2O \Rightarrow 2AlO_2^- + 2H^+$$

This stage corresponds to the specklogramms (h) and (i), which show a decorrelation of the fringes by the introduction of new fringes. One thus attends a beginning of corrosion. While specklogramms (j), (k), and (l) (preserve the same figure of the object) corresponds at the stage of dissolution of the base metal. Once the dissolved passive film, the base metal is found naked and one can have the possibility of the following reactions:

$$Al \Rightarrow Al^{3+} + 3e^-$$
$$Al^{3+} + H_2O \Rightarrow Al(OH)^{2+} + H^+$$
$$Al^{3+} + 2H_2O \Rightarrow Al(OH)_2^+ + 2H^+$$

Cependant the two harmful reactions which can take place is:
- Formation of chlorides such as:
$Al^{3+} + 3Cl^- \Rightarrow AlCl_3$ (which are soluble)
- And that of $AlOHCl^-$ in solution :
$Al^{3+} + H_2O + Cl^- \Rightarrow AlOHCl^-$ ( soluble also).

the process of formation and dissolution of these two products, will activate the process of the oxidation of the base metal and thus one attends the starting of a piquration.
From these results, one could estimate the variation thickness of passive film formed on metal.

## 5. Detection of the beginning of corrosion by method ESPI

### 5.1. Capture figures of speckle

An initial figure of speckle ($S_0$) of the object after its immersion in the solution of 3.5% of NaCl, is recorded. After 12 minutes of immersion, one moves the piezoelectric one by quantities 0, $\pi/2$, $\pi$, $3\pi/2$ successively. Four figures of speckle of ($S_1$ to $S_4$) corresponding to each shift of phase are recorded.

### 5.2. Treatment of the interferograms

Four interferograms of ($I_1$ to $I_4$) are generated by the calculation of the square of the difference between the figures of speckle of the beginning of the immersion of the object up to 12 min of immersion ( $I_i = (S_i - S_0)^2$, (i = 1-4 ). These operations are carried out using the software Image-Pro Plus.
The analysis of these interferograms will be carried out by the software Fringe Processor 3, from where procedure of calculation of the phase which proceeds according to the following stages.

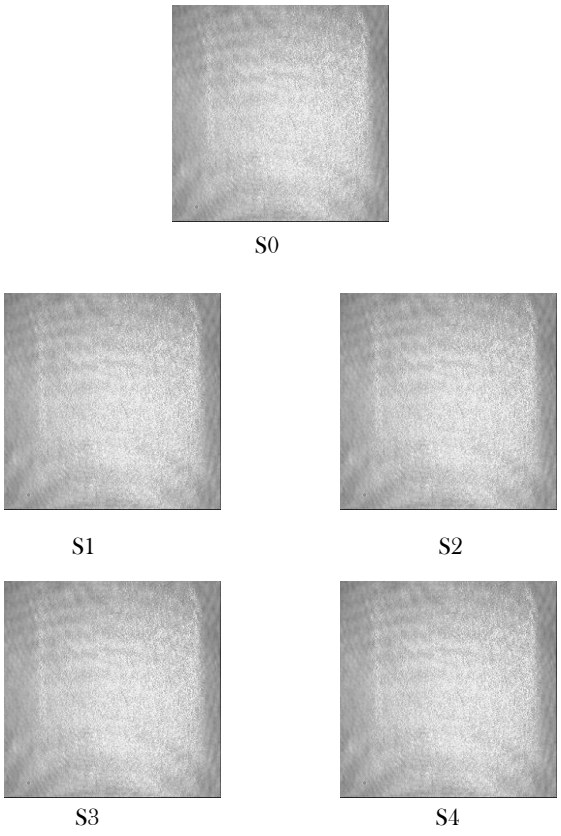


Figure 3. Images of speckle, (S0) image initial, (S1 to S4) images collected after 12 min of immersion.

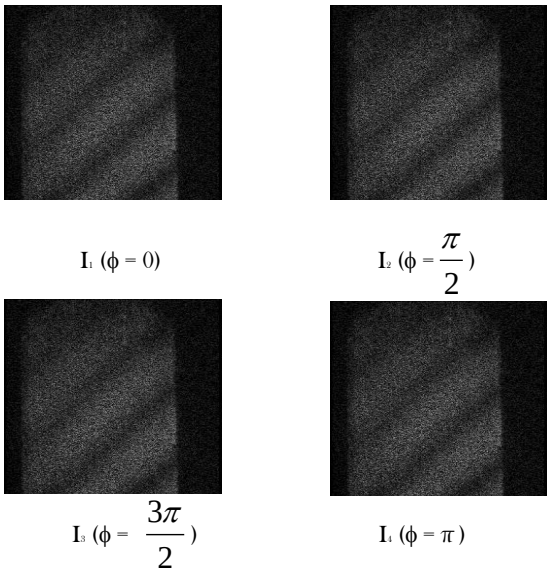


Figure 4. Interferograms obtained by the technique of shift of phase after 12 min of immersion.


Figure 5. a- Distribution of wrapping phase. b- Distribution of unwrapping phase

### 5.3. Representation of the wrapping and unwrapping phase

To represent the distributions of the wraping and unwrapping phase (see figure 5 a and b), we chose the algorithm with four images (with a constant increment $\pi/2$) (D.W.Robinson, 1993)

### 5.4. Exploitation of the phase in three dimensions

The exploitation of the phase unwrapping in three dimensions enables us to know the value and the direction of the evolution thickness of film formed on the base metal. Once the phase is determined, the product « e.n = $a$ » can be calculated starting from the distribution of the unwrapping phase. The following equation enables us to calculate « e.n » out of the plan,
which is expressed by (J-I Kato, I. Yamaguchi, and Q. Ping, 1993):

$$\Delta\varphi = (2\pi/\lambda)\Delta L = (2\pi/\lambda).2\Delta(n.e).\cos\varepsilon''$$

with ε" the angle of incidence under which the object is illumineted, « e » is the thickness of film and « n » is the index of refraction of alumina.
From the results recorded for various immersion times, we can represent the variation of the thickness of the passive film with time of immersion of the metal.
one notices that the more the duration of the samples in the chlorinated medium increases, the more the thickness increases.
One as sees on this figure as :
- Firstly this thickness does not evolve/move in the same way on all surface, that can be due :
- A nonuniformity of surface (difference of roughness and the slope of the sample);
- Or with the difference in concentration of the dissolved oxygen on both sides of the surface of the sample;
- Or many two at the same time.
- Secondly the values found thicknesses more important are compared with the values quoted in the bibliography and which are of the order of (nm). This difference is probably due to the hydration of the sample.
The values obtained in experiments can agree with the thicknesses of the layer of Alumina formed in various mediums. In fact this thickness depends on the nature of material, of the conditions of its preparation, the nature of the electrolyte (medium) and the duration.

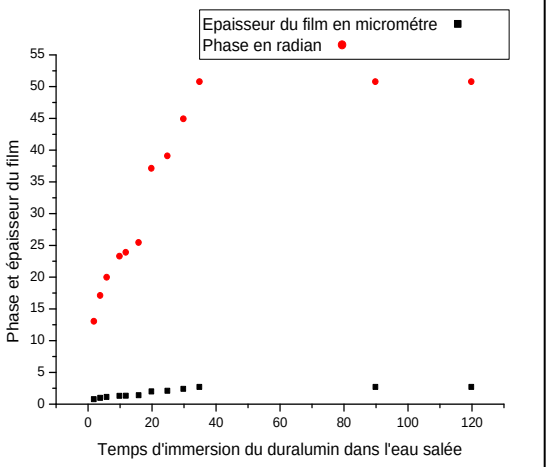


Figure 5. Varying the phase and the film thickness as a function of immersion time of the metal.

## 6. Conclusion

The technique speckle is a technique no destructive rapid and precise. It makes it possible to take qualitative and quantitative measurements static or dynamic deformations at weak frequencies, provided that the deformation does not exceed the diameter of the grain of speckle. It is also shown that a mathematical operation such as the difference in two images in two different states, makes it possible to generate fringes of correlation. In this work one showed that the chemical reactions under consideration for the formation and the destruction of passive film, agree well with our practical results. With the technique of interferometry speckle and by combining to him the technique of shift of phase (phase shifting), one also could evaluate the variation thickness of passive film formed according to the time of immersion of our samples in a salt solution.

## References

[1] K.CREATH,1985,phase shifting speckle interferometry, *Applied Optics*, 24, pp.3053-3058.

[2] J.CDainty, 1975, Laser speckle and related phenomena, Springer-Verlag Berlin Heidelberg New York.

[3] R. Jones and C.Wykes, 1989, Holographic and speckle interferometry, Cambridge University Press.

[4] J-I Kato, I. Yamaguchi, and Q. Ping, 1993, Automatic deformation analysis by a TV speckle interferometer using a laser diode, *Appl*, 32, pp.77-83.

[5] G.Okamoto, T.Shibata, 1978, In passinty of metals, Frankelthal and Kruger editors Electrochemical Society Princetron. *NJ*, pp. 646-677.

[6] D.W.Robinson, 1993, Phase unwrapping methods inteferogram analysis, eds. Institute of Physics Bristol UK, pp.194-229.

[7] R.S.Sirohi and F.S.Chau , 1999, Optical methods of measurement, Wholefield techniques,Marcel Dekker, New York-Basel, pp .152-182.

[8] C.Vargel,1999, Corrosionl'Aluminium, Dunod,pp.65-84.

Journal of New Technology and Materials
JNTM
Vol. 03, N°01 (2013) 23-27

OEB Univ. Publish. Co.

# Downstream physico-chemical and bacteriological investigation of wastewater of Oued Athmania treatment plant

*Abdelhakim Belaidi*, Mounira Adoui, Amar Zellagui, Noureddine Gherraf* and Abdellah Ouldjaoui*

**Laboratory of Biomolecules and Plant Breeding, Life Science and Nature Department ,Faculty of Exact Science and Life Science and Nature, University of Larbi Ben M'hidi Oum El Bouaghi, Algeria.*

*Received: June 19, 2012; revised June 10, 2013, accepted June 30, 2013,*

***Abstract***

*Wastewater treatment is a very important process that consists of applying modern and new technology to improve or upgrade the quality of a wastewater because its disposal whether by surface, subsurface methods or dilution, is dependent on its treatment. In the present work a full study has been carried out dealing with the physicochemical and bacteriological properties of wastewaters after being treated in* ***Oued Athmania*** *Wastewater Treatment Plant. The results revealed that the findings are in conformity with the international standards.*

***Key words****: wastewater, physicochemical, bacteriological, properties.*

## 1. Introduction

Usually wastewater treatment will involve collecting the wastewater in a central, segregated location (the Wastewater Treatment Plant) and subjecting the wastewater to various treatment processes.

Water is the most important and indispensable natural resource for life. Therefore, the conservation of clean and suitable water resources for different uses is a national responsibility so as to assure protection and safety for the environment. Nevertheless, the ever-increasing demographic growth has led to intensive urban farm and various activities across all Algerian cities during the last decade. These activities have induced a drastic raise of domestic untreated wastewaters which may cause a spread of serious diseases. For this purpose, wastewaters require treatment before being rejected in nature to rid it from polluting organic matter and microorganisms, including bacteria, (Salmonella-sp, E.coli, Vibrio cholera) or a virus (polio, hepatitis A and B).

Whatever the type of treatment used in wastewaters technology, it usually goes through three successive steps:

1 - An initial physical treatment aiming to eliminate 20 to 30% of the non-dissolved solids through screening or sedimentation.

2 - A secondary purification (biological treatment) to get rid of dissolved organic matter. This treatment depends on the ability of micro-organisms to dissolve the contaminated organic matter. The active sludge method is the most widely used and the most effective.

3 – A biological and / or physical treatment to get rid of nitrogen or inorganic phosphorus or other chemical materials.

After being purified physically and biologically, wastewaters are usually cleaned using chlorine to eliminate the pathogenic micro-organisms.

Several measurements have to be conducted before making any appropriate decision for treatment, including: $BOD_5$ (biological oxygen demand), COD (chemically oxygen demand), SM (suspended material)

## 2. Materials and methods

During our study, we have performed the following physicochemical and bacteriological characteristics of the wastewaters of **Oued Athmania** station (Mila) before and after treating the water using the active sludge method.

### 2.1. Physicochemical analysis [1,2]

1. Temperature: using a thermometer.
2. pH: using a pH-meter.
3. COD: to measure the COD of treated water, we used tubes with $K_2C_2O_7$ or $KMnO_4$. However for non-treated water we used tubes with $Hg_2SO_4$. After heating the tubes at 150°C for two hours and then cooled, COD values are read using a spectrophotometer.
4. $BOD_5$: each sample of treated and untreated water was put in a glass bottle and well stirred before being put in a BOD-meter and left for an hour. Then NaOH tablets were added to absorb $CO_2$ and $BOD_5$ rates were recorded after 5 days of incubation.
5. Suspended materials (SM): these materials are measured using a Spectrophotometer.

### 2.2. Bacteriological Analysis [3,6]

These analyzes were conducted by looking for fecal pollution indicators and some pathogenic bacteria (Salmonella).

Since the wastewater is rich in micro-organisms, it is subjected to many special treatments before bacteriological analysis.

1. Find the Coliform bacteria and the fecal Coliform bacteria according to the two steps:

- **Presence Test**

We have used a BCPL medium (with **Durham**) by using different concentrations of three consecutive dilutions of the water so we can read the more likely number by referring to the **Mac Grady** table. Samples are incubated at 30-35 °C for 24-48 h.the color Change of the medium with production of gas highlights the possible presence of the coliform bacteria.

- **Confirmatory test**

Tubes were seeded in Shubert medium containing Durham from positive BCPL tubes. Sample is incubated at 40-44 °C. Kovacs detector is added to tubes containing turbidity and gas production. Formation of a red ring indicates the presence of fecal Coliform bacteria, especially E-coli.

2. Detection of fecal Streptococcus bacteria

Detection of these bacteria is based on two stages:

- **Presence test**

Tubes were seeded with Rothe at different concentrations for three consecutive dilutions. The sample is incubated at 37 °C. Samples that exhibit certain turbidity indicate the presence of fecal Streptococcus bacteria.

- **Confirmatory test**

Tubes were seeded with Litsky medium from Rothe tubes and incubate for 24-48 h at 37 ° C, a violet ring reveals the presence of fecal streptococcus bacteria.

3. Presence Of Salmonella Bacteria

These pathogenic bacteria are detected in two steps:
Samples are seeded in the liquid environment SFB: and then incubated at 37 °C.
Samples are seeded in Hectoen environment: from SFB positive tubes is seeded Hectoen medium then are incubated at 37 °C for 24-48 h.The appearance of green or blue spots with black or non-black centers indicate the presence of *Salmonella* bacteria but this must be confirmed using biochemical analyses.

## 3. Results and discussions

Table 1: physicochemical results before and after treatment

| Sample | 1 | | 2 | | 3 | | 4 | | 5 | | 6 | |
|---|---|---|---|---|---|---|---|---|---|---|---|---|
| | Before | after | Before | after | before | after | before | after | before | after | before | After |
| **characteristics** | | | | | | | | | | | | |
| **T°** | 16.5 | 17 | 17.3 | 17 | 18 | 19 | 17.5 | 18 | 19 | 18 | 17.5 | 17 |
| **pH** | 7 | 7.5 | 7 | 7 | 6.8 | 7 | 7.5 | 6.6 | 7.9 | 7 | 6.9 | 7 |
| **SM: mg/L** | 457 | 17 | 286 | 12 | 306 | 22 | 278 | 10 | 291 | 17 | 325 | 10 |
| **COD: mg/L** | 522 | 54 | 426 | 45 | 700 | 36 | 444 | 62 | 413 | 66 | 361 | 46 |
| **BOD: mg/L** | 270 | 35 | 230 | 16 | 250 | 37 | 210 | 11 | 230 | 26 | 200 | 14 |

### 3.1 Physico-chemical results before and after treatment

- Temperature: recorded Temperatures ranged between 16-19 °C for treated and untreated water and hence the values did not exceed standards (25 °C).
- pH: The values show that the treated water and untreated water was neutral, as the recorded values ranged between 6-7.
- COD: For untreated wastewater we recorded considerable values for chemically absorbed oxygen ranging between 361-700 mg / l. this indicates the presence of significant pollution with organic or inorganic compounds. In the other hand, we recorded a significant lack of chemically absorbed oxygen COD for the wastewater after the treatment station with a range of 36-66 mg/L and the results are consistent with the standards which stated that the COD of the treated water should be between 120-90 mg/l.
- BOD5 of untreated domestic wastewater showed large values ranging between 270-200 mg/l, which confirms the richness of this water with bio-oxidable contaminated organic matter.
- After treatment we noticed a large decrease in the BOD5 as we recorded values ranged between 11-37 mg/L which is in conformity with the standards for treated wastewaters (40-20 mg/l)..

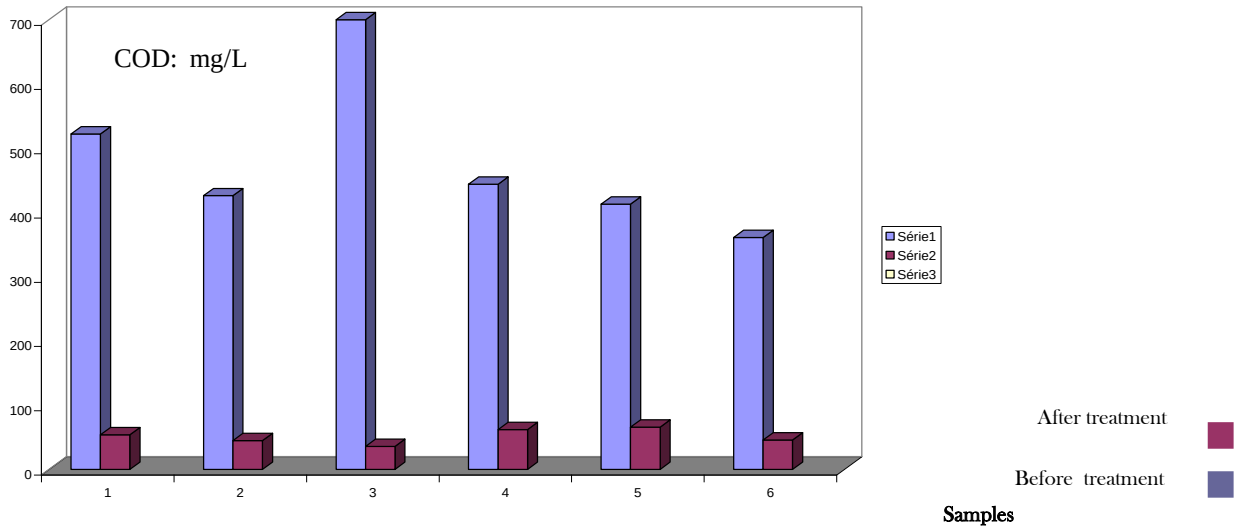


Figure 1. DCO values before and after treatment

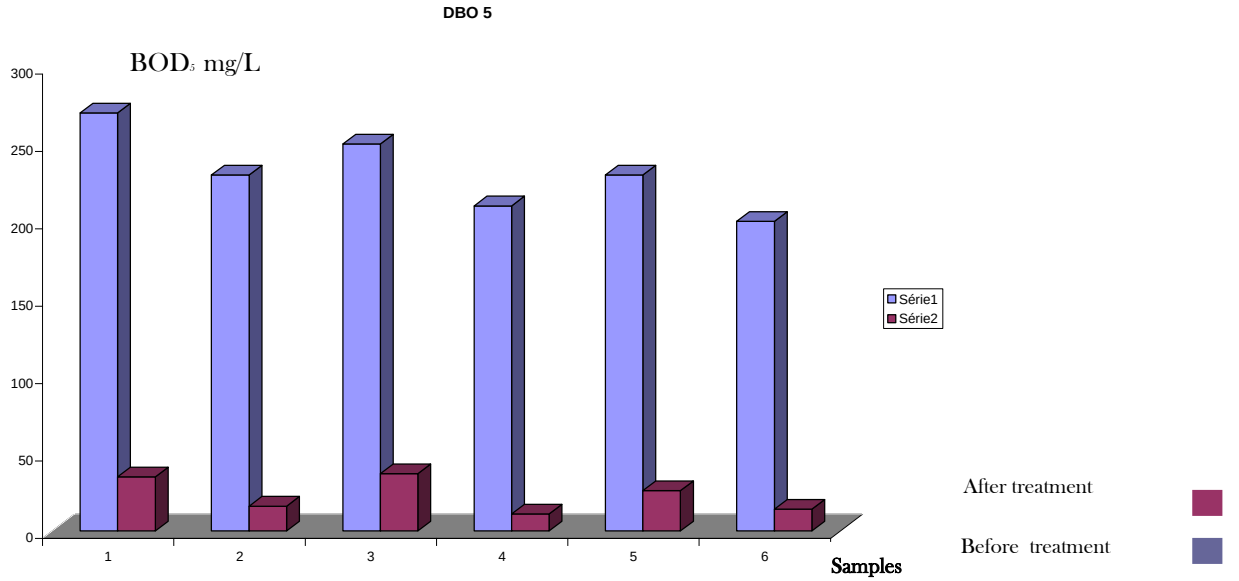


Figure 2. $BOD_5$ values before and after treatment

➢ SM: the amount of suspended material recorded after treatment is significantly lower than that recorded after treatment as a large part is eliminated during the first and second deposition processes.

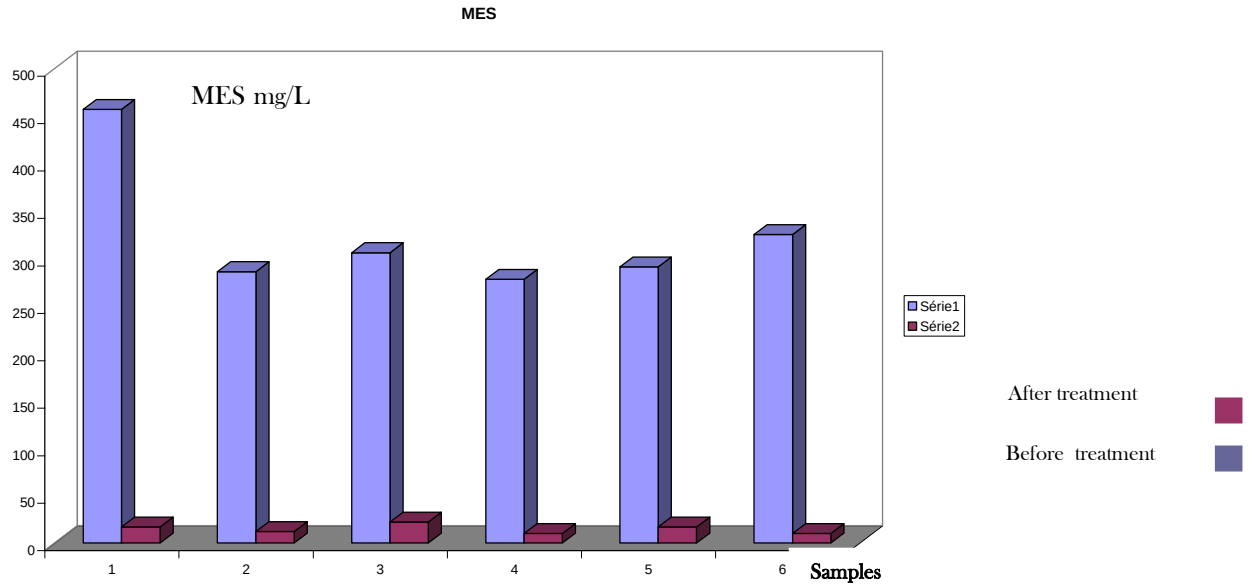


Figure 3. SM Values before and after treatment

### 3.2. Bacteriological results

**1. Coliform bacteria:** The results showed a color change of the medium with the production of gas, indicating the possible presence of these bacteria in the treated and untreated waters.
Seeding with Shubert gave microbial turbidity and after the addition of Kovacs reagent gave a red ring, which indicates the presence of bacteria fecal Coliform bacteria, especially E. coli that has been identified using the biochemical analysis. We recorded very high numbers of these bacteria in untreated wastewaters, however in the treated water we recorded a significant shortfall due to the fact that these bacteria belongs to the active sludge which oxidizes and dissolves organic matter.

**2. Fecal *Streptococcus* bacteria:** we recorded the presence of fecal Streptococcus bacteria in wastewater before and after treatment, but always with the largest number in untreated water. These bacteria are also active in the formation of sludge, which has led to their decrease after treatment.

**3. *Salmonella* bacteria:** Our results showed the absence of Salmonella bacteria, either in treated or untreated wastewater.

Table 2: Effectiveness of the treatment:

| | Decrease rate | | | | | |
|---|---|---|---|---|---|---|
| **Sample** | 1 | 2 | 3 | 4 | 5 | 6 |
| **MES** | 95 | 95 | 92 | 96 | 94 | 96 |
| **COD** | 89 | 89 | 95 | 86 | 84 | 87 |
| **BOD5** | 87 | 93 | 85 | 72 | 89 | 93 |
| **Coliform** | 45 | 93 | 75 | 50 | 76 | 89 |
| **Streptococcus** | 48 | 60 | 45 | 97 | 72 | 41 |

The results in table 2 confirm the effectiveness of the treatment carried out in **Oued Athmania** station.
The Results show a significant lack of the organic matter through $BOD_5$ values as we recorded a decrease rate ranged between 87 and 93%.
According to H. Leclerc **[6]** the purification of wastewater in appropriate circumstances using the sludge method often exceeds 90%.

We recorded also a significant decrease of suspended material (by approximately 95-96%) and lack of organic matter and mineral chemically oxidable with a rate ranged between 84-95%.
We have also a very significant decrease ranged between 54-93% of Coliform bacteria and 60-97% of *Streptococcus* bacteria.

## 4. Conclusion

Through the above results we can emphasize that rejection of the water after treatment to the environment will not affect the ecosystem or impair the health of the citizens, but we recommend cleaning the water using chlorine after treatment in order to ensure the absence of any harmful bacteria that may lead severe damage to the health.

We also emphasize the effective treatment of active sludge remained after treatment because it contains a huge number of micro-organisms, which can be pathogenic because the only method used in Algeria is to expose it to sun rays. So we incite the concerned authorities to provide the purification station with modern technology in order to make use of sludge and to use it as a source of fertilizer.

## References

[1] I. Howard, E. Espigares, P. Lardelli, J.L. Martín, M. Espigares, Evaluation of microbiological and physicochemical indicators for wastewater treatment, *Environ Toxicol.* 19(3): (2004) 241-9.

[2] O.B. Shittu, J.O. Olaitan, and T. S. Amusa, Physico-Chemical and Bacteriological Analyses of Water Used for Drinking and Swimming Purposes in Abeokuta, *Nigeria, African Journal of Biomedical Research*, 11 ( 2008) 285 - 290

[3] J.P. Guiraud Microbiologie alimentaire Ed Dunod Paris. (1998), 18-19.

[4] Prescott et al. Microbiologie, 2ème édition française. 2003

[5] J, Pelmout. Bactéries et environnement. PUG, Paris. 1994

[6] H. Leclerc et al. Microbiologie du tube digestif l'eau et les aliments. DOIN, Paris. 1986

Journal of New Technology and Materials
JNTM
Vol. 03, N°01 (2013) 28-32

OEB Univ. Publish. Co.

# A new drain current I–V model for MESFET with submicron gate

*M. Azizi[a] and C. Azizi[b]*
[a]*Department of Material Sciences. Larbi Ben Mhidi University, Oum El Bouaghi. Algeria.*
*Email: mounir.perso@gmail.com*
[b]*Department of Material Sciences. Larbi Ben Mhidi University, Oum El Bouaghi. Algeria. email: aziziche@yahoo.fr*

*Received: August 28, 2012, revised: May 19, 2013, accepted: May 28, 2013*

***Abstract***

*In this work we present a new nonlinear approach for the calculation of the static characteristics of MESFET GaAs with submicron gate. First, we compare the results of the numerical simulations of the three main models for the MESFETs with submicron gate : Ahmed [1], Islam [2] and Memon [3] with experimental results. Then we propose a new approach that takes into account the surface states of the Schottky junction through a new mobility law for the determination of the output characteristics. The thermal effect is also represented in the mobility law. The comparison of our model with the three previous models referring to the experimental data shows that our approach gives the most accuracy result. Also, the proposed model can be used in the case of logic or analog circuits based on submicron GaAs MESFET.*

***Keywords:*** *MESFET; GaAs; nonlinear models; interface states; submicron gate.*

## 1. Introduction

The widespread use of field-effect transistor with gallium arsenide "GaAs MESFET" in telecommunications and technology using the microwave field effect operating in the gigahertz band warrants a critical need for the analytical study of the physical behavior of this component. The development of a simple mathematical model describing the output characteristics of the MESFET is the main objective of this work.

Indeed, several models have been proposed since the fifties. Most proposals simulate a perfect Schottky junction barrier with no surface effects, therefore distorting their results.

The MESFET with a submicron gate has a better treatment of high-frequency signals. But this creates a large conductance, a decrease of the transconductance and a change in the threshold voltage $V_T$. This is called the short channel effect, and it makes the development of a theoretical model very complex. In the case of a submicron channel, the interface state due to the Schottky barrier cannot be eliminated.

In this work, we relied on the model of Memon [1] and that of Islam [2] in order to verify the accuracy of the results by comparing them with experimental data. An extension of the models was proposed by the introduction of the electron mobility in terms of current intensity, conductance and transconductance. A study of the thermal effect on the electronic behavior of GaAs MESFET using the proposed model was performed. The treatment was carried out through software simulation, programmed using MATLAB 7, 2010.

## 2. Nonlinear models of the MESFET

Memon's model [3] which describes the electrical behavior of the MESFET was proposed in 2006. This model is an extension of the Ahmed model [1] that also mades changes to other theories.

The relationship between the drain-source current $I_{ds}$ and the drain-source voltage $V_{ds}$ is given in the model of Ahmed [1] by:

$$I_{ds} = I_{dss}\left[1-\frac{V_{gs}}{V_T+\Delta V_T+\gamma V_{ds}}\right]\times\tanh\left(\alpha V_{ds}\right)\left(1+\lambda V_{ds}\right) \qquad (01)$$

$V_{gs}$: gate-source voltage.
$I_{dss}$: saturation current.
$V_T$: threshold voltage.
$\Delta V_T$: shift in the threshold voltage.
$\alpha$: saturation current parameter, used to simulate the linear region on $V_{ds}$.
$\lambda$: simulation parameter of the dependence of the $I_{ds}$ to $V_{ds}$ in the saturation region.
$\gamma$: parameter simulation of the threshold voltage on $V_{ds}$.

Where:

$$V_T = \frac{qN_d a^2}{2\varepsilon_s} - \Phi_b \quad \text{and} \quad \Delta V_T = \frac{4a}{3L_g}V_T \qquad (02)$$

q: electron charge.
$N_d$: carrier density in the channel.
a: channel thickness.
$\Phi_b$: Schottky barrier height.
$\varepsilon_s$: semiconductor permittivity.
$L_g$: intrinsic channel length (controlled by the gate).

$$I_{dss} = \left(\frac{\beta}{1+\mu\left(V_{gs}-V_T-V_{ds}-\Delta V_T\right)}\right) \qquad (03)$$

$\beta$: transconductance parameter.
$\mu$: simulation of the effect of electron mobility parameter.

Ahmed [1] based his model on those of Rodriguiz [4] and Materka [5]. He introduced $\Delta V_T$ which is a variation of $V_T$ caused by the submicron geometry of the gate.

Islam [2] proposed another model in 2004. He added $\mu V_{gs}$ in the term $(1 + \lambda V_{ds})$ The expression that he proposed for the current intensity is as follows:

$$I_{ds} = I_{dss}\left[1-\frac{V_{gs}}{V_T+\Delta V_T+\gamma V_{ds}}\right]^2 \times \tanh\left(\alpha V_{ds}\right)\left(1+\lambda V_{ds}+\mu V_{gs}\right) \quad (04)$$

Memon's model [3] is an extension of Ahmed's model [1]. He notes the principle of the presence of an interface effect in the metal-semiconductor junction, which makes the Schottky barrier not perfect. This effect is the main cause of the decrease in $V_{gs}$ received in the semiconductor channel compared to the applied $V_{gs}$. Ignoring this effect causes a remarkable difference between the experimental characteristics of the MESFET and those simulated.

The $I_{ds}$ expression in the Memon's model is given by:

$$I_{ds} = I_{dss}\left[1-\frac{V_{eff}}{V_T+\Delta V_T+\gamma V_{ds}}\right]^2 \times \tanh\left(\alpha V_{ds}\right)\left(1+\lambda V_{ds}\right) \quad (05)$$

where:

$$V_{eff} = \frac{V_{gs}}{1+\eta e^{V_{gs}}} \quad (06)$$

The main difference between the Memon's model [3] and those of Ahmed [1] and Islam [2] is in the term $\eta$ describing the effect of the Schottky barrier interface. Memon [3] did not revise the term $(1 + \lambda V_{ds})$ in the expression of $I_{ds}$. While the model of Islam [2] introduced a modification in this term that makes his model a better approximation.

## 3. New approach

In our study, we propose the introduction of the term $\mu V_{gs}$ in the expression of $I_{ds}$ to take into account both the interface states at the metal-semiconductor junction effect and the electron mobility parameter effect. It gives:

$$I_{ds} = I_{dss}\left[1-\frac{V_{eff}}{V_T+\Delta V_T+\gamma V_{ds}}\right]^2 \times \tanh\left(\alpha V_{ds}\right)\left(1+\lambda V_{ds}+\mu V_{gs}\right) \quad (07)$$

Our model is a combination of Memon's model [3] and that of Islam [2].

The choice of a law for carrier mobility in GaAs is important for a correct description of the physical phenomena in submicron-gate MESFET. In the case of weak fields, free carriers are in thermal equilibrium with the grid and their average speed is proportional to the electric field:

$$v(E) = \mu_n E \quad (08)$$

However, there is no law that truly reflects the variation of mobility with the electric field and several approximate analytical expressions have been proposed for this function. For our part we propose the following law:

$$v(E) = \mu(E)E = \frac{\mu_n E}{1+\left(\frac{E}{E_c}\right)} \quad (09)$$

The expression of mobility is given by [7]:

$$\mu(E) = \frac{\mu_n}{1+\left(\frac{E}{E_c}\right)} \quad (10)$$

with

$$E_c = v_s / \mu_n \quad (11)$$

Where $\mu_n$ is the electron mobility at low electric fields, and $v_s$ is their saturation velocity.

The dependence of the mobility on the electric field at room temperature allowed us to see the influence of the thermal effect on the output characteristics $I_{ds}$ - $V_{ds}$. Indeed, an increase of junction temperature causes a decrease of electron mobility and consequently a decrease of the drain current $I_{ds}$.

Equation (12) gives the variation of the classical electron mobility as a function of temperature for gallium arsenide [8].

$$\mu = \mu_0(300^0 K)[300/T]^{2/3} \quad (12)$$

The saturation velocity is given by [9]:

$$v_s = \frac{2.410^5}{1+\exp(T/600)} m/s \quad (13)$$

The dependence of the threshold voltage can be approximately given by [9]:

$$V_T = V_T(300°K) - \alpha_{vT} T \quad (14)$$

The value of $\alpha_{vT}$ is about the order of 1.2 $mV/°C$.

## 4. Models simulation and comparison with experimental data

A comparative study of the different models mentioned above was performed. The accuracy of these models for GaAs MESFET has been verified by a simulation of the expressions $I_{ds}$ - $V_{ds}$ and then comparing them with experimental data.

We used Matlab 7.10.2010. Once the best approach is reached, the calculations will be interrupted and the best result will count. The fit of the model will be done by choosing the best fitting parameter values.

The physical and geometrical parameters of the component studied here (ref. A4-74-3) are as follows:

$N_d$ = 5 x $10^{17}$ cm-3;
a = 90 nm;
$L_g$ = 0.28µm;
W = 100 µm;
$\Phi_b$= 0.60 V;
$V_T$ = -3.49V;
$\Delta V_T$ = -1.32 V.

The experimental results for this component were obtained from [6].

Figures (1) to (3) shows the output characteristics $I_{ds}$ - $V_{ds}$, both experimental and simulated for different values of $V_{gs}$, for a submicron-gate GaAs MESFET component using the models of Ahmed [1], Islam [2] and Memon [3].

In the case of Ahmed [1] the results are quite satisfactory in the linear region for $V_{gs}$ = *-2.2V* and *-3.3V* with a slight difference in the saturation region. For $V_{gs}$ = *-1.1V* the results are much better in the saturation region. The results are worse for $V_{gs}$ = *0.0V.*

For the case of Islam [2] presented in figure (2), we notice a marked improvement over the previous case for both values of $V_{gs}$ = *-1.1* and *0.0 V.* This is due to the incorporation of the term electron mobility parameter effect *($\mu V_{gs}$).*

Figure (3) illustrates the comparison of the results obtained by the Memon model [3] with the experimental data. The gap is smaller because Memon considered the effect of the interface state of the metal-semiconductor junction in his model, unlike the two previous models where the effect was considered negligible.

In Figure (4) we present our simulation results of output characteristics based on the new proposed approach, for GaAs MESFET components with a *0.28 x 100 µm²* gate dimensions. We can clearly see that it gives results that are better than those demonstrated previously, even with a slight discrepancy in the linear region for $V_{gs}$ = *-1.1 V.*

In Figure (5) we can clearly see the comparison between the Memon's model [3] and the one proposed here in reference to the experimental results.

The accuracy of the models can be better estimated by calculating the error of each simulation using the least squares method, which gives a numerical result of the shift in then measured curves relative to those observed. Table (1) illustrates the different values of the errors of the models for different values of $V_{gs}$. We clearly see that the average error of the new approach is smaller and it is equal to 0.5984, while in the Memon's model [3] is 0.7915. Those of Ahmed [1] and Islam [2] exceed the unity. According to these results, we deduce that the new model is more accurate than those cited above, especially for $V_{gs}$ = *0.0V* and *-1.1V.*

The thermal effect has been studied through the law of mobility using equation (12) in the case of Memon [3] and in the new method. Figures (6) and (7), representing the simulation of the characteristics $I_{ds}$ *($V_{ds}$)* for $V_{gs}$ = *0.0V,* clearly shows the variations of drain-source current depending on drain-source voltage for various values of temperature. Indeed, the current increases when the temperature T decreases in the model we have proposed.

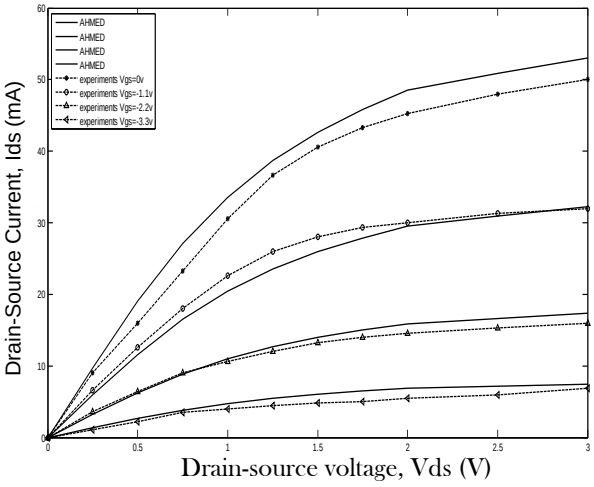


Figure 1. Comparison of the characteristics $I_{ds}$ ($V_{ds}$) simulated and observed using the model of Ahmed [1] for a GaAs MESFET (0.28 x 100 µm²)

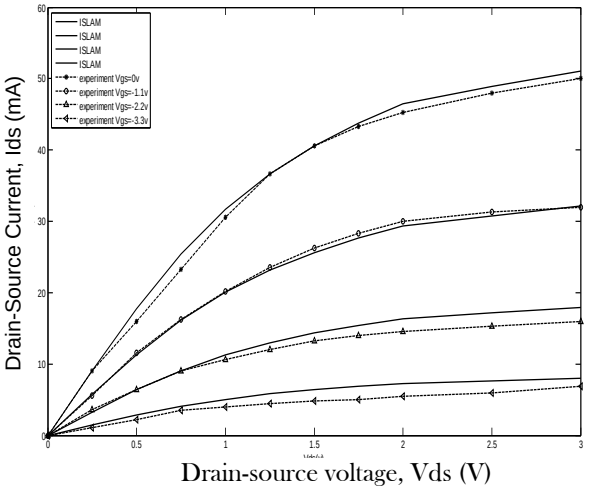


Figure 2. Comparison of the characteristics $I_{ds}$ ($V_{ds}$) simulated and observed using the model of Islam [2] for a GaAs MESFET (0.28 x 100 µm2).

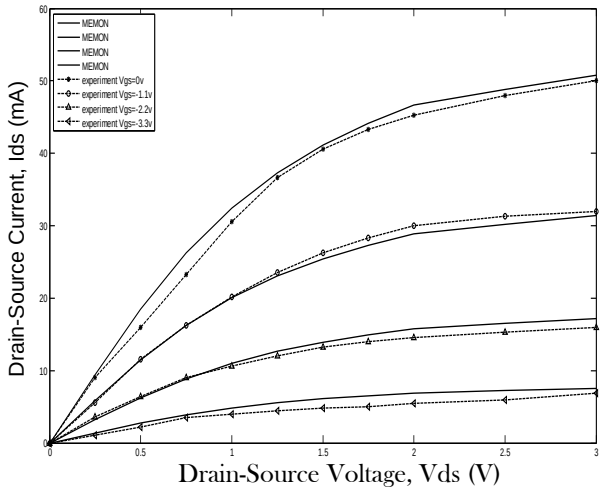


Figure 3. Comparison of the characteristics $I_{ds}$ ($V_{ds}$) simulated and observed using the model of Memon [3] for a GaAs MESFET (0.28 x 100 µm2).

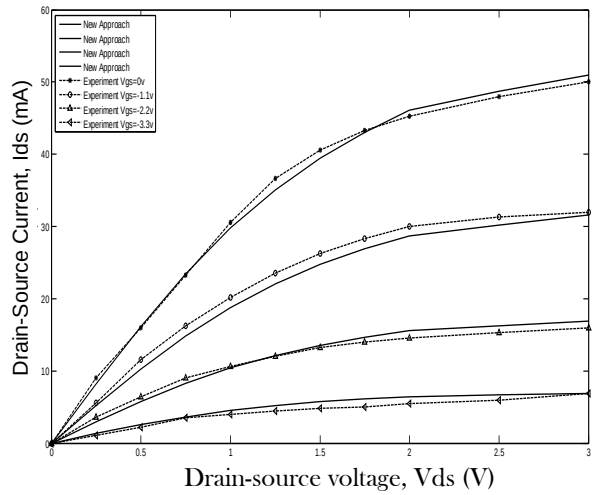


Figure 4. Comparison of the characteristics $I_{ds}$ ($V_{ds}$) simulated and observed using the new approach [1] for a GaAs MESFET (0.28 x 100 µm2).

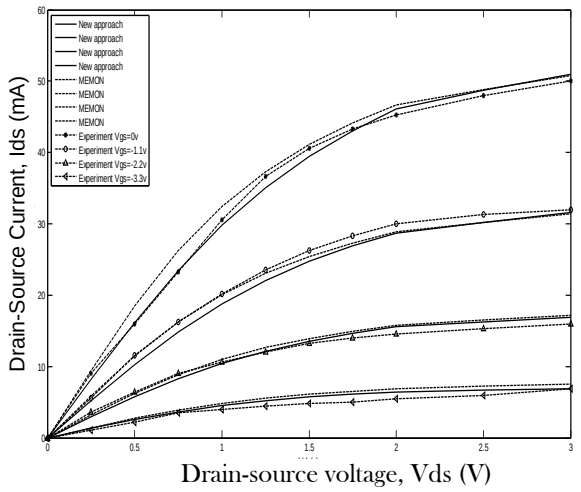


Figure 5. Comparison of the characteristics $I_{ds}$ ($V_{ds}$) of the model Memon [3] and the new approach for a GaAs MESFET (0.28 x 100 µm2).

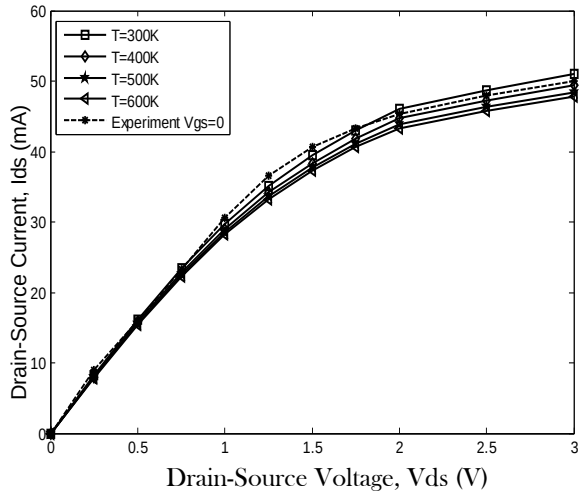


Figure 6. Variation of $I_{ds}$ ($V_{ds}$) with temperature for a GaAs MESFET (0.28 x 100 µm2) using the new approach.

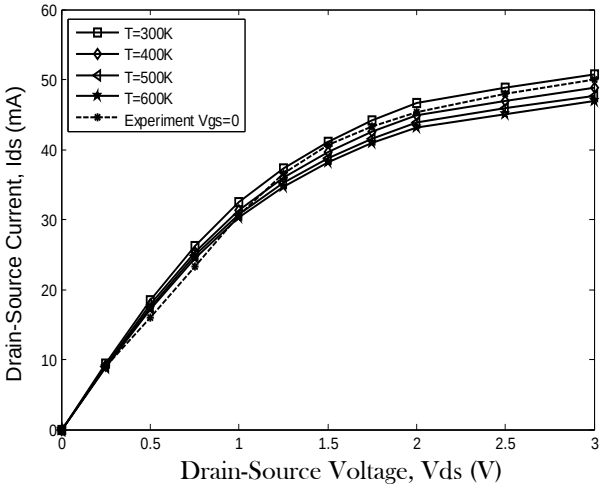


Figure 7. Variation of $I_{ds}$ ($V_{ds}$) with temperature for a GaAs MESFET (0.28 x 100 µm2) using the Memon's model.

Table 1. Comparison of RMS errors of different MESFET models as a function of V*gs*.

| VGS / THE MODEL | Vgs = -3.3 V | Vgs = -2.2 V | Vgs = -1.1 V | Vgs = 0.0 V | Average Error |
|---|---|---|---|---|---|
| AHMED | 3.037 | 0.244 | 1.358 | 0.584 | 1.306 |
| ISLAM | 1.103 | 0.146 | 1.886 | 1.062 | 1.049 |
| MEMON | 0.775 | 0.580 | 1.189 | 0.621 | 0.791 |
| New Approach | 1.009 | 0.442 | 0.895 | 0.046 | 0.598 |

## 5. Conclusion

First we performed simulations using three mathematical models to study the static properties of submicron gate GaAs MESFET. The results of these simulations were then compared with experimental data. Among the models of Ahmed [1], Islam [2] and Memon, we established that Memon's [3] is closest to experiment. This was verified by the calculation of RMS errors.

A new model was performed by the taking into account both the interface effect in the metal-semiconductor junction and the electron mobility effect. The simulation based on the new approach confirmed that it contain the smallest error.

It confirms that it is the most accurate method of simulation of the static characteristic of GaAs MESFET with submicron gate.

Finally we have seen the thermal effect on the output static characteristic of the MESFET GaAs.

## Acknowledgment

The authors gratefully acknowledge the contributions of the department of material sciences of the University of Oum El Bouaghi.

## References

[1] Mansoor M. Ahmed, Haroon Ahmed, and Peter H. Ladbrooke," An Improved DC Model for Circuit Analysis Programs for Submicron GaAs MESFET's", *IEEE Transactions On Electron Devices*, Vol. 44, No. 3, (March 1997).

[2] Islam M. S and Zaman M. M, "A seven parameter nonlinear I-V characteristics model for sub-µm range GaAs MESFETs," *Journal of Solid-State Electronics*, Vol. 48 pp. 1111-1117, (2004).

[3] N. M. Memon, M. M .Ahmed and F.Rehman "A Comprehensive Four Parameters I-V Model for GaAs MESFET Output Characteristics" *Journal of Solid State Electronics*, Vol. 51, pp511-516 (2007).

[4] Rodriguez T. J, England, "A five-parameter dc GaAs MESFET model for nonlinear circuit design," Proc. IEEE , pt. G, Vol. 139, No. 3, pp. 325-332, (1992).

[5] Tomasz Kacprzak And Andrzej Materka, "Compact dc Model of GaAs FET's for Large-Signal Computer Calculation" *IEEE Journal Of Solid-State Circuits*, Vol. Sc-18, No. 2, (April 1983).

[6] NEC data sheet California eastern laboratories.

[7] Nicolas Dubuc "Modélisation Electrothermique de transistors MESFET SiC et optimisation d'une architecture Doherty pour l'amplification de puissance à haut rendement" Thèse doctorat d'état, Université de Limoges, (2003) N°84.

[8] Issam Hamma "Contribution à l'étude des propriétés statiques du MESFET GaAs" Mémoire de magister, C .U d'Oum El bouaghi, (2007).

[9] T.A. Fjedly. T. Yterdal, M.S.Shur "Introduction to Device Modeling and circuit "New York ،Wiley ،"simulation, (1998).

Journal of New Technology and Materials
JNTM
Vol. 03, N°01 (2013) 33-36

OEB Univ. Publish. Co.

# Synthesis of Perovskite Type of Zinc Titanate nano-Crystal Powders via Combustion Technique

*Solmaz Ghanbarnezhad[a,*], Ali Nemati[a,b], Maryam Abolfazli[a]*

[a]*Department of Materials Engineering, Science & Research Branch, Islamic Azad University, P. O. Box 14515 775, Tehran, Iran*
[b]*Department of Materials Engineering, Sharif University of Technology, P. O. Box 11365 9466, Tehran, Iran*
[*]*e-mail address: S.ghanbarnezhad@yahoo.com*

*Received; September 05, 2012, revised: February 11, 2013, accepted: June 15, 2013*

***Abstract***

*Zinc titanate ($ZnTiO_3$; ZT) powders were successfully prepared by a combustion technique. The ZT powders were heated at temperature from 500 °C to 850 °C for various times 2, 4 and 6 h. Powder samples were characterized using thermogravimetric (TGA), differential thermal analysis (DTA), X-ray diffractrometer (XRD), scanning electron microscopy (SEM) and laser particle size analyzer (LPSA). The second phases such as ZnO and $TiO_2$ were detected in the powders calcined below 800 °C. A single perovskite of the ZT powders was found with calcination temperatures at 800 °C. The shape of crystalline will be changed as increasing the time of calcination temperature. The TGA-DTA results corresponded to the XRD investigation. According to SEM and LPSA analysis nano-crystal powders of ZT were obtained.*

***Keywords:*** *Combustion Technique; Calcination; Zinc titanate; Perovskite; Ultra-fine*

## 1. Introduction

First investigations of a binary oxide system consisting of ZnO and $TiO_2$ introducing a phase diagram were conducted by Dulin and Race 1960, who reported that there are three compounds exist in the ZnO–$TiO_2$ system, including $Zn_2TiO_4$ (cubic), $ZnTiO_3$ (hexagonal) and $Zn_2Ti_3O_8$ (cubic) [1–2]. $ZnTiO_3$ was perovskite type oxide structure and could be an useful candidate for microwave resonator materials [3] gas sensor [4] (for ethanol NO, CO, etc.) catalyst [2] and paint pigment [5]. Yamaguchi et al. [6] clarified that $Zn_2Ti_3O_8$ is a low-temperature form of $ZnTiO_3$. This system still attracts the attention of researchers because of its importance in practical applications [6–9]. $Zn_2TiO_4$ can easily be prepared by conventional solid-state reaction between 2ZnO and 1$TiO_2$. But, the preparation of pure $ZnTiO_3$ from a mixture of 1ZnO and 1$TiO_2$ has not been successful because the compound decomposes into $Zn_2TiO_4$ and rutile at about 945 °C. There are a lot of processing techniques for preparing ZT powders, such as the solid state reaction technique [1], the sol-gel method [6], molten salt synthesis [10], etc.

The conventional solid state reaction method is the most widely used route.

However, the ceramics which are synthesized by a solid state reaction require high temperature and the resulting powders exhibit many undesirable character -istics: large particle size and wide particle size distribution. Wet chemical synthesises can provide homogenous nano-sized oxides of high purity at lower reaction temperatures but they have a high cost for starting materials, and are intricate and complicated.

The combustion method has much interest; at present it helps to decrease the temperature in the preparation and has a small particle size. The combustion reaction method also has interesting characteristics such as its simplicity, its relatively low cost and the fact that it usually results in products with the desired structure and composition [11]. The applications for zinc titanates were at that time mostly paint pigments and fusion cast thermistors.Although, the first application was as a sorbent for removing sulfur from coal gasification products [8-12]. Nowadays, due to the development of microwave dielectrics, zinc-titanates can be used as dielectric resonators and filters in microwave devices [13]. Thus, in this work, ultra-fine powders of $ZnTiO_3$ successfully were obtained via the combustion method.

## 2. Experimental procedure

The starting materials were commercially available ZnO (>99.5% Merck 108849) and $TiO_2$ (>99.5% Merck 100808). The ZT powders were synthesized by the combustion route as shown in Fig 1. The powders were mixed by ball milling for 12 h with ethanol. After drying and sieving, the powders and urea were mixed and ground in an agate motor. Then, the mixtured powders were calcined using various calcination temperatures, ranging from 500 to 850 °C, for 2 h and at 800 °C for 4, 6.

The reaction of uncalcined ZT powders and urea fuel taking place during heat treatment was investigated by thermogravimetric analysis (TGA), differential thermal analysis (DTA). X-ray diffraction (XRD) was employed to identify the phase formed. The particle morphology and size were directly imaged, using scanning electron microscopy (SEM) and the particle size distribution was determined by using a laser particle size analyzer.

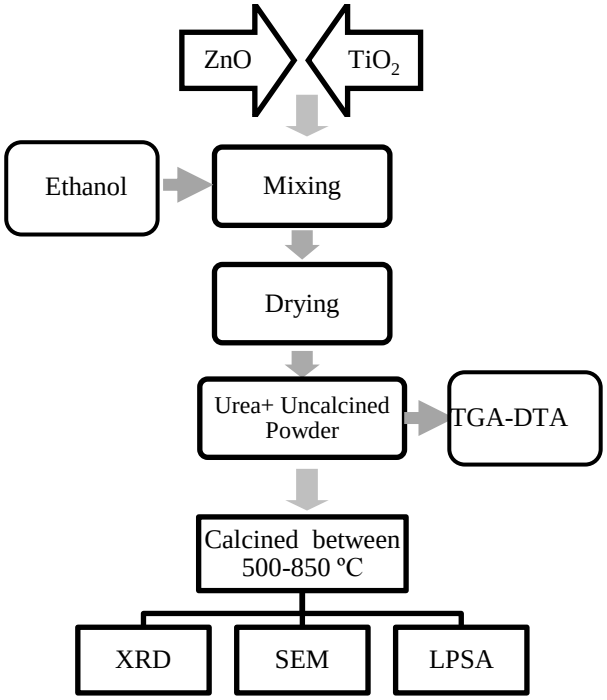


Figure 1. Preparation route for ZT powders

## 3. Results & discussion

Fig 2. shows the TGA and DTA curves of ZT powders prepared via the combustion route. The ZT powders demonstrated a three-stage weight loss; the first one was in the temperature range of 150 to 220 °C, the second one from 300 to 500 °C, and the last one began around 550 °C. The first weight loss is believed to be caused by the melting of the urea. It was related with the endothermic peaks in the DTA curves at 160, 185 and 230 °C. The second step was caused by the evaporation of water and gas. This was associated with the endothermic peak at 330, 410 and 475 °C. The last curve corresponded to a small endothermic peak at 650 °C, and represented the reaction of ZnO and $TiO_2$.

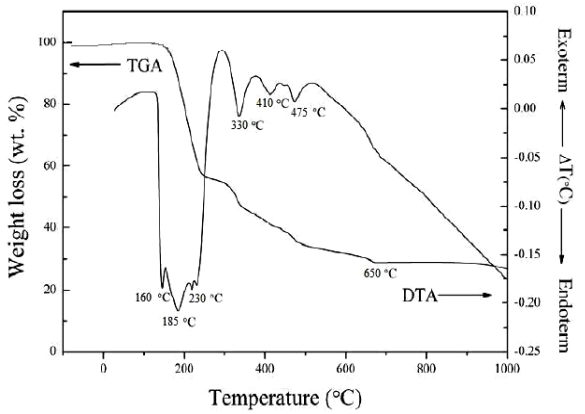


Figure 2. DTA-TG curves of uncalcined ZT powders

Based on the results of DTA and TGA, calcinations were carried out from 500 to 850 °C for 2 h, at a heating /cooling rate of 5 °C /min for the uncalcined ZT powders. The XRD patterns of the ZT powders, formed with different calcination temperatures, are shown in Fig 3.

After calcination from 500 to 700 °C, the precursor of ZnO and $TiO_2$ were detected. When the temperature went above 700 °C, the minor phase of ZnO remained. A high purity of the hexagonal perovskite phase was discovered in powders calcined at 800 °C, which could be matched with JCPDS file number 00-014-0033. Above 800 °C, $Zn_2TiO_4$ phase formed. Results of the X-ray analysis of $ZnTiO_3$ after heat treatment at 800 °C for different times: (a) 4, (b) 6 h and are given in Fig. 4. The average grain sizes were determined from the XRD powder pattern according to the Scherrer's equation [14].

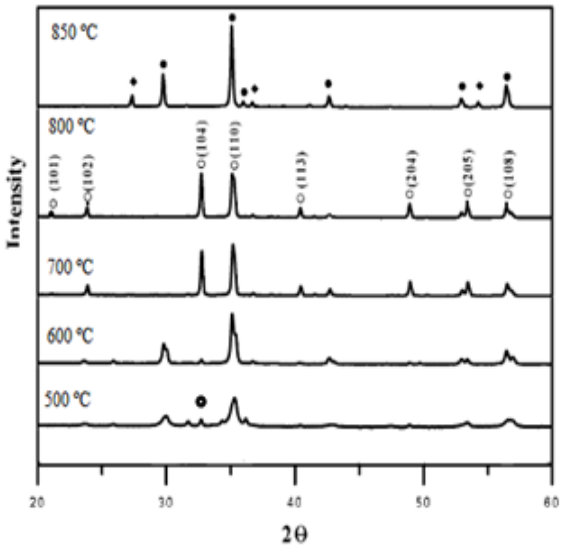


Figure 3. XRD patterns of ZT powders with various calcination temperatures for 2 h; ( ) $ZnTiO_3$, ( ) $Zn_2TiO_4$ and (♦) $TiO_2$, ( ) ZnO

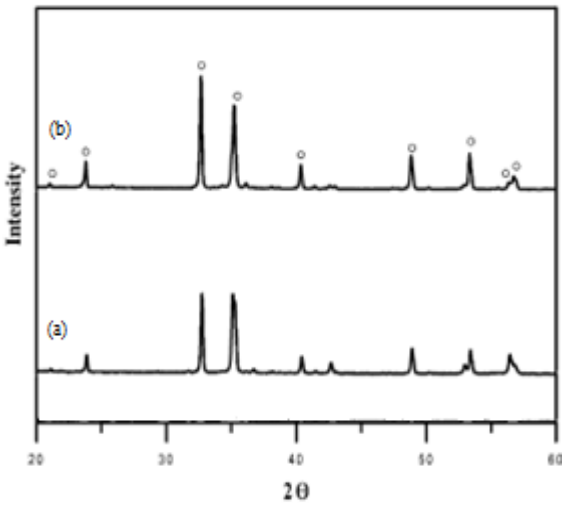


Figure 4. XRD patterns of ZT powders after calcination at 800 °C for different times: (a) 4 and (b) 6 h; ( ) $ZnTiO_3$

$D = k\lambda/(B\cos\theta)$ (1)

Where; D is the size of powder, λ is the X-ray wavelength, B is the FWHM of diffraction peak, θ is the diffraction angle and k is a constant equal to 0.89.

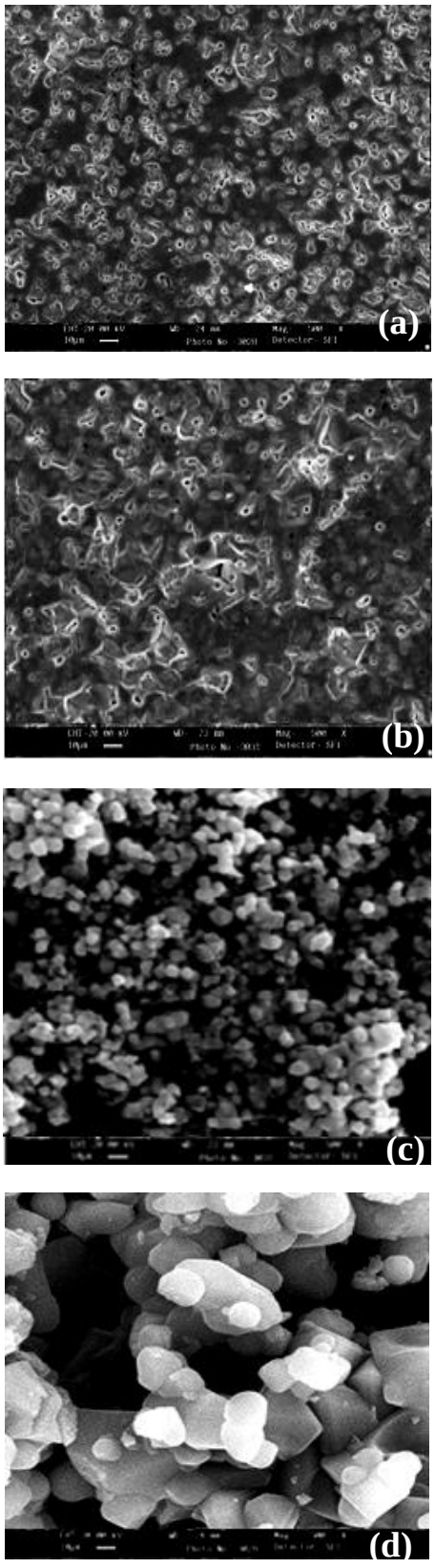


Figure 5. SEM morphology of ZT powders calcined at (a) 600 °C, (b) 700 °C, (c) 800 °C and (d) 850 °C

The average grain sizes of powders fired at 600 °C, 700 °C, 800 °C and 850 °C were about 340, 392, 473 and 541 nm, respectively. These results are in good accordance with SEM observations which are shown in Fig 5.

Heat treatment at 800 °C for different times: 4 and 6 h are given in Fig. 6 shows to enhance the atomic mobility and caused the grain growth to result in a better crystallinity.

The results are in good accordance with XRD analysis.

SEM micrographs revealed when the temperature increased the surface morphology of the samples changes and also appears that a higher calcination temperature favors a particle with larger grain sizes.

The average particle size estimated from SEM is similar with the average particle size computed by XRD data and LPSA which are shown in Fig. 7 and Table 1.

The relative percentage in the perovskite and impurity phases were determined by measuring the major XRD peak intensities of the perovskite and impurity phases.

The percentage of the perovskite phase was estimated by the following equation [15]:

$$\%\ perovskite\ phase = \left(\frac{I_{Perov}}{I_{Per\ ov} + I_{ZnO} + I_{TiO\ 2} + IZn\ 2TiO\ 4}\right) \times 100 \quad (2)$$

The percent perovskite phase increased with an increase in the calcining temperature.

The percent perovskite phase increased with an increase in the calcining temperature. A hundred percent of the perovskite phase was obtained at 800 °C which are given in

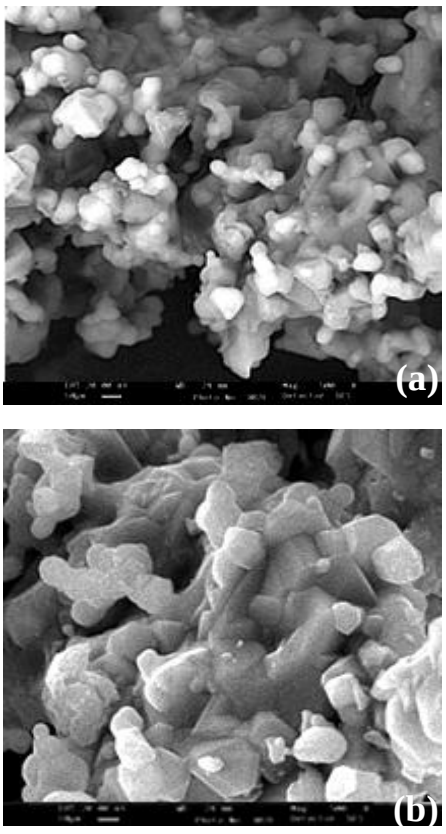


Figure 6. SEM morphology of ZT powders after heat treatment at 800 °C for different times: (a) 4 h and (b) 6 h

Fig. 8 The lattice parameter *c* tended to increase, while the lattice parameter *a* tended to decrease. Also, The *c/a* ratio increased with increased calcination temperatures as seen in Fig. 9.

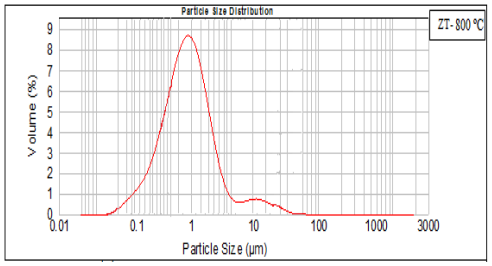


Figure 7. Particle size distribution curve of ZT-800 °C

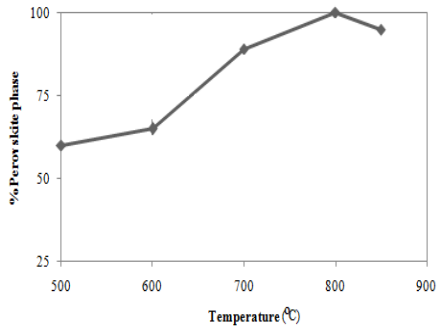


Figure 8. The percent perovskite phase of ZT powders with various calcinations temperatures

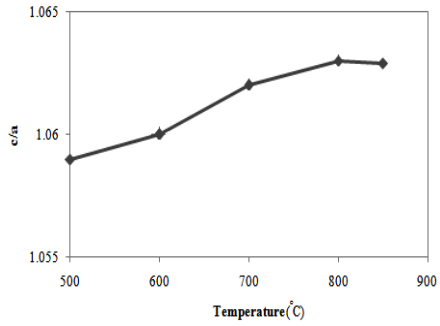


Figure 9. The *c/a* ratio of ZT powders with various calcination temperatures.

## 4. Conclusions

Perovskite $ZnTiO_3$ powders can be successfully obtained by the combustion technique and the best conditions for calcination is 800 °C. The calcination temperatures have a strong influence on the crystal structure, percent perovskite phase and the particle size of the ZT powders. Finally, presented SEM and X-ray analyses of ZT-800 °C showed advantageous microstructures, with the appropriate pores/ materials ratio and good candidates for application in the electronic industry as well as chemical industry as catalysts and colour pigments. Heat treatment at 800 °C for different times: 4 and 6 h enhanced the atomic mobility and caused the grain growth to result in a better crystallinity.

## References

[1] F.H. Dulin, D.E. Rase, Phase equilibria in the system $ZnO-TiO_2$, *J. Am. Ceram. Soc.* 43 (1960) 125–131.

[2] S.F. Bartram, R.A. Slepetys, Compound formation and crystal structure in the system $ZnO-TiO_2$, *J. Am. Ceram. Soc.* 1961, 44, 493–499.

[3] H.T. Kim, S. Nahm, J.D. Byun, Low-fired (Zn, Mg) $TiO_3$ microwave dielectrics, *J. Am. Ceram. Soc.* 82 (12) (1999) 3476–3480.

[4] H. Obayashi, Y. Sakurai, T. Gejo, Perovskite-type oxide as ethanol sensors. *J. Solid State Chem.* (1976), 17, 299–303.

[5] A.T. McCord, H.F. Saunder, Preparation of pigmentary materials. US Patent 2379019, 1945.

[6] O. Yamaguchi, M. Morimi, H. Kawabata, K. Shimizu, Formation and transformation of $ZnTiO_3$, *J. Am. Ceram. Soc.* 70 (1987) c97–c98.

[7] Y.S. Chang, Y.H. Chang, I.G. Chen, G.J. Chen, Y.L Chai, Synthesis and characterization of zinc titanate nano-crystal powders by sol-gel technique. *J. Cryst. Growth* 2002, 243, 319–326.

[8] J.H. Swisher, J. Yang, R.P. Gupta, Attrition-resistant zinc titanate sorbent for Sulfur. *Ind. Eng. Chem.* 1995, 34, 4463–4471.

[9] U. Steinike, B. Wallis, Formation and Strusture of Ti-Zn-Oxides. *Cryst. Res. Technol.* 1997, 32, 187–193.

[10] H. Idrissi, A. Aboujalil, J. P. Deloume, G. Fantozzi. Molten salt prepared lead titanate. *Journal of the European Ceramic Society*, 19(11), 1997-2004.

[11] K. C. Patil., S. T.Aruna, and S. Ekambaram, Combustion synthesis. *Current Opinion in Solid State & Materials Science*, (1997), 2(2), 156-l 65.

[12] E. Hosono, S. Fujihara, M. Onuki, T. Kimura, Low-temperature synthesis of nanocrystalline zinc titanate materials with high specific surface area. *J. Am. Ceram. Soc.* (2004), 87, 1785–1788.

[13] H.Kagata, T. Inoue, J. Kato, I. Kameyama, T. Ishizaki, Low-fire microwave dielectric ceramics. *Ceram. Trans.* (1993), 32, 81–90.

[14] B.D. Cullity, Elements of X-ray diffraction, 2nd Edition, Addison-Wesley Publishing Company, Inc., Reading, MA, 1978.

[15] N. Vittayakorn, G. Rujijangul, T. Tunkasiri, X. Tan, and D.P Cann.. Influence of processing conditions on the phase transition and ferroelectric properties of PZNPZT ceramics. *Material Science and Engineering B*, (2004) 108(3), 258-265.

Journal of New Technology and Materials
JNTM
Vol. 03, N°01 (2013) 37-42

OEB Univ. Publish. Co.

# Study on the use of different combined biopolymers for the microencapsulation of the probiotic bacteria *Lactobacillus curvatus* B431

*Houria Ouled-Haddar[a,b,*], Mohamed Sifour[a,b], Tayeb Idoui[b,c], Hamida Bouridane[a] and Somia Arid[a]*
[a]*Department of Cell and Molecular Biology, Faculty of Sciences, University of Jijel, Algeria*
[b]*Laboratory of Molecular Toxicology, Faculty of Sciences, University of Jijel, Algeria*
[c]*Laboratory of Biotechnology, Health and environment, Faculty of Sciences, University of Jijel, Algeria*
[*]*E.mail: Hrourou2002@gmail.com*

*Received: February 16, 2013; Revised: May 20, 2013; Accepted: June 16, 2013*

***Abstract***

*This study has focused on the confirmation of the protective role of microencapsulation of the probiotic lactic acid bacterium Lactobacillus curvatus B431 isolated from traditional butter by several matrixes against the hostile gastrointestinal tract conditions. The tolerance of Lb. curvatus to acidic pH, bile salts and pancreatic enzymes was evaluated. In addition, the effect of cold storage and heat treatment on viability was also tested. The results showed that the strain is resistant to low pH, bile salts, digestion by pancreatic enzymes, cold storage and heat treatment, particularly when encapsulated in sodium alginate. Microencapsulation of this strain in biopolymer enhanced the viability of probiotic strain in gastrointestinal-like conditions.*

***Keywords:*** *Biopolymer, alginate,Lactobacillus curvatus, microencapsulation, probiotic*

## 1. Introduction

Probiotics are microorganisms that transfer a variety of health benefits to the host and have numerous applications in food and medicine. Probiotic bacteria should be safe for consumption, reach the intestine alive in large numbers and provide specific health benefits to the host. These bacteria should maintain the balance of the intestinal flora by altering favorably the gut environment in such a manner that the growth of friendly beneficial bacteria are promoted and harmful disease causing organisms are inhibited [1]. Lactic acid bacteria (LAB) are the most important probiotic microorganisms typically associated with the human gastrointestinal tract. They are mainly used as starter cultures and play an important role in food preservation. They have the capacity to inhibit spoilage and pathogenic bacteria as a result of the drop in pH and antimicrobial activity of their metabolites such as lactic, acetic acid or bacteriocin; they also play an important role in microbiological stability and production of aroma compounds in various food products [2-5]. Beneficial effects depend on the ability of the probiotic strains to maintain viability in the food during shelf-life and to survive the natural defenses of the host and multiply in the gastrointestinal tract [6]. Many factors such as acidity, oxygen content, and concentration of lactic and acetic acids affect the survival of probiotics in food and in the gastrointestinal tract of the host. Several methods have been used to enhance the viability of probiotics, including selection of resistant strains, stress adaptation, incorporation of micronutrients, and microencapsulation [7]. Encapsulation is the most developed method for cell immobilizing which involves a large number of processes that entrap an active material in mainly spherical particles in order to immobilize it, protect it, control its release and provide new physical properties or functions. Immobilized cells have many advantages over free-cell cultures which include higher productivity as a result of high cell densities, long-term operational stability, improved control process, protection against contamination, improvement of plasmid stability and improvement of the ability to separate and reuse cells [8, 9].

The encapsulation is defined as the technology for packaging solids, liquid, or gaseous materials in capsules to protect the microencapsulated materials from the surrounding environment, or conversely to protect the environment from the active ingredient, while nutrients and products can migrate through the semi-permeable membrane of the capsule. Besides enhancing the viability of bacteria, microencapsulation facilitates handling of cells and allows a controlled dosage. The materials used for encapsulation consist of a semi-permeable, spherical, thin and strong membrane surrounding a solid or liquid core, with a diameter varying from a few microns to 1 mm. Polysaccharides like alginate, gellan, *k*-carrageenan and starch are the most commonly used materials in microencapsulation of bifidobacteria and lactobacilli [7, 9-11].

Microencapsulation of probiotic cells has been recently used as an efficient method for improving the viability of probiotic bacteria in fermented milk drinks, fermented frozen dairy desserts, ice-cream and juices, and simulated gastrointestinal tract [12]. Various researchers have studied the efficiency of encapsulation of *Lb. acidophilus* with

sodium alginate in calcium chloride ($CaCl_2$) to protect this organism from the harsh acidic conditions in gastric fluid [13-15].

The main purpose of this work was to investigate the effect of encapsulation with several biopolymers on the viability of a probiotic *Lactobacillus curvatus* B431 isolated from traditional butter.

## 2. Materials and Methods

### 2.1. Microencapsulation of bacterial strain in different biopolymers

The isolate used in this study was previously isolated from traditional butter and identified as *Lb. curvatus*. *Lb. curvatus* B431 was grown at 37°C in Man Rogosa Sharpe (MRS) broth (Biokar Diagnostics, France). To confirm the purity of the isolate the strain was streaked on MRS agar plates (MRS broth + 15g/L agar). *Lb. curvatus* B431 was cultivated in MRS broth at 37°C for 20h. Then the cells were harvested by centrifugation (4000g for 3 min) and washed twice with sterile normal saline and resuspended in normal saline, the final OD was 1.6 at 660 nm.

*Lb. curvatus* B 431 cells were microencapsulated using alginate (2 % w/v). Capsules containing the cells were prepared as follows: 80 mL of 2% sodium alginate (Louis Francois) was sterilized by autoclaving (121°C per 15min) and cooled to 40 )°C to which 20 mL of a freshly prepared cell suspension was added and homogenized using a magnetic stirrer (the final solution contained approximately $88.10^{11}$ CFU/mL). The resulting mixture was introduced into a sterile syringe (2.5ml) and was injected through a needle into 100 mL of $CaCl_2$ solution (0.05M+0.1%tween 80) previously autoclaved and cooled. The resulting beads formed were then left for 30 min to harden in the cross-linking solution, and then washed three times with sterile distilled water. Finally the beads were conserved in normal saline at 4°C for further utilization. On the other hand, 2% sodium alginate supplemented with 0.5 % modified starch (E 1442, Danone) was used for the encapsulation of *Lb. curvatus* B431 cells [16]. Furthermore, extrusion method was used for the encapsulation of *Lb. curvatus* B431 cells in 2% sodium alginate supplemented with 2 % agar-agar (Institut Pasteur- Alger) [17]. Finally, thermal gelation was employed to microencapsulate *Lb. curvatus* B431 in 2 % κ-carrageenan (Sigma) [18].

### 2.2. Effect of GIT-like conditions on the rate of cell release

The rate of cell release from the microcapsules was monitored as function of incubation time in GIT-like conditions by measuring OD $660_{nm}$ of the culture as described by Klinkenberg *et al.* [19]. The effect of acidic conditions on the kinetics of cell release was first tested by incubating 15 microcapsules of different materials in MRS broth (pH 2.0) for 3 hours at 37 °C; OD $660_{nm}$ was recorded at 1 hour intervals over the assay period. Cell release was also studied when microcapsules were incubated in MRS supplemented with 0.3% bile salts for 7 hours.

### 2.3. Evaluation of probiotic skills of *Lb. curvatus in vitro*

#### 2.3.1. Effect of acidic conditions on the survival of free and encapsulated *Lb. curvatus*

The effect of acidic conditions on the viability of free and microencapsulated cells of *Lb. curvatus* B431 was determined by incubating MRS broth (pH 2.0) inoculated with approximately $10^{10}$ CFU/mL (free or encapsulated cells) for 2 hours at 37 °C. A viable count on MRS agar was carried out at 1h intervals over the assay period after appropriate serial dilution in normal saline. The plates were incubated at 37 °C for 48 hours. For microencapsulated cells, the count was determined after lysis of the capsules in 2M phosphate buffer (pH 7.0). Samples were plated on MRS agar. The plates were incubated for 48 hours at 37 °C and the probiotic bacteria were enumerated as CFU/mL. Results were expressed in percent viability.

#### 2.3.2. Effect bile salts on the survival of free and encapsulated *Lb. curvatus*

To evaluate the effect of bile salts on the viability of free and microencapsulated cells of *Lb. curvatus* B431, approximately $10^{10}$ CFU/mL (free or encapsulated cells) were incubated in MRS broth supplemented with 0.3 % bile salts (Institut Pasteur, Alger) for 8 hours at 37 °C. A viable count on MRS agar was carried out at 1h intervals over the assay period after appropriate serial dilution in normal saline. The plates were incubated at 37 °C for 48 hours. For microencapsulated cells, the count was determined as described before.

#### 2.3.3. Survival of *Lb. curvatus* in simulated intestinal fluid

Simulated intestinal fluid (SIF) was prepared by dissolving bile salts 3 g/L, NaCl 9 g/L, pancreatin 10 g/L and trypsin 10 g/L in distilled water; pH was adjusted to 6.5 with NaOH [20]. An appropriate number of free and microencapsulated cells was used to inoculate the SIF, which was then incubated for 3 hours at 37 °C; a viable count on MRS agar was carried out at 1.5 h intervals over the assay period after appropriate serial dilution.

### 2.4. Effect of temperature and cold storage on the viability of free and encapsulated cells

The effect of temperature on the viability of *Lb. curvatus* was evaluted by incubating free and encapsulated cells at different temperatures (25 °C, 40 °C, 50 °C et 60 °C) for 20 minutes. A viable count was carried out before and after the incubation period [21]. For the effect of cold storage on the viability of free and encapsulated cells, the cells were stored in a refrigerator at 4±1 °C for two weeks and a viable count was carried out each week [22].

## 3. Results and discussion

The probiotic *Lb. curvatus* B431 was encapsulated in different matrices; and to make in evidence the presence of bacterial cells in the beads, microscopic examination of a thin section of an alginate capsule stained with the Gram stain was performed. The observation revealed the presence of lactobacilli in the encapsulation matrix.

The number of microencapsulated cells per bead was determined according to the method of Chàvarri *et al.* [23], after lysis of beads and enumeration of viable cells on MRS agar; results were expressed as CFU/ml. The yield of encapsulation (YE), which is a combination between the encapsulation efficiency and cell survival during the process of microencapsulation was calculated as follow:

$$YE = N/N^{\circ} \times 100 \quad \text{where}$$

N: the number of viable cells liberated from capsules
N°: the number of free cells added to the matrix.

The results of the encapsulation yields of studied matrices showed that encapsulation in alginate, agar and alginate-starch was less effective (30 and 50%), however alginate presented the highest yield (91.66%).

### 3.1. Effect of acidic conditions on the cell release

The test of cell release was realised to determine the capacity of matrices to retain cells within the beads. results showed that the release rate of cells after 3 hours of incubation in acidic conditions vary from a matrix to another (Figure 1). The release rate of cells from alginate beads increased slowly but remained relatively stable during 3h of incubation (OD=0.015). For Alginate-agar beads, the release rate increased progressively during 3h of incubation, while for alginate-starch beads the release rate was relatively stable during the 2 first hours of incubation and increased after that. We can conclude that the rate of release was the same for this two matrices after 3h of incubation (OD=0.03). However, for carrageenan beads, released rate increased rapidely during the incubation in acidic conditions and reached an OD of 0.043. The results indicated that carrageenan beads was the weakest matrix concerning the capacity to retain cells within the beads and alginate is the strongest gel.

We observed that the size of beads changed during the 3h of incubation as well as a progressive dissolution of carrageenan beads which can explain the increase in cell release, while alginate-based beads, shrunk and became rigid. As a result, we can conclude that acidic conditions affect the permeability of beads as a function of time, and we can classify polymers based on their release rate in acidic conditions (pH 2.0) in a decreasing order as follows: alginate, alginate-starch, alginate-agar and κ- carrageenan.

Immobilized cell systems are considered to be heterogeneous systems enclosing a continuous aqueous phase (microorganisms) and a dispersed phase (the matrix), the transfer of bacterial biomass is characterized by a flow through the membrane matrix which is controlled by the size and shape of the capsule, the porosity of the matrix and the capsule thickness, and the incubation of the beads formed by different matrices in a solution at low pH increases the rate of release of the cells by modifying the flow between the interior of the capsule and the outside environment [18].

Todorov *et al.* (2012) reported that after 2.5 h in solution simulating the stomach (pH 3.0), no counts of *Lb. plantarum* ST16Pa were obtained when they were encapsulated in alginate, indicating that the cells remained inside the capsules and were not affected by the low pH. In counterpart, the counts of free cells after the same treatment were 2 log lower than the initial counts [6].

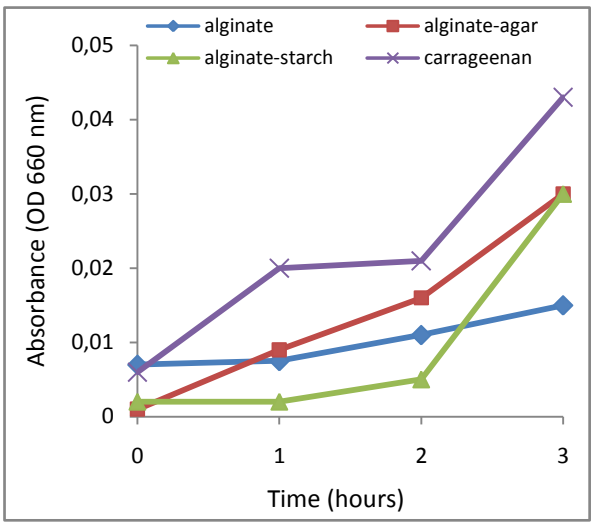


Figure 1. Effect of acidic conditions (pH 2.0) on the release of *Lb. curvatus* encapsulated in different matrices.

### 3.2. Release of cells from matrices in the presence of 0.3 % of bile salts

Results illustrated in Figure 2 represent the release rate of different matrices used for the encapsulation of *Lb. curvatus* in presence of bile salts. Cell release from alginate beads increased gradually during the incubation period and it reached an OD of 0.2 at the end of incubation. No cell release was observed during the first 3h of incubation from alginate-agar and carrageenan beads, where it increased gradually to reach approximatly 0.34 and 0.32 after 7 hours of incubation, respectively. On the other hand, alginate-Starch beads lost easily their content in the first three hours of incubation and after that they lost all of them rapidly after 5h of incubation to reach an absorbance of 0.37 at the end of the experiment.

In general, we observed a change in the size of the beads for the different matrices. Thus, for beads containing alginate (alone, alginate-agar and alginate-starch) there was a swelling with a softening over the experience time; while for κ-carrageenan, the gel undergoes significant dissolution in function of the time of exposure to bile salts.

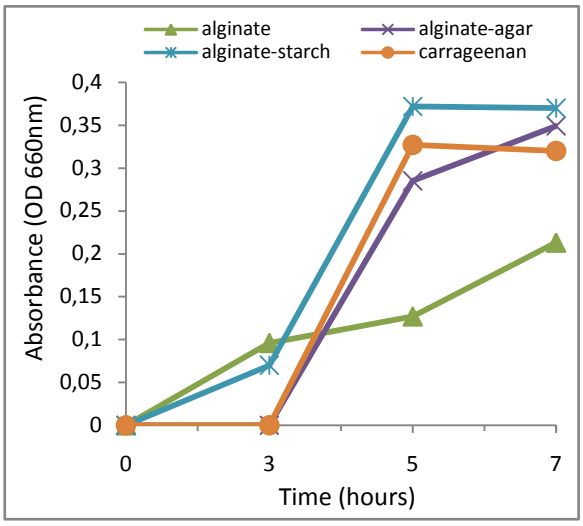


Figure 2. Effect of bile salts on the kinetic of cell release of *Lb. curvatus* B431 encapsulated in different matrices.

Similar results were reported by Todorov *et al.* [6] for alginate-based microencapsulated cells of *Lb. plantarum* ST16Pa when transferred from the low pH to the new stomach solution added of pancreatic components (digestive enzymes and bile salts), the protection given by the encapsulation weakened along exposure to this environment as the number of released cells increased gradually with time. However, the number of viable cells obtained for non-encapsulated *Lb. plantarum* ST16Pa was always lower than that recorded for their encapsulated counterparts.

Study of the effect of acidic conditions and bile salts on the release of cells from different matrices showed that 2% sodium alginate present an acceptable rate of release and it was selected for the study of the effect of the encapsulation on probiotic and technological properties of *Lb. curvatus* B431.

### 3.3. Evaluation of probiotic skills of *Lb. curvatus* B431 *in vitro*

#### 3.3.1. Tolerance of free and encapsulated *Lb. curvatus* to acid conditions

Bacteria used as probiotics supplements are usually delivered in a food system and will therefore begin their travel to the lower intestinal tract through the mouth, the time between the entry and release of the stomach is about 90 min. Although the cellular stress begins in the stomach, which has a pH as low as 1.5, most *in vitro* assays are carried out at pH 3.0. thus, the screening of all cultures studied for their tolerance to low pH of 2.0 and 3.0 is required. In addition, several studies indicated that bacteria do not survive in sufficient numbers during their passage through the gastrointestinal tract [24].

Free and alginate microencapsulated *Lb. curvatus* cells were subjected to acidic conditions in order to simulate the gastric juice effect. The obtained results are presented in Table1. The initial cell number was approximately $7x10^{10}$ CFU/ml for free cells and about $12x10^{10}$ CFU /ml for encapsulated cells. After 1hour of incubation in acid conditions (pH 2.0), the number of viable cells observed for the free form was $17x10^{4}$ CFU with a survival rate of 48% and after 2h of exposition to acid conditions, the number of viable cells decreased to reach $15x10^{3}$ CFU/ml which represent 38.4%. For the microencapsulated *Lb. curvatus* cells, a decrease in the number of viable cells was observed after 1 hours of incubation ($10^{7}$ CFU/ml) with a survival rate of about of 64%. The decrease in viable cells was continued to reach $58x10^{4}$ CFU/ml with a survival rate of 52% after 2h of incubation. The results suggest that microencapsulation of *Lb. curvatus* in 2% sodium alginate biopolymer protected efficiently this bacteria against acid conditions (pH 2.0) similar to those of stomach by increasing the survival of *Lb. curvatus* by about 14% after 2h of incubation.

| Time (h) / Survival rate (%) | 0 | 1 | 2 |
|---|---|---|---|
| Survival of encapsulated cells | 100 | 64 | 52 |
| Survival of free cells | 100 | 48 | 38 |

Table 1. Effect of acidic conditions (pH 2) on the survival of free and encapsulated *Lb. curvatus* B431.

Similarly, the counts of encapsulated *Lb. plantarum* ST16Pa after exposure to simulated gastric conditions (pH 1.6) for 3 h was 1.2 log lower than the initial count, while for non-encapsulated cells, a five-log reduction was observed [6]. Mandal *et al.* showed that the survival rate of *Lb. casei* NCDC-298 encapsulated in 2% sodium alginate was about 57% after 3 hours of incubation under acidic conditions [21].

#### 3.3.2. Tolerance of free and encapsulated *Lb. curvatus* to bile salts

Results in Table 2 showed that the initial cell number of both the free ($4x10^{10}$ CFU/ml) and microencapsulated forms ($7x10^{10}$ CFU/ml) decreased to reach $21x10^{6}$ CFU /ml (67% of survival) and $26x10^{7}$ CFU/ml (survival rate 78%) after 4 hours of exposition to 0.3% of bile salts, respectively. After 8 hours of incubation the cell number reached $24x10^{5}$ CFU/ml (survival rate 60%) for free cells and $9x10^{6}$ UFC/ml (survival rate 65%) for microencapsulated form. Based on the obtained results, microencapsulation in alginate biopolymer improved cell viability of *Lb. curvatus* by 5%.

It was reported that exposure to 1 and 2% oxbile for 12 h caused less than two log reduction in the counts of *Lb. plantarum* ST16Pa when encapsulated in 2, 3 or 4% alginate, while the number of non-encapsulated cells decreased five logs [6]. The survival of *Lb. plantarum* and *Lb. rhamnosus* was 68.6 and 65.4%, respectivly, after exposure to 3 % bile salts. Tolerance of probiotic to bile is very important because it displays a strong antimicrobial activity due to its action that

emulsifies and breaks down lipids of bacterial membranes [25].

| Time (h) / Survival rate (%) | 0 | 4 | 8 |
|---|---|---|---|
| Survival of encapsulated cells | 100 | 78 | 65 |
| Survival of free cells | 100 | 67 | 60 |

Table 2. Effect of bile salts (0.3%) on the survival of free and encapsulated *Lb. curvatus* B431.

### 3.3.3. Tolerance of free and encapsulated *Lb. curvatus* to simulated intestinal fluid

Because the pancreatic juice modifies the intestinal fluid, an experiment was carried out to study the viability of free and microencapsulated probiotic bacteria *Lb. curvatus* in these particular conditions by simulating the intestinal conditions through incubating both free and microencapsulated cells in a fluid containing pancreatic enzymes, bile salts, trypsine and NaCl for 3 hours. Results illustrated in Table 3 indicated that the survival of encapsulated cells decreased after 1.5 hours of incubation in the simulated intestinal fluid (survival rate 89.4%) and reached 51.4% after 3 hours of incubation. Despite of the slight protection of bacterial cells by microencapsulation, it was not very efficient since the improvement in cell viability was not important (6.7%) comparing with free cells which present a survival rate of 44.7% after 3 hours of incubation. It should be mentioned that an incomplete dissolution of alginate beads was observed and this could be attributed to the amylolytic activity of the pancreatic enzymes.

Comparing the effect of bile salts alone with the effect of simulated intestinal juice on the viability of encapsulated cells it appears that after exposure to simulated intestinal juice for 3 hours only, the survival rate is lower than that obtained after incubation with bile salts alone for 8 hours; hence, the relevance of this test proves that the pancreatic juice has a negative effect on the survival of this probiotic bacteria in the intestinal tract.

| Time (h) / Survival rate (%) | 0 | 1.5 | 3 |
|---|---|---|---|
| Survival of encapsulated cells | 100 | 89,4 | 51,4 |
| Survival of free cells | 100 | 86 | 44,7 |

Table 3. Effect of pancreatin on the survival of free and encapsulated *Lb. curvatus* B431.

The obtained results are similar to those obtained with *Lb. plantarum* CMU-FP002 encapsulated with 2% alginate and incubated for 3 h in the same solution of simulated intestinal fluid, where survival rate was of approximately 60% [20].

### 3.4. Evaluation of technological skills of *Lb.* curvatus in vitro

### 3.4.1. Effect of heat treatment on free and microencapsulated cells

As the main aim of the heat treatment is to inactivate harmful microorganisms and pathogens responsible for deterioration of food in order to extend its shelf life and food safety, it is inevitable to kill beneficial organisms that offer advantages over health. Therefore, it may be useful to use the microencapsulation to protect cells against heat treatments such as pasteurization, so we tested the resistance of free and encapsulated *Lb. curvatus* to heat treatment.

The results of the heat resistance test of free and encapsulated *Lb. curvatus* in different temperatures are illustrated in Figure 3. Cell viability of *Lb. curvatus* in the free form, showed a decrease in function of temperature increase, 83.72%, 65.48% and 46% of the cells survived after exposure to 40, 50 and 60 °C, respectively. In addition, encapsulated cells are more resistant and present the following survival rate: 90.9%, 78.65% and 52% for temperatures 40, 50 and 60 °C, respectively. Relatively low protection of *Lb. curvatus* cells was found by comparing the different values obtained in free or encapsulated, thereby protection was improved as follows: 7.13, 17 and 6% at 40, 50 and 60 °C, respectively.

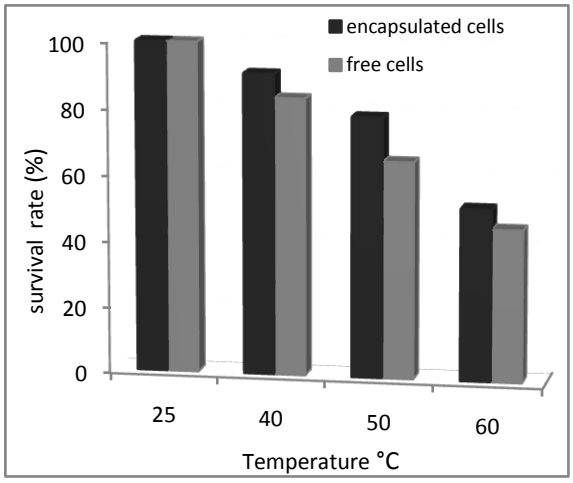


Figure 3. Effect of temperature on the survival of free and encapsulated *Lb. curvatus* B431.

In a similar report, *Lb. acidophilus* ATCC 43121 showed a survival rate of aproximately 90% when encapsulated in 2% alginate and exposed to 65°C for 30 min [26]. The effect of temperature on the strain *Lb.casei*

NCDC-296 encapsulated in alginate at various concentrations: 2, 3 and 4% was tested and results showed that the survival rate was of about 70, 75 and 82%, respectively [21], these finding are in agreement on the fact that 2% alginate significantly improves the viability of encapsulated cells of different species of *Lactobacillus* compared to free one.

### 3.4.2. Resistance to cold storage

As there is a significant loss of bacterial cells during storage, an experiment was conducted to evaluate the efficiency of encapsulation in 2% sodium alginate to reduce the loss of viability of probiotic caused by refrigeration; Table 4 illustrated the results obtained for *Lb. curvatus* after 15 days of storage at 4 °C. The results showed that free cells of *Lb. curvatus* are less resistant to storage at 4°C (66% were viable after two weeks of incubation) comparing with encapsulated form were the survival after two weeks remains relatively high (86% survived after two weeks). The microencapsulation was able to protect cells of *Lb. curvatus* against cold storage and the efficiency of the protection was equal to 20%.

| Time (week) / Survival rate (%) | 0 | 1 | 2 |
|---|---|---|---|
| Survival of encapsulated cells | 100 | 98 | 86,6 |
| Survival of free cells | 100 | 86 | 66 |

Table 4. Effect of cold storage at 4°C on the survival of free and encapsulated *Lb. curvatus* B431.

In a recent study, 75 % of the cells survived after 8 weeks of cold storage of *Lb. plantarum* CMUF-002 encapsulated in 2% alginate [20]. On the other hand, viability of immobilized cells of *Lb. plantarum* BL011 was greatly enhanced compared to the free microorganisms under refrigerated storage, and the treatments showing the lowest loss of viability were those of 4% (w/v) pectin, 3% (w/v) sodium alginate coated with chitosan and a mixture of 2% (w/v) sodium alginate and 2% (w/v) pectin, respectively [22].

## References


[1] G. Tiwari, R. Tiwari, S. Pandey, P. Pandey, *Chroni. Young Sci.*; 3 (2012) 17-27.

[2] S.D. Todorov, L.M.T.Discks, *World J. Microb. Biotech.* 21 (2005) 1585-1590.

[3] M. Sifour, T. Idoui, H. Ouled Haddar, H. Namous, S. Aissaoui, Online *J. Sci. Technol.* 2 (2012) 55-61.

[4] Mezaini A., Chihib N., Bouras AD., Naima N. and Hornez JP. J. Environ. *Public Health*; (2009) DOI: 10.1155/2009/678495.

[5] N. Saidi, M. Hadadji, B. Guessas, *Global J. Biotechnol. Biochem.* 6 (2011) 154-161.

[6] S.D. Todorov, J.G. Le-blanc, D.G.M. Franco, *World J. Microbiol. Biotechnol.* 28 (2012) 973-984.

[7] S. Rokka, P. Rantamäki, Eur. *Food Res. Technol.*; 231 (2010) 1-12.

[8] E. Ivanova, V. Chipeva, I. Ivanova, X. Dousset, D. Poncelet, *J. Culture Col.* 3 (2002) 53-58.

[9] J.W. Collins, R.M. La Ragione, M.J.D. Woodwar, L.E.J. Searle, Application of probiotic and prebiotic in livestock, In Prebiotics and Probiotics Science and Technology. Charalampopoulos D. and Rastall R A. (eds.) Springer, (2009) 1123.

[10] D. Patel, T. Parekh S. Rema, *Elec. J. Pharmacol. Therapy 1* (2008) 39-43.

[11] S. Prakash, A.M. Urbanska; *Biologics: Targets Therapy* 2 (2008) 355-378.

[12] P. Rosas-Ledesma, J.M. Leon-Rubio, F.J. Alarcon, MA. Morinigo, M.C. Balebona, *Aquaculture Res.* 43 (2012) 106-116.

[13] A.A. Kumar, H. Singh, *Trends Food Scien. Technol.* 18 (2007) 240-251.

[14] R.R. Mokarram, S.A. Mortazavi, H.M.B. Najafi, F. Shahidi. Food Res. Int. 42 (2009) 1040-1045.

[15] V. Chandramouli, K. Kailasapathy, P. Peiri, Jones M., *J. Microbiol. Methods* 56 (2004) 27-35.

[16] P. Boyaval, A. Lebrun, J. Goulet, Le Lait 65 (1985) 185-199.

[17] J.R. Morgan, M.L. Yarmush: Microencapsulation. In: Tissue Engineering Methods and Protocols, Chang T.M.S. (Ed.), Edition Humana Press, USA (1999) pp.317-330.

[18] R.H. Wijffels: Immobilised Cells, Springer and Verlag, Germany (2000).

[19] G. Klinkenberg, K.Q. Lystad, D.W. Levine, N. Dyrset, *J. Dairy Sci.* 84 (2001) 1118-1127.

[20] S. Woraharn, C. Chaiyasut, B. Sirithunyalug, J. Sirithunyalug, *Afr. J. Microbiol. Res.* 4 (2010) 2086-2093.

[21] S. Mandal, A.K. Puniya, K. Singh, *Int. Dairy J.* 16 (2006) 1190-1195.

[22] G. Brinques, M.A.Z. Ayub, *J. Food Eng.* 103 (2011) 123-128.

[23] M. Chávarri, I. Marañón, R. Ares, F.C. Ibáñez, F. Marzo, M.d.C. Villarán, *Int. J. Food Microbiol.* 142 (2010) 185–189.

[24] A.A. Khater, M.A. Ali, E.A.M. Ahmed, *J. American Sci.* 6 (2010) 836-845.

[25] W.K. Ding, N.P. Shah, *Food Microbiol. Safety* 74 (2009) 2.

[26] S.J. Kim, S.Y. Cho, S.H. Kim, O.J. Song, I.S. Shin, D.S. Cha et al., *LWT-Food Sci. Technol.* 41 (2008) 493-500 .

Journal of New Technology and Materials
JNTM
Vol. 03, N°01 (2013) 43-49

OEB Univ. Publish. Co.

# Height and Feature Parameters Study of thermally evaporated ZnS thin films By AFM

*Siham Trabishi, Roula Abou Samra and Imad Asaad*
*Department of Physics, Damascus University, Syria*

*Received: November 25, 2012, revised: April 11, 2013, accepted: June 30, 2013*

**Abstract**

*AFM has allowed to get microscopic information on the surface structure and to plot topographies representing the surface relief. In this work, this technique was used to visualize the surface relief, specify the growth, and determine Height parameters for form removed thermally evaporated Zinc Sulphide thin films such as root mean square height, Surface Skewness, Surface Kurtosis, Arithmetical mean height , Density of peaks and others. It can be seen on optical micrographs the fine grains with different sizes which are distributed over a smooth homogeneous background that may correspond to the amorphous, or polycrystalline phase of ZnS film. Some of the grains are seen to be united/fused- forming agglomerates. The surface roughness parameters were determined by using the software of ISO 25178 standard provided with the microscope.*

***Keywords:*** *Form removed surfaces (FR), roughness (R), waviness (W), root mean square height (RMS), Surface Skewness (Ssk), Surface Kurtosis (Sku), Arithmetical mean height (Sa), Density of peaks and Arithmetic mean peak curvature.*

## 1. Introduction

Zinc sulphide (ZnS) is an important (II-VI) semiconducting material with a wide direct band gap of 3.65eV in the bulk[1], a high refractive index (2.35) and high dielectric constant[2]. ZnS thin films with a wide direct band gap and n- type conductivity are promising candidates for optoelectronic device applications. These properties of zinc sulphide thin films are promising for short wavelength optoelectronic device applications. It has potential applications in optoelectronic devices such as blue light emitting diodes[3] ZnS can also be used for light emitting diodes in the blue ultraviolet region because of its wide band gap. ZnS is also widely used as the base materials for cathode-ray tube luminescent materials, catalysts, electroluminescent devices, and UV semiconductor lasers for optical lithography [4,5]. ZnS crystals are material having high photoluminescence and thermo –luminescence properties above room temperature. The nanostructures made up of ZnS materials find attractive applications in electronic and optoelectronic nano-devices [5],electroluminescent devices and photovoltaic cells[6]. In thin film solar cells based on CuGaIn (S.Se)2 absorbers, a CdS buffer layer is generally required in order to obtain high conversion efficiency. However, there are toxic hazards with respect to the production and use of the CdS layer. Therefore research in developing Cd-free buffer layers has been encouraged. This has lead to the investigation of ZnS as a buffer layer in ZnO/ZnS/CuInS2 devices[7]. ZnS has a wider energy band gap than CdS, which results in the transmission of more high energy photons to the junction and to the enhancement of the blue response to the photovoltaic cells.

Several techniques such as thermal evaporation [8], molecular beam epitaxy [9], metal-organic vapor phase epitaxy [10], chemical vapor deposition[11], spray pyrolysis[12], and chemical bath deposition CBD[13] have been used to produce ZnS thin films for photovoltaic applications because of its efficient, cost effective and large scale capability[15].

## 2. Theoretical study of roughness and surface parameters [16, 17, 18]

The Roughness of a surface is defined as the main components of the relief containing the smallest wavelengths measured on the sample. The roughness gives indication on the nature of the material and the machining type used. The wavelengths under the cut-off are kept in the roughness, the others, higher, are kept in the waviness.

The height properties, according to surf are described by six parameters, which give information about the statistical average properties, the shape of the height distribution histogram and about extreme properties. All the parameters are based on two-dimensional standards that are extended to three dimensions.

### A. Height Parameters (ISO 25178) (Surface)

Parameters related to roughness are general and valid for any M  N rectangular image.

Some of the parameters depend on the definition of a local minimum and a local maximum. Here, a local minimum is defined as a pixel where all eight neighboring pixels are higher and a local maximum as a pixel where all eight neighboring pixels are lower.

As there are no pixels outside the borders of the image there are no local minimums or local maximums on the borders. Note that parameters based on local minimums and/or local maximums may be more sensitive to noise than other parameters.

Height parameters are a class of surface finish parameters that quantify the Z-axis perpendicular to the surface. They are included in the ISO 25178 standard.

The reference plane for the calculation of these parameters is the mean plane of the measured surface.

***1. Root mean square height, $S_q$***

Standard deviation of the height distribution, or RMS surface roughness. It is defined as:

$$S_q = \sqrt{\frac{1}{MN}\sum_{k=0}^{M-1}\sum_{l=0}^{N-1}[z(x_k, y_l)]^2}$$

Computes the standard deviation for the amplitudes of the surface (RMS).

***2. The Surface Skewness or skewness of the height distribution, $S_{sk}$,*** is defined as:

$$S_{sk} = \frac{1}{MN\ S_q^3}\sum_{k=0}^{M-1}\sum_{l=0}^{N-1}[z(x_k, y_l)]^3$$

which is the third statistical moment, qualifying the asymmetry of the height distribution histogram. A negative $S_{sk}$ (Fig. 1a) indicates that the surface is composed with principally one plateau and deep and fine valleys. In this case, the distribution is sloping to the top. A positive $S_{sk}$ (Fig. 1b) indicates a surface with lots of peaks on a plane. The distribution is sloping to the bottom. Due to the big exponent used, this parameter is very sensitive to the sampling and to the noise of the measurement.

If $S_{sk}$ = 0, a symmetric height distribution is indicated, for example, a Gaussian like. If $S_{sk} < 0$, it can be a bearing surface with holes and if $S_{sk} > 0$ it can be a flat surface with peaks. Values numerically greater than 1.0 may indicate extreme holes or peaks on the surface.

***3. The Surface Kurtosis or Kurtosis of the height distribution, $S_{ku}$,*** is defined as:

$$S_{ku} = \frac{1}{MN\ S_q^4}\sum_{k=0}^{M-1}\sum_{l=0}^{N-1}[z(x_k, y_l)]^4$$

Which is the fourth statistical moment, qualifying the flatness of the height distribution. Due to the big exponent used, this parameter is very sensitive to the sampling and to the noise of the measurement.

For Gaussian height distributions $S_{ku}$ approaches 3.0 when increasing the number of pixels. Smaller values indicate broader height distributions and *visa versa* for values greater than 3.0.

A high kurtosis distribution has a sharper *peak* and longer, fatter *tails*, while a low kurtosis distribution has a more rounded peak and shorter thinner tails.

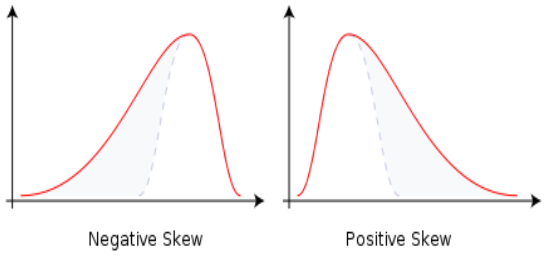


**Ku** a b

Figure 1.

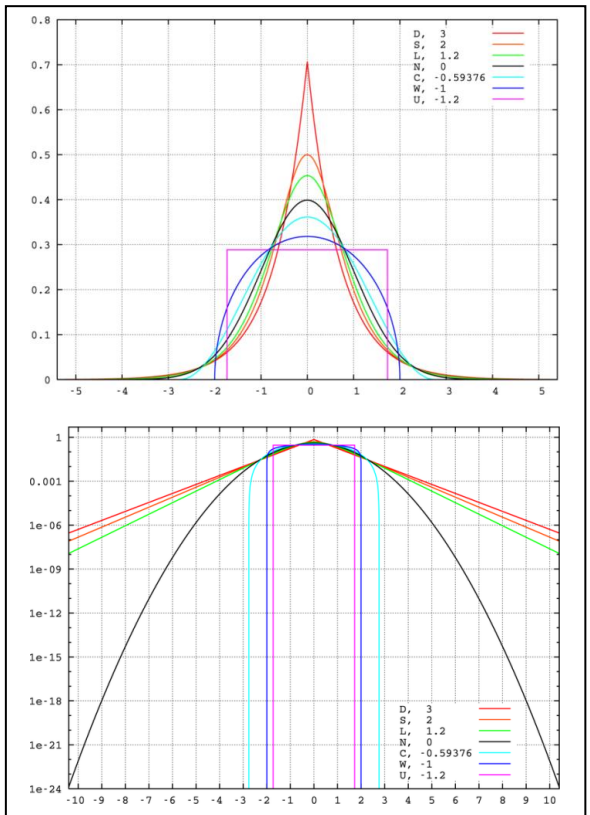


Figure 2. In this example we compare several well-known distributions from different parametric families.

***4. Maximum peak height, $S_p$,*** Height between the highest peak and the mean plane.

***5. Maximum pit height, $S_v$,*** Depth between the mean plane and the deepest valley.

***6. Maximum height, $S_z$***

Height between the highest peak and the deepest valley.

The definition of the (ISO 25178) Sz parameter is different from the definition of the (EUR 15178N) Sz parameter. The value of the (EUR 15178N) Sz parameter is always smaller than the value of the (ISO 25178) Sz parameter.

The (ISO 25178) Sz parameter replaces the (EUR 15178N) St parameter.

The **Peak-Peak Height,** are denoted by three parameter names, ***$S_z$, $S_t$, $S_y$***, according to ISO, ASME and reference [6]. They are defined as the height difference between the highest and lowest pixel in the image.

$$S_z = S_t = S_y = z_{\max} - z_{\min}$$

***7. Arithmetical mean height, $S_a$*** or Mean surface roughness is defined as

$$S_q = \frac{1}{MN}\sum_{k=0}^{M-1}\sum_{l=0}^{N-1}|\ z(x_k, y_l)\ |$$

**B. Theoretical study of Feature parameters [16, 17, 18]**

The feature parameters are a new family of parameters that is integrated in the ISO 25178 standard. Feature parameters are derived from the segmentation of a surface into motifs (hills and dales). Segmentation is carried out in accordance with the watersheds algorithm

For the moment, all feature parameters are calculated after a discrimination by segmentation using a Wolf pruning of 5% of the value of the Sz parameter (Maximum height).

***1. Density of peaks, $S_{pd}$,*** Number of peaks per unit area.

$$S_{pd} = \frac{Number\ of\ local\ Maximums}{(M-1)(N-1)\delta x \delta y}$$

Because, the parameter is sensitive to noisy peaks it should be interpreted carefully.

The peaks taken into account for the (EUR 15178N) $S_{dc}$ parameter are detected by local neighbourhood (with respect to 8 neighbouring points) without discrimination between local and significant peaks. The (ISO 25178) $S_{pd}$ parameter is calculated the same way, but takes into account only those significant peaks that remain after a discrimination by segmentation (Wolfpruning of 5% of Sz). Therefore the value of the (ISO 25178) $S_{pd}$ parameter is smaller than the value of the (EUR 15178N) $S_{dc}$ parameter.

***2. Arithmetic mean peak curvature, $S_{pc}$ (Mean Summit Curvature, $S_{sc}$, according to SPIP)*** Arithmetic mean of the principle curvatures of peaks within a definition area. It is defined as:

$$S_{pc} = \frac{-1}{2n}\sum_{i=1}^{n}\left(\frac{\delta^2 z(x,y)}{\delta x^2}\right)+\left(\frac{\delta^2 z(x,y)}{\delta y^2}\right)$$

for all local maximums , where $\delta x$ and $\delta y$ are the pixel separation distances. This parameter enables to know the mean form of the peaks: either pointed, either rounded, according to the mean value of the curvature of the surface at these points.

The peaks taken into account for the (EUR 15178N) $S_{sc}$ parameter are detected by local neighbourhood (with respect to 8 neighbouring points) without discrimination between local and significant peaks. The (ISO 25178) $S_{sc}$ parameter is calculated the same way, but takes into account only those significant peaks that remain after a discrimination by segmentation (Wolf pruning of 5% of $S_z$). Therefore the value of the (ISO 25178) $S_{sc}$ parameter is more accurate and significant than the value of the (EUR 15178N) $S_{sc}$ parameter.

There are three hybrid parameters. These parameters reflect slope gradients and their calculations are based on local z-slopes.

***3. Ten point height, $S_{10z}$.*** Average value of the heights of the five peaks with the largest global peak height added to the average value of the heights of the five pits with the largest global pit height, within the definition area.

$$S_{10z} = S_{5p} + S_{5v}$$

$$\text{or} \quad S_{10z} = \frac{\sum_{i=1}^{5}|z_{pi}| + \sum_{i=1}^{5}|z_{vi}|}{5}$$

where $z_{pi}$ and $z_{vi}$ are the height of the $i^{th}$ highest local maximums and the $i^{th}$ lowest local minimums respectively. When there are less than five valid maximums or five valid minimums, the parameter is not defined.

***4. Five point peak height, $S_{5p}$.*** Average value of the heights of the five peaks with the largest global peak height, within the definition area.

***5. Five point pit height, $S_{5v}$.*** Average value of the heights of the five pits with the largest global pit height, within the definition area.

***6. Closed dale area, $S_{da}$.*** Mean dale area Average area of dales connected to the edge at height c.

***7. Closed hill area, $S_{ha}$.*** Mean hill area Average area of hills connected to the edge at height c.

***8. Closed dale volume, $S_{dv}$.*** (Mean dale volume) Average volume of dales connected to the edge at height c.

***9. Closed hill volume, $S_{hv}$.(mean hill volume)*** Average volume of hills connected to the edge at height c.

## 3. Experiments and AFM Characterization

Thin films of ZnS films were deposited on glass substrates by thermal evaporation. Experimental evidence and analytical studies of the XRD patterns and optical characterizations of ZnS films with different optical thicknesses had been reported previously [19]. In this work, I used AFM technique to get microscopic information on the surface structure, to plot topographies representing the surface relief , specify the growth, and determine the contribution of optical thickness to the quality of the film. The study of height parameters was carried out by contact and dynamic modes of AFM. The optical photos of 3different thicknesses, whose sizes are of (500µm*370µm), show, high in-homogeneity of crystallite sizes. The thicker the sample, the larger the crystallite size is. Fig.3 shows an optical micrograph of zinc sulphide thin films of 300nm thickness, grown on glass substrate.

Before the calculation of the roughness parameters, I carried out a slope correction by a 2nd order polynomial plane fit. Components of the surface relief of long horizontal wavelengths have been removed in order to analyze surface finish (i.e. waviness and roughness). As the Form in our samples is coming from a smooth material (thin films), 2nd order polynomial plane fit Form Removal operator has been used for slope correction. **Gaussian Filtering (**with 0.25 µm cut-off wavelength**) has been used to** separate data frequencies (or wavelengths) into two parts, the first one having the long wavelengths (waviness), the other one having the short wavelengths (roughness).

The wavelengths above the cut-off are kept in the waviness whereas the others, smaller, are kept in the roughness.

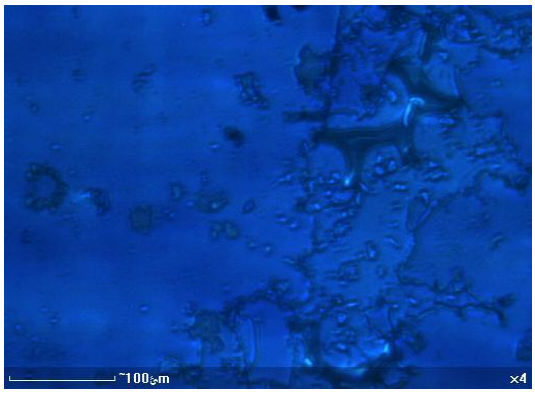


Figure 3. An optical micrograph for (500µm*370µm) area of thermally evaporated ZnS film, of 300nm thickness, grown on glass substrate.

Figs.4,5,6 illustrate the topographies of zinc sulphide thin films of 300, 200, 50nm thickness respectively. Each figure contains 3D AFM view of denoised, form removed surface, and Gaussian filtered roughness for one point of each film. The table in each figure contains the Height Parameters of form removed (FR) surface, it's roughness and waviness in several points of the concerned film.

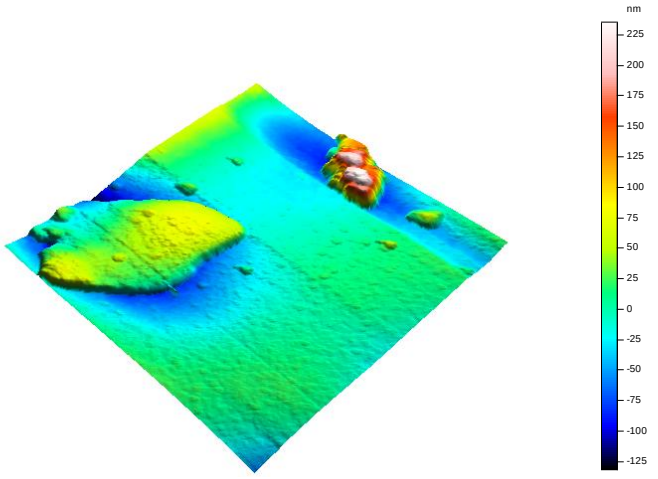


FR surface P3

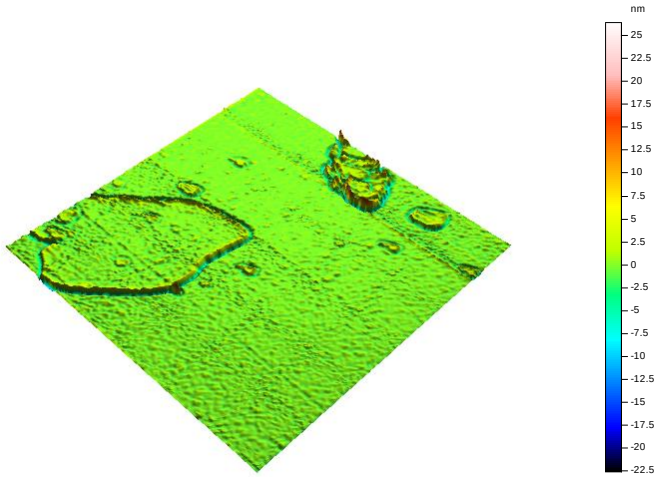


Gaussian filtered roughness P3

| ISO 25178 Height Parameters 300nm thickness | | | | |
|---|---|---|---|---|
| | | FR | R | W |
| $S_q$ | P1 | 113 nm | 3.95 nm | 0.111 µm |
| | P2 | 2.56nm | 0.385nm | 2.24 nm |
| | P3 | 41.4 nm | 1.51 nm | 40.8 nm |
| | P4 | 2.86 nm | 0.433nm | 0.433 nm |
| $S_{sk}$ | P1 | -0.122 | -1.32 | -0.123 |
| | P2 | 6.15 | 0.466 | 7.12 |
| | P3 | 1.47 | -1.28 | 1.49 |
| | P4 | 5.9 | 0.57 | 0.57 |
| $S_{ku}$ | P1 | 4.9 | 45.3 | 4.01 |
| | P2 | 75.7 | 13.9 | 95.2 |
| | P3 | 8.66 | 40.1 | 8.71 |
| | P4 | 75 | 8.73 | 8.73 |
| $S_p$ | P1 | 443 nm | 68.8 nm | 0.361µm |
| | P2 | 39.9 nm | 4.77 nm | 39.1 nm |
| | P3 | 235 nm | 26.4 µm | 0.233 µm |
| | P4 | 45.5 nm | 4.85 nm | 4.85 nm |
| $S_v$ | P1 | 518 nm | 66.7 nm | 0.499µm |
| | P2 | 8.99 nm | 5.54 nm | 8.47nm |
| | P3 | 132 nm | 22.6 nm | 0.128 µm |
| | P4 | 9.79 nm | 4.17 nm | 4.17 nm |
| $S_z$ | P1 | 961 nm | 135 nm | 0.86µm |
| | P2 | 48.9 nm | 10.3 nm | 47.6 nm |
| | P3 | 367 nm | 49 nm | 0.362 µm |
| | P4 | 55.3 nm | 9.02 nm | 9.02 nm |
| $S_a$ | P1 | 81 nm | 1.63 nm | 0.0802µm |
| | P2 | 1.42 nm | 0.275 nm | 1.15 nm |
| | P3 | 28.4 nm | 0.000705 | 0.028 µm |
| | P4 | 1.63 nm | 0.321 nm | 0.321 nm |

Figure 4. 3D view of denoised, form removed surface and Gaussian filtered of AFM photo for point P3 of 300nm thickness thin film of ZnS. The Table indicates the Height Parameters of form removed (FR) surface, roughness (R) and waviness (W) in four points (P1, P2, P3, P4) of the 300nm thickness film.

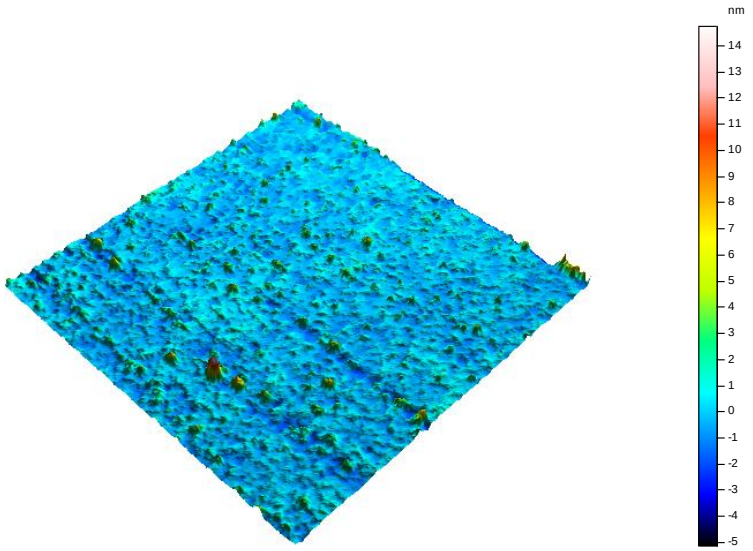


FR surface P4

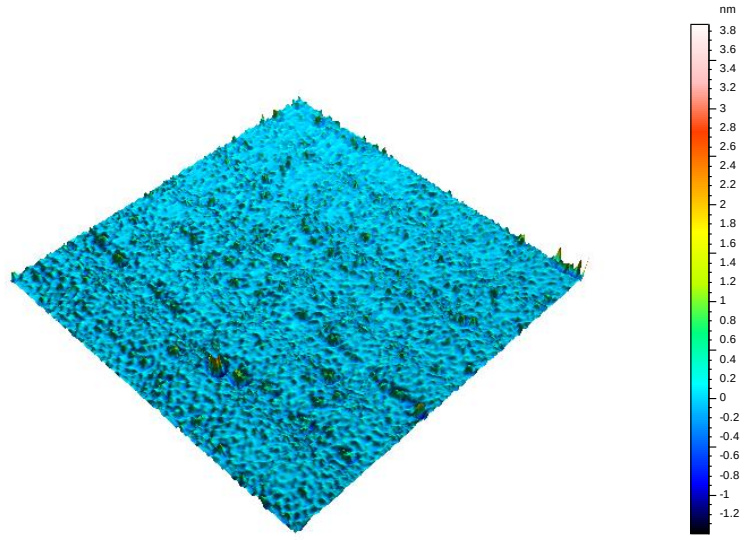


Gaussian filtered roughness P4

| ISO 25178 | | | | |
|---|---|---|---|---|
| Height Parameters | | | | |
| 200nm | | | | |
| | | FR | R | W |
| $S_q$ | P1 | 3.1 nm | 0.369 nm | 2.87 nm |
| | P2 | 1.56 nm | 0.362 nm | 1.19 nm |
| | P3 | 10.9 nm | 0.402 nm | 10.6 nm |
| | P4 | 0.845 nm | 0.193 nm | 0.65 nm |
| $S_{sk}$ | P1 | 8.41 | 0.267 | 9.51 |
| | P2 | 1.06 | 0.584 | 1.04 |
| | P3 | 12.7 | 1.6 | 12.7 |
| | P4 | 3.02 | 1.35 | 3.3 |
| $S_{ku}$ | P1 | 119 | 12.6 | 143 |
| | P2 | 5 | 4.03 | 5.69 |
| | P3 | 253 | 184 | 254 |
| | P4 | 30.1 | 15.2 | 37.3 |
| $S_p$ | P1 | 52.9 nm | 3.63 nm | 52.3 nm |
| | P2 | 9.79 nm | 2.43 nm | 8.49 nm |
| | P3 | 238 nm | 13.3 nm | 236 nm |
| | P4 | 14.7 nm | 3.87 nm | 12.5 nm |
| $S_v$ | P1 | 8.24 nm | 5.04 nm | 7.63 nm |
| | P2 | 3.86 nm | 1.48 nm | 3.26 nm |
| | P3 | 53.9 nm | 11.4 nm | 52.3 nm |
| | P4 | 5.13 nm | 1.4 nm | 3.09 nm |
| $S_z$ | P1 | 61.1nm | 8.67 nm | 60 nm |
| | P2 | 13.7 nm | 3.91 nm | 11.7 nm |
| | P3 | 292 nm | 24.7 nm | 288 nm |
| | P4 | 19.9 nm | 5.27 nm | 15.6 nm |
| $S_a$ | P1 | 1.51 nm | 0.253 nm | 1.28 nm |
| | P2 | 1.19 nm | 0.276 nm | 0.903 nm |
| | P3 | 3.61 nm | 0.162 nm | 3.55 nm |
| | P4 | 0.551 nm | 0.135 nm | 0.425 nm |

Figure 5. 3D view of denoised, form removed surface and Gaussian filtered of AFM photo for point P4 of 200nm thickness thin film of ZnS. The Table indicates the Height Parameters of form removed (FR) surface, roughness (R) and waviness (W) in four points (P1, P2, P3, P4) of the 200nm thickness film.

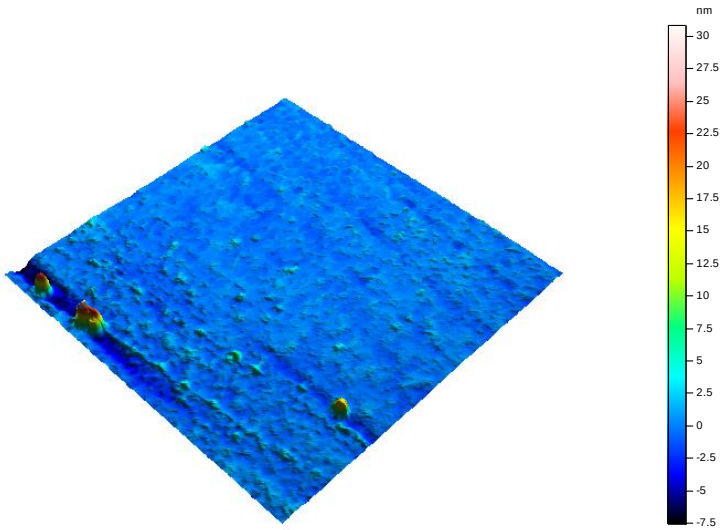


FR surface P2

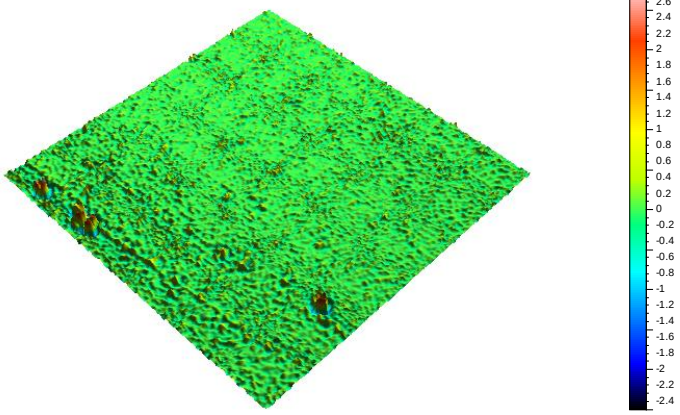


Gaussian filtered roughness P2

| ISO 25178 Height Parameters 50nm | | | | |
|---|---|---|---|---|
| | | FR | R | W |
| ***Sq*** | P1 | 4.42 nm | 0.488 nm | 4 nm |
| | P2 | 1.55 nm | 0.201 nm | 1.39 nm |
| | P3 | 2.36 nm | 0.33 nm | 2.16 nm |
| ***Ssk*** | P1 | 5.94 | -0.918 | 6.53 |
| | P2 | 7.79 | 1.36 | 8.18 |
| | P3 | 13.7 | 0.278 | 14.1 |
| ***Sku*** | P1 | 83.4 | 46 | 94.7 |
| | P2 | 115 | 29 | 124 |
| | P3 | 243 | 222 | 256 |
| ***Sp*** | P1 | 77.3 nm | 8.76 nm | 73 nm |
| | P2 | 30.8 nm | 3.36 nm | 28.5 nm |
| | P3 | 51.8 nm | 10.9 nm | 50.4 nm |
| ***Sv*** | P1 | 23.5 nm | 8.33 nm | 20.9 nm |
| | P2 | 7.58 nm | 2.51 nm | 7.21 nm |
| | P3 | 5.79 nm | 10.7 nm | 5.17 nm |
| ***Sz*** | P1 | 101 nm | 17.1 nm | 93.9 nm |
| | P2 | 38.4 nm | 5.87 nm | 35.7 nm |
| | P3 | 57.6 nm | 21.5 nm | 55.5 nm |
| ***Sa*** | P1 | 1.78 nm | 0.241 nm | 1.59 nm |
| | P2 | 0.699 nm | 0.129 nm | 0.587 nm |
| | P3 | 0.746 nm | 0.144 nm | 0.632 nm |

Figure 6. 3D view of denoised, form removed surface and Gaussian filtered of AFM photo for point P2 of 50nm thickness thin film of ZnS. The Table indicates the Height Parameters of form removed (FR) surface, roughness (R) and waviness (W) in three points (P1, P2, P3) of the 50nm thickness film.

## 4. Discussion & Conclusion

Investigation of the Gaussian filtered roughness Height Parameters of form removed surfaces for 3 different thicknesses of ZnS film shows that they depend highly the film thickness, and even they vary from point to the other on the same film. The root mean square (RMS) $S_q$ of the roughness on the 300nm thickness film is positioned between 0.00395 μm and 0.385nm, (table of Fig4), between 0.402 nm and 0.193nm (table of Fig5) and between 0.488 nm and 0.201nm (table of Fig6) in the scanned range areas.

Investigating skewness **height distribution,** $S_{sk}$ values in tables of Figs 4, 5, 4 shows that each of the films may include areas with positive surface skewness and others with negative surface skewness, indicating that surface is composed of peaks and holes on a plane. Though the parameter is very sensitive to sampling I didn't notice a big difference between the examined areas.

Examining Kurtosis of the height distributions, $S_{ku}$ in the tables mentioned above, indicates that they are in most cases much greater than 3, indicating sharp peaks and long tails especially in the 50 nm thick film, where surface Kurtosis values are positioned between 29 and 222.

Examining the Density of peaks, $S_{pd}$ of the roughness surface on the 300nm thickness film in the table below, we notice that it is positioned between 518387 1/μm2 and 8620587 1/μm2, for the 200nm thickness between 124561 1/μm2 and 11948300 1/μm2 , and for 50nm between 182051 1/μm2 and 3966797 1/μm2 in the scanned range areas.

Regarding the **Arithmetic mean peak curvature,** $S_{pc}$ values, the table shows that they vary from 0.496 1/μm to 9.01 1/μm(for300nm), from 0.298 1/μm to 1.71 1/μm(for200nm) and from 0.314 1/μm to 1.65 1/μm (for50), which indicates

the sensitivity of this parameter to film thickness, at least in the examined areas.

Values of Height and Feature parameters of ZnS thin films should be controlled according to the application sought after, transmission or reflection or fluid retention.

## References


[1] X.D. Ago, X.M Li, W.D.Yu, *Thin Solid films* 468 (2004)43.

[2] J. Cheng, D. Fan, H. Wang, B. W. Liu, *Semicond. Sci. Technol.* 18 (2003)676

[3] S.H. Deulkar, C.H. Bhosaile, M. Sharon, *J. Phys. Chem. Solids* 65(2004)1879.

[4] L. thamizhmani, A. K. Azad, J. Dai, W. Zhang, *Appl. Phys. Lett.* 86 (2005) 131111.

[5] A. N. Yazici, M. Oztas, M. Bedir, *J. Luminescence* 104 (2003)115.

[6] J.Vidal, O.De.Melo, O.Vigil, N.Lopez, G.Contreras-Puente. O.Zelaya-Angel. *Thin Solid films* 419(2002)118

[7] R.O. Borges, D. Lincot, J.Videl, Proceedings of eleven European Photovoltaic Solar Energy Conference, Montreux, Switzerland, October (12-16 1992, p.862.

[8] Z. Porada, E. Sch(1986)75.abowska, *Thin solid films* 145

[9] M. Yoneta, M.Ohishi, H. Saito, *J. Cryst. Growth* 127(1993)314.

[10] A. Aboundi, M. Diblasio, D. Bouchara, *Phy. Rev.*, B 50(1994) 11677.

[11] H. Kashani, *Thin Solid Films* 288 (1996) 50.

[12] R. R. Chanberlin, J. S. Skarman, *J. Electrochem. Soc.* 113 (1966)86

[13] P.K Nair, M. T. S. Nair, *Semicond. Sci. Technol.* 7(1992)239.

[14] K.R. Murali, S. Vasantha, K. Rajamma, Properties of pulse plated ZnS films, *Materials Letters* 62(2008) 1623-1826.

[15] Compositional, structural, and Optical study of nanocrystalline ZnS thin films prepared by a new chemical bath deposition route, R. Sahraei, et al., *J. Alloys and Compd.* (2008)

[16] surf manual

[17] spip manual

[18] Wikipedia, the free encyclopedia

[19] *Eur. Phys. J. Appl. Phys.* 52, 30301 , DOI: 10.1051/epjap/2010162 (2010)

Journal of New Technology and Materials
JNTM
Vol. 03, N°01 (2013) 50-55

OEB Univ. Publish. Co.

# Tensile and Flexural Strengths of Coconut Shell Particle & Coir Fibre Reinforced Composite

[1]Jitendra Bhaskar and [2]V.K.Singh
[1]Associate Professor
Department of Mechanical Engineering Harcourt Butler Technological Institute, Kanpur-208002 India
[2]Associate Professor
Department of Mechanical Engineering College of technology
G.B.Pant University of Agriculture& Technology, Pantnagar-263145, Uttarakhand, India
Email :vks2319@yahoo.co.in

Received: October 21, 2012, revised: June 22, 2013 accepted: June 30, 2013

**Abstract**

*This paper presents the tensile and flexural strengths of coconut shell particle and coir fibre reinforced wood composite. The composites material were fabricated by reinforcing coconut shell particle (size between 200-800μm) by 17- 28 wt% and coir fibre (2-5mm) by 2-3 wt% into epoxy matrix using open mould casting method. Microscopic investigations were done for estimating properties. Experimental results showed that ultimate strength, modulus of elasticity, % elongation decreases with wt% of shell particle. Ultimate strength and % elongation increases but modulus of elasticity decreases with the increase of coir wt%. Modulus of elasticity decreases with the reinforcement of shell particle and coir both. Flexural strength decreases with addition of coir fibre. The coconut shell particles and coir fibers are good reinforcing of 30 wt% materials to reduce the consumption of resin as well as utilizing waste natural material with maintaining the properties required for structural applications. The open mould casting method used has been proved to be easy way of composite material preparation.*

**Keywords:** *Bio materials, Composites, Mechanical Properties, Thermosets.*

## 1. Introduction

Composites consist of one or more discontinuous phases embedded in a continuous phase. The discontinuous phase is usually harder and stronger than the continuous phase and is called the 'reinforcement' or 'reinforcing material', whereas the continuous phase is termed as the 'matrix'. Properties of composites are strongly dependent on the properties of their constituent materials, their distribution and the interaction among them. The geometry of the reinforcement (shape, size and size distribution) influences the properties of the composite to a great extent.

Natural fillers and fibers reinforced thermoplastic composite have successfully proven their high qualities in various fields of technical application. As replacements for conventional synthetic fibers like aramid and glass fibers are increasingly used for reinforcement in the thermoplastic due to their low density, good thermal insulation and mechanical properties, reduced tool wear, unlimited availability, low price, and problem free disposal. Wood fibers/particles provide a sufficient reinforcement at much lower cost than synthetic and mineral filled thermoplastic. When the synthetic and mineral fibers are used, machine wears and damages of processing equipment is much higher than with wood filler. Fiber damage during processing is greatly reduced when wood is utilized, which allows for recycling production waste without compromising quality [1].

Luo and Netravali [2], Ahmed [3], Faud [4], Schneider [5], and bhaskar [6] studied pineapple, filament wound cotton fibre, oil palm wood flour and jute & kenaf fiber based composite respectively.

Coconut shell is one of the most important natural fillers produced in tropical countries like Malaysia, Indonesia, Thailand, Sri Lanka and India. Many works have been devoted to use of other natural fillers in composite in recent past and coconut shell filler is a potential candidate for the development of new composites because of their high strength and modulus properties. The coconut particles also have remarkable interest in the automotive industry owing to its hard-wearing quality and high hardness (not fragile like glass fiber), good acoustic resistance, moth-proof, not toxic, resistant to microbial and fungi degradation, and not easily combustible.

Composite of high strength coconut filler can be used in broad range of applications as, building materials, marine cordage, fishnets, furniture, and other household appliances [7-8]. The objective of this paper is to investigate the density and tensile properties of epoxy composite based coconut shell filler particles.

As the name itself indicates, the reinforcement is of particle nature (platelets are also included in this class). It may be spherical, cubic, tetragonal, a platelet, or of other regular or irregular shape, but it is approximately equiaxed. In general, particles are not very effective in improving fracture resistance but they enhance the stiffness of the composite to a limited extent. Particle fillers are widely used to improve the properties of matrix materials such as to modify the thermal and electrical conductivities, improve performance at elevated temperatures, reduce friction,

increase wear and abrasion resistance, improve machinability, increase surface hardness and reduce shrinkage. Particles are more commonly used as extenders to lower the polymer use with other simultaneous improvement in properties.

## 2. Materials

### 2.1. Epoxy Resin

Epoxy resins (ER) are one of the most important classes of thermosetting polymers which are widely used as matrices for fiber-reinforced composite materials and as structural adhesives [1, 2, 3, 4, 9]. They are amorphous, highly cross linked polymers and this structure results in these materials possessing various desirable properties such as high tensile strength and modulus, uncomplicated processing, good thermal and chemical resistance, and dimensional stability [1]. However, it leads to low toughness and poor crack resistance, which should be upgraded before they can be considered many end-use applications [1, 2].

In the present investigation epoxy resin SY-12(319) purchased from M/s RESINOVA CHEMIE Limited, Kanpur India has been used as matrix material. The epoxy used is colourless, odorless and completely nontoxic. Tensile, modulus of elasticity compressive, flexural, and impact strengths are 43 MPa, 800-820 kg/mm$^2$, 90-100 MPa, 50-60 MPa, 2.5-4 kg-cm/cm$^2$ respectively. Density is 1.15 g/cm$^3$. It has versatile applications in technical and industrial applications. Curing takes place at room temperature and atmospheric pressure after addition of hardener. Fully cured mixture has excellent mechanical, thermal properties and atmospheric attack. The castings have good ageing characteristics.

### 2.2. Hardener

Hardener SY31(B) is a yellowish-green liquid. Hardener SY31(B) purchased from M/s RESINOVA CHEMIE Limited, Kanpur, India has been used as curing agent. In the present investigation 8 % wt/wt has been used in all material developed. Specific viscosity of hardener is 10-20 cps. The weight percentage of hardener used in the present investigation is as per recommendation of Singh [9].

### 2.3. Coconut shell particle

Coconut shell particles were used as reinforcing material for investigation as shown in figure 1(a) prepared from coconut shell as shown in figure 1(b). Shell particles of size between 200-800 μm were prepared by grinding machine. Coconut shell filler are potential candidates for the development of new composites because of their high strength and modulus properties. An approximate value of coconut shell density is 1.60 g/cm$^3$.

### 2.4. Coir fiber

Coconut fruit is covered inside coconut coir fiber. Fibers are very long and have good tensile properties as shown in figure 1(c). It is assumed that cover of fibre gives damping strength to the coconut fruit for protecting while falling from height. Fibers used were collected and milled to get fine form of coir fiber.

## 3. Composite fabrication

The measured quantity of resin, coconut shell particle and coir fibre were mixed according to required quantity of reinforcement 20 wt% to 30 wt% was kept in the furnace at a temperature of 90±5 $^0$C for two hours as per the recommendation of Singh [10]. At each interval of 30 minutes the solution was remixed by mechanical stirrer at high speed. After two hours the whole solution was allowed to cool to a temperature of 45 °C. When a temperature of 45°C was attained 8 wt% of the hardener was mixed immediately. Due to addition of hardener high viscous solution was obtained which was again mixed mechanically by high speed mechanical stirrer. The viscous solution so obtained was poured in to different moulds for sample preparation for tensile testing.

The viscous solution obtained from resin, hardener and filler materials is poured in to different moulds for specimen preparation for tensile and flexural strength test and casted material is shown in figure 1(d). Flat plates as required for tensile test. Tensile test specimens were prepared on milling machine as per ISO 527-2(1996).

Figure 1(a). Coconut shell particles

Figure 1(b). Coconut shell

Figure 1(c). Coconut coir fiber particle

Figure 1(d). Prepared composite plates

## 4. Experiments

### 4.1. Microscopic Investigation

The scanning electron micrograph study generally performed by scanning electron microscope, which uses electron to form an image with high resolution or magnification. To obtain the topographical contrast of the morphology of the organic-inorganic samples were etched. In etching 'weakest' compound is removed, while the 'strongest' compound remains at the surface, thus creating a topographical difference. The organic phase was etched away, without affecting inorganic particles present in the material. The inorganic phase is much better visible when etching was used.

In the present investigation SEM studies has been done to see the dispersion of coconut shell particle and coir fibre. The images were obtained through microscopic investigation. To obtain the scanning electrons micrographs square samples were cut and gold coated to avoid the artifacts associated with sample charging and then placed inside a chamber in which an electron beam was falling on the material. The accelerated voltage was 20 kV. Different images are taken at various magnification ranges.

### 4.2. Tensile test

Tensile tests were performed to determine the modulus of elasticity, elastic limit, elongation, proportional limit, and tensile strength, yield strength and other tensile properties. In the present investigation all the tensile tests were conducted as per ISO test procedure. The tests were conducted on 100 kN servo hydraulic UTM machine under different strain rates under displacement mode of control. All measurements were performed at ambient conditions (23±2 0C and 50-60% RH, relative humidity). The displacement of cross head is taken as 1 mm/min.

### 4.3. Flexural strength

Flexural strength is the ability of composite material to withstand bending forces applied perpendicular to its longitudinal axis. Three point bending tests were performed for characterizing flexural property of composite material. A small of rectangular cross section was placed on two supports. A displacement was applied at the centre with cross head speed of 1 mm/min and the resulting force was recorded. This test was performed on a universal testing machine (UTM).

The span was taken 40 mm to measure flexural strength. The stress-strain curves were calculated using a linear elastic approach. Because of application of load at three points it is known as three point bending test.

Sample size 60x10x10 $mm^3$ and span length= 40 mm.

Formulae used for calculation: Flexural stress

$= 3PL/2bd^2$

Where P= load at given point (N), L= support, b=width (mm), d=depth (mm)

## 5. Results and Discussions

### 5.1. Microscopic investigation

In this investigation SEM was carried out on coconut based composite containing different weight percentage of shell particle and coir fiber to evaluate matrix interface and dispersion of the particle and coir fiber in the epoxy resin matrix. SEM was done on 10000 times magnification factor and 1000 times magnification factor. The state of dispersion of coconut shell particles and coir fibre into the resin matrix plays a significant role on the mechanical properties of the composite.

Figure 2 & 3 shows the SEM photographs of different shell particle composite material investigated in the present work. The absence of any voids around the particle indicates a satisfactory adhesion between particle and epoxy matrix. The concentrations of shell powder are also seen in figures. From the above figures it is also evidence that there is no chemical reaction between shell powder and epoxy resin.

Hence, from the above micrographs it is can be concluded that due to somewhat uniform dispersion of coconut shell particle in the epoxy resin, a remarkably affect on the mechanical properties. Role of dispersion of particle and bonding/adhesion can be seen easily from SEM. A suitable coupling agent could improve adhesion and bonding among particles and coir fibre.

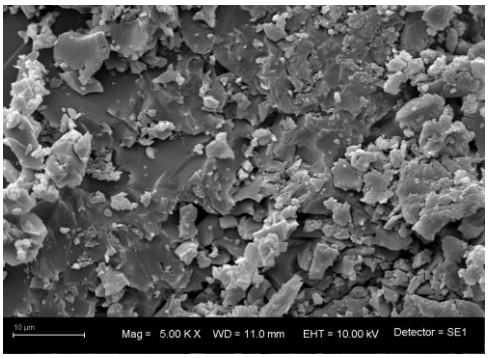


Figure 2(a). 18 wt% coconut shell particle & 2 wt% coir fibre reinforced composite.

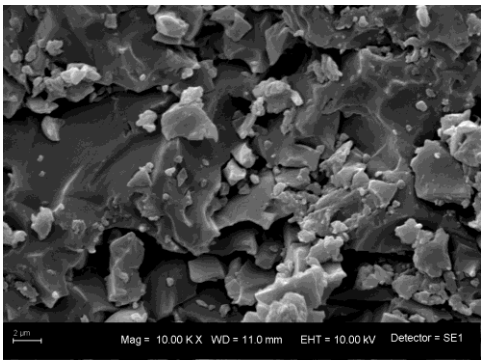


Figure 2(b). 17 wt% coconut shell particle & 3 wt% coir fibre reinforced composite.

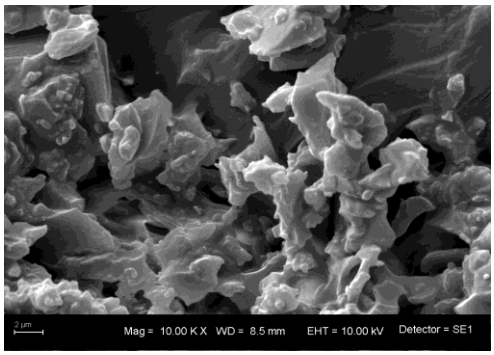


Figure 3(a). 28 wt% coconut shell particle & 2 wt% coir fibre reinforced composite

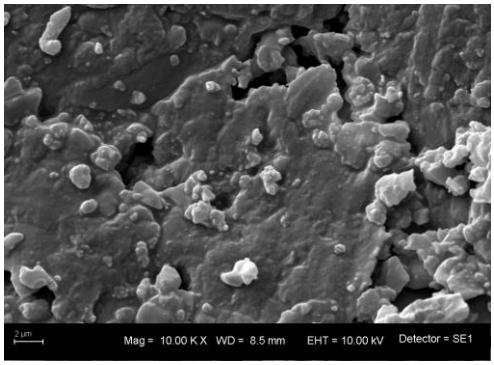


Figure 3(b). 27 wt% coconut shell particle & 3 wt% coir fibre reinforced composite

### 5.2. Tensile properties

The Mechanical properties of the natural fibre reinforced composites depend on several factors such as the stress-strain behaviors of fibre/particle and matrix phases, the phase volume fraction, the fiber concentration, the size of particles, the distribution and orientation of the fibre or fillers relative to one another.

Figure 4 shows the typical stress vs. strain curves for coconut shell particle and coir fibre reinforced composite. It can be seen that ultimate tensile strength decreases with coconut shell particle and increases with coir fiber when coir and shell particle used as reinforcement.

Sapuan [11, 12, 13] investigated that tensile properties (27-35 MPa) increases for coconut shell particle (50-200 µm) reinforced into epoxy upto 0-15 wt% and decrease beyond 15 wt% of reinforcement of shell particle.

The reinforcement used in this experiment was 20%wt shell particle & coir fibre that is more than 15 wt% used in Sapuan's experiment [11, 12, 13]. So, same fashions of decrement in the tensile properties were also observed for this range of reinforcement as given in table 1. Tensile strength of 35 MPa was retained even after 30 wt% reinforcement of shell particle and coir fibre. But it is quite appreciable when compared with tensile strength of 24.8-19.8 MPa and modulus of elasticity (633-318 MPa) of coir reinforced for 5-15 wt% polyster composite.

Stress strain diagram was plotted for shell particle and coir fibre in figure 4. A low stress level was observed in particle and coir fibre composite with 28 wt% particle & 2 wt% coir fibre and 27 wt% particle & 3 wt% coir fibre. Stress was maximum for 17 wt% of particle and 3 wt% of coir. Reduction in ultimate tensile strength due to shell article was compensated with coir fibre. Reduction in tensile strength with addition of particle would due to poor adhesion of particles of this bigger average size 0.200-0.800 mm. Reinforcement of fibre would be improving the adhesion or bonding strength among resin, shell particle and fibre. Finally 2-3 wt% fibre contributed to improve tensile strength as shown in figure 5.

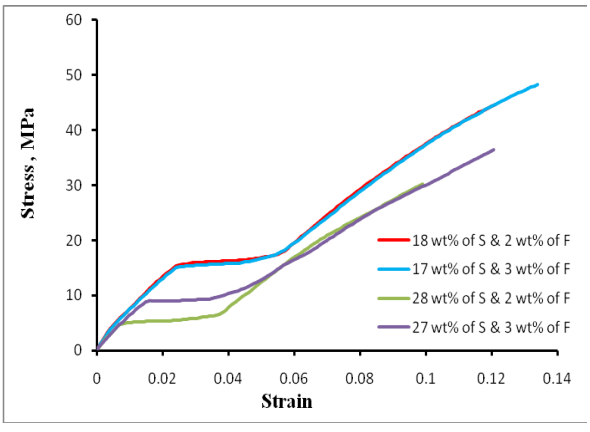


Figure 4. Stress-Strain diagram coconut shell particle and coir fiber reinforced composite

| S.No. | 20 wt% Reinforcement | | 20 wt% reinforcement | | 30 wt% reinforcement | | 30 wt% reinforcement | |
|---|---|---|---|---|---|---|---|---|
| | 18 wt% S | 2 wt% F | 17 wt% S | 3 wt% F | 28 wt% S | 2 wt% F | 27 wt% S | 3 wt% F |
| Ultimate tensile strength (MPa) | 44.59 | | 48.27 | | 30.20 | | 38.99 | |
| Modulus of elasticity (MPa) | 920.81 | | 848.53 | | 720.06 | | 684.93 | |
| Percentage elongation | 12.09 | | 13.39 | | 9.90 | | 13.06 | |

Table 1. Tensile Properties of coconut shell particle (S) and coir fibre (F) reinforced composite

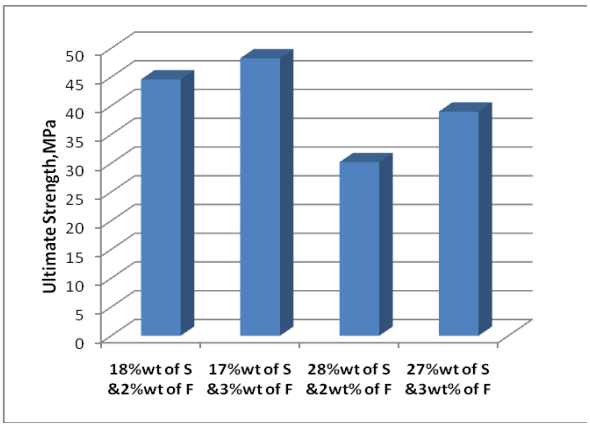


Figure 5. Variation of ultimate strength of coconut shell particle and coir fibre reinforced composite

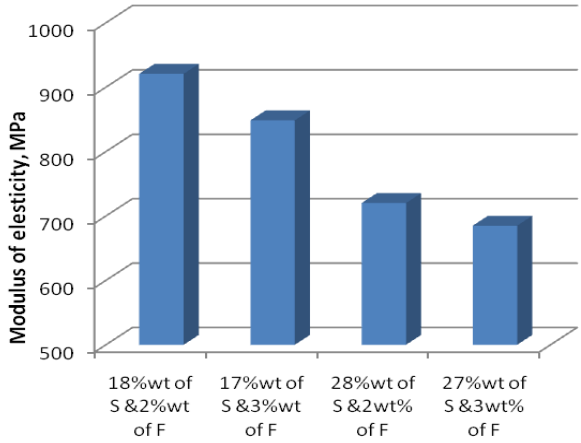


Figure 6. Variation of modulus of elasticity of coconut shell particle and coir fibre reinforced composite

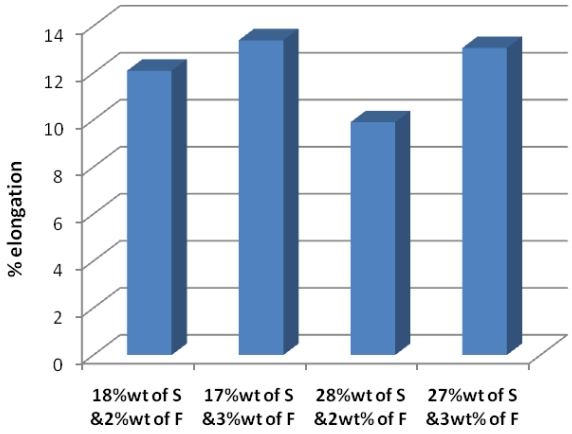


Figure 7. Variation of % elongation of coconut shell particle and coir fibre reinforced composite

Figure 6 & 7 shows that the variation of modulus of elasticity and percentage elongation with wt% of coconut shell particle and wt% coir fibre. Modulus of elasticity decreased with the increase in wt% of coir fibre and shell particle both. Fibre reinforcement reduces the modulus of elasticity more severely for only 1 wt% increase in wt% of coir from 2 wt % to 3 wt%. The lowest value modulus of elasticity was 650 MPa for 27 wt% of particle 3 wt% of coir. It was observed from figure 7 that percentage elongation showed same pattern of modulus of elasticity reflection.

### 5.3. Flexural strength

Flexural property of wood composite is very necessary for structural application to avoid failure. This property for tested composite is presented in table 2 and figure 8.

The role of coir and particle reinforcement in the resin matrix can be observed and shown in figure 8. The flexural strength was reduced for increasing the reinforcement of coir from 2 wt% to 3 wt%. But flexural strength was not affected

much more when wt% of particle was increased from 17 wt% to 27 wt%. 2 wt% of coir fibre is appropriate in view of flexural strength.

| S.No. | 20 wt% Reinforcement | | 20 wt% reinforcement | | 30 wt% reinforcement | | 30 wt% reinforcement | |
|---|---|---|---|---|---|---|---|---|
| | 18 wt% S | 2 wt% F | 17 wt% S | 3 wt% F | 28 wt% S | 2 wt% F | 27 wt% S | 3 wt% F |
| Flexural Strength (MPa) | 58.140 | | 51.048 | | 58.494 | | 44.910 | |

Table 2. Flexural strength for composites of coconut shell particle and coir fibre reinforced composite.

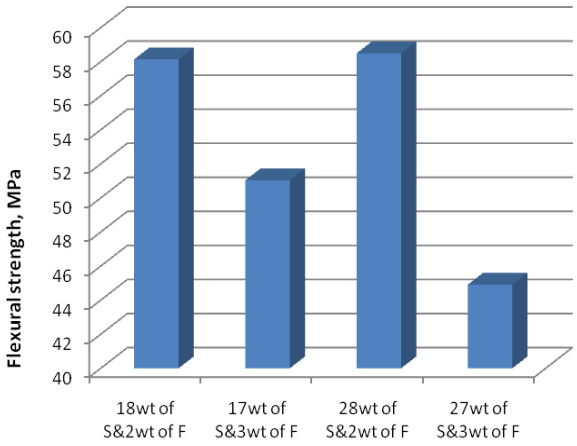


Figure 8. Flexural strength of shell particle and coir fibre reinforced composite.

## 6. Conclusions

The tensile and flexural properties of epoxy composite reinforced with coconut shell particle and coir fibre have studied and discussed here. A satisfactory dispersion of coconut shell particle and coir was observed. Disorder could be easily maintained by coupling agent. Ultimate tensile strength and percentage elongation increases with the increase of coir wt% and modulus of elasticity decreases with the reinforcement of shell particle and coir both. Flexural strength decreases with addition of coir fibre. The coconut shell particles and coir fibers are good reinforcing (30 wt%) material to reduce requirement of matrix material. The tensile and flexural properties this coir and shell particle based composite are found to be equivalent to other materials or composite used for structural applications. But there is a certain hope to improve tensile and flexural properties with the use of proper coupling agent.

## References

[1] M.P. Wolcott, K. Englund, A Technology Review of Wood-Plastic Composites 33rd International Particle board Composite Material Symposium, Washington State University Pullman, (1999) 103-111.

[2] S. Luo, A.N. Netravali, *Polymer composites* (1999) 20(3):367-378.

[3] E.M. Ahmed, B. Sahari, P. Pederson, Proceeding of World Engineering Congress 1999, Mechanical and Manufacturing Engineering, Kuala Lumpur (1999) 537-543.

[4] M.Y.A. Fuad, S. Rahmad, M.R. N.Azlan, Proceeding of the Fourth International Conference on Advances in Materials and Processing Technologies, Kuala Lumpur (1988) 268-271.

[5] J.P. Schneider, A.C. Karmaker, *Journal of material Science* (1999) 15:201-204.

[6] J. Bhaskar, S. Haq, A.K. Pandey, N. Srivastava, *Journal of Material & Environmental Science* (2012) 3(3):605-612.

[7] N. Ayrilmis, S. Jarusombuti, Fibers and Polymer (2011) 12(7):919-926.

[8] I.Z. Bujang, M.K. Awang, A.E. Islmail, Regional conference on Engineering Mathematics, Mechanics, manufacturing & Architecture (2007)185-201.

[9] V.K. Singh, P.C. Gope, *Journal of Reinforced Plastics and Composites* (2010) 29:2450-2468.

[10] A. Misra, V.K. Singh, Journal of IEI (2010) 91:21-24.

[11] S.M. Sapuan, M.A. Maleque, *The Arabian Journal for Science and Engineering*, (2003) 28:171-180.

[12] S.M. Sapuan, M. Harimi, M.A. Maleque, *Journal of Tropical Agriculture*, (2005) 43:1-2.

[13] S.M. Sapuan, M.N.M. Zan, E.S. Zainudin, P.R. Arora, *The Arabian Journal for Science and Engineering*, (2003), 28(2B).

Journal of New Technology and Materials
JNTM
Vol. 03, N°01 (2013) 56-60

OEB Univ. Publish. Co.

# Changes of thermal Conductivity, Optical Conductivity, and Electric Conductivity of Porous Silicon With Porosity

*Faten Alfeel*, Fowzi Awad, and Fadi Qamar*
**Department of Physics, Science Faculty, Damascus University, Syria*
*E-mail: fatenfeel@gmail.com*

*Received: November 10, 2012, revised: March 11, 2013, accepted: March 24, 2013*

***Abstract***

*Porous silicon (PS) was prepared by electrochemical etching method. Mirage effect in transverse photothermal deflection PTD ( skimming configuration) was used to determine thermal conductivity the experimental results of PS thermal conductivity was compared with theoretical results they were almost the same. Optical extinction coefficient and absorption coefficient were calculated from transmittance T and reflectance R curve which measured with UV-Vis-NIR Spectrophotometer, and they were used to calculate the optical conductivity and electric conductivity from the Shankar and Joseph equations, and optical conductivity and electric conductivity were studied with porosity in porous silicon.*

***Key words:*** *thermal conductivity, optical conductivity, electric conductivity, porous silicon, electrochemical etching, porosity, optical extinction coefficient , absorption coefficient , film.*

## 1. Introduction

Porous silicon has attracted considerable research interest after their discovery in 1956 [1]. Low-dimensional materials are finding ever-widening application in many areas of science and Engineering [2]. Nanostructured porous silicon shows a variety of other interesting properties, including tunable refractive index, tunable energy gap, low light absorption in the visible, high internal surface, variable surface chemistry, or high chemical reactivity. Properties, along with its ease of fabrication and the possibility of producing precisely controlled layered structures make this material adequate for its use in a wide range of fields, such as optics, micro- and optoelectronics, chemical sensing or biomedical applications [3].

## 2. Experimental Methods

Porous silicon samples were prepared by electrochemical etching method of p-type cubic silicon wafers (c-Si), (100) orientation with resistivity of 0.01-40 Ω·cm, electrochemical dissolution of Si wafers is used: HF-ethanol (measured by volume) aquas with concentration from 20% . The current density was always kept Constant for each sample during etching of PS (10,..,50 mA/cm2).Fabricating process done in a normal etching Teflon cell fig(1). After anodization, PS samples are carefully removed from the bath and cleaned in deionized water . Few examples of AFM measurement is presented to show differences between samples according to preparing current (fig.2).

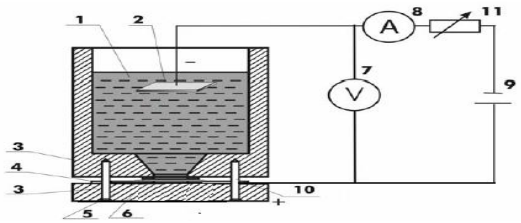


Figure 1. Iliustration of the experimental setup:
a) schematical view,
b) crossection of the electrochemical etching cell:
1 – electrolyte, 2 – copper cathod, 3 – electrochemical etching tank (teflon), 4 – platinum anode , 5 – seal, 6 – Si wafer, 7 – voltmeter, 8 – amperemeter, 9 – DC source, 10 – grips, 11 – rheostat [4].

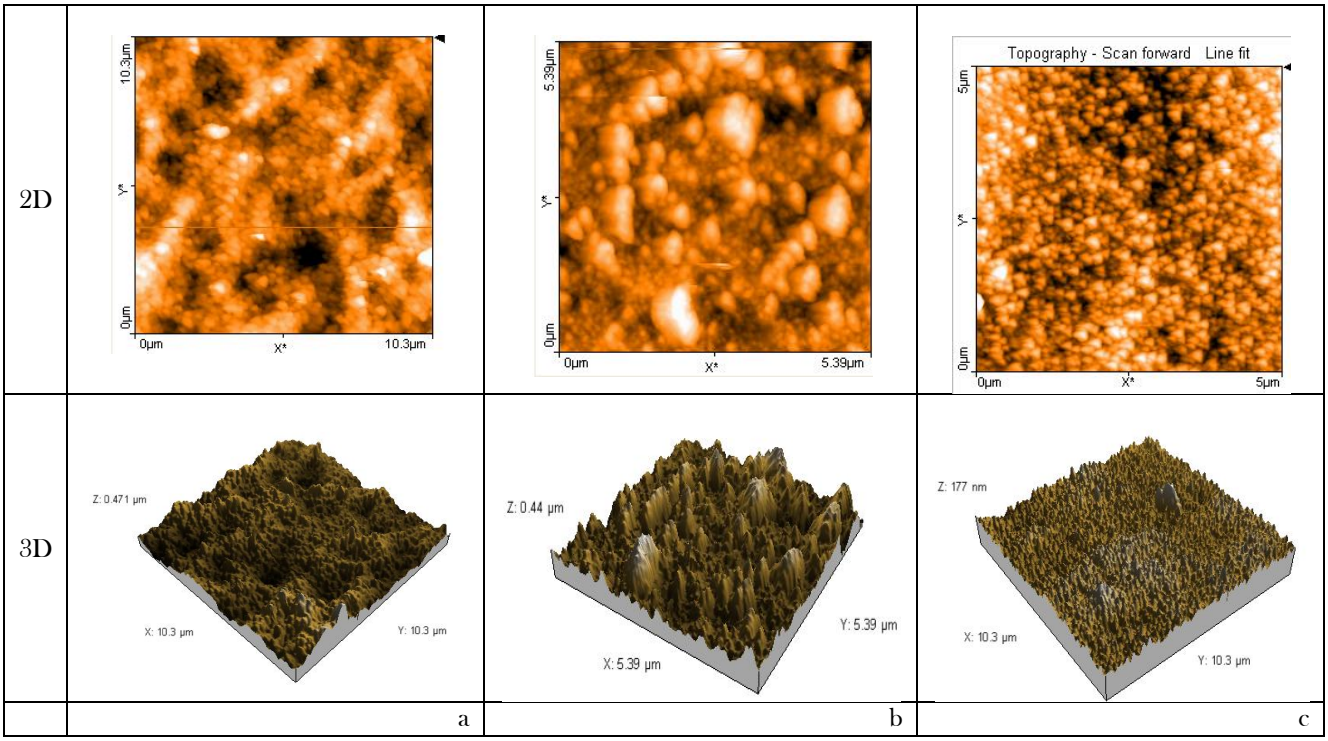


Figure 2. 2D and 3D AFM image of porous silicon samples prepared with etching time of 5 min and current density of (a-20,b-30,c-45) mA·cm$^{-2}$, at HF concentration 20%.

## 3. Theory

### 3.1 The porosity of porous silicon P

Porosity is defined as the fraction of void within the porous silicon PS layer and can be determined easily by weight measurements. The virgin wafer is first weighed before anodisation (m1), then just after anodisation (m2) and finally after dissolution of the whole porous layer in a molar KOH aqueous solution (m3).

$$P(\%) = \frac{m_1 - m_2}{m_1 - m_3} \tag{1}$$

the removal is made through a dip for some minutes in an aqueous solution of KOH (3% in volume), that leads to a selective removal of the PS layer without reacting with the bulk crystalline silicon.

Different techniques are employed to determine the porous layer thickness d. From the gravimetric measurements,

$$d = \frac{m_1 - m_3}{\rho S} \tag{2}$$

where ρ is the silicon density and S the etched surface [5].

### 3.2. Thermal conductivity

We've used transverse photothermal deflection PTD to determine thermal properties of PS, in skimming probe beam configuration [6, 7, 8, 9] fig.3

We've measured $\kappa_{eff}$ of the two layers Si-PS from PTD then by using two layers model, thermal conductivity of porous silicon film is calculated from eqs. (3, 4) [10]:

$$\kappa_{eff} = \frac{L\kappa_1\kappa_2}{\kappa_1 L_2 + \kappa_2 L_1} \tag{3}$$

$$\kappa_1 = \kappa_{eff}\frac{\kappa_2 L_1}{\kappa_2 L - \kappa_{eff} L_2} \tag{4}$$

Where $\kappa_1$ is thermal conductivity of porous silicon, $\kappa_2$ thermal conductivity of silicon (150w/mk) , $\kappa_{eff}$ the effective thermal conductivity(for porous silicon and silicon layer), $L_1$ the porous silicon film thickness, $L_2$ the silicon substrate thickness, $L$ thickness of porous silicon film and silicon substrate together(0.4 mm).

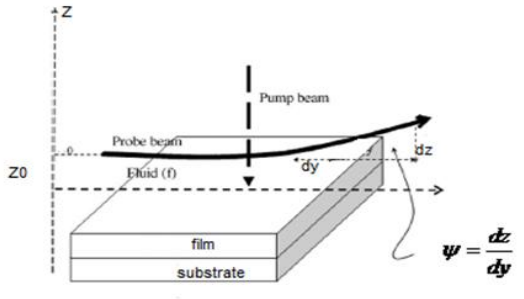


Figure3. schematic representation of the probe beam deflection in Skimming probe beam configuration

### 3.3. Optical conductivity measurement

As incident photon energy is given by : $E = h\nu$
Where $h$ is blank's constant, $\nu$ is the light frequency. The optical conductivity is directly proportional to optical extinction coefficient [11]:

$$k = \frac{\alpha\lambda}{4\pi} \quad (5)$$

$\lambda$ is the wavelength of light, $\alpha$ absorption coefficient which is calculated from transmittance T and reflectance R curve measured with UV-Vis-NIR Spectrophotometer[11]:

$$\alpha = (1/d)\ln((1-R)/T) \quad (6)$$

d film thickness.
and results were used to calculate the optical conductivity from the Shankar and Joseph equation [12]:

$$\sigma_{op} = \frac{k\,n\,c}{\lambda} \quad (7)$$

$k$ is the optical extinction coefficient, n is the optical refractive index, c is the velocity of light and l is the wavelength of light.

### 3.4. Electrical conductivity measurement

The electrical conductivity measurement using the Shankar and Joseph equation [12]:

$$\sigma_{ec} = \frac{2k\,c\,n}{\alpha} \quad (8)$$

### 4. Results and discussion

It was found that the Thermal conductivity of PS films decreases with increasing porosity. The measured thermal conductivities, of our samples was close to theoretical results predicted by Eq. (9) [13, 14].

$$\kappa_{1th} = \kappa_{si}(1-p)^3 \quad (9)$$

The decreasing in Thermal conductivity is attributed to that: The solid contribution is normally significantly higher than that of the gas contained in the pores, and thus, the gaseous conduction contribution is considered to be negligible. The radiative contribution, $k_{rad}$, is derived from heat radiated throughout the pores, and is highly dependent on the porosity, pore size, and temperature [15]. For all that reasons thermal conductivity in bulk silicon is higher than that of PS samples. fig(4) shows the measured and theoretical calculated thermal conductivity of PS sample they are almost the same.
$\alpha$ absorption coefficient which is calculated from transmittance T and reflectance R curve measured with UV-Vis-NIR Spectrophotometer fig.(5), using eq.(6). Then from $\alpha$ absorption coefficient the extinction coefficient $k$ is calculated from eq.(5), using $\alpha$ , $k$ optical conductivity is calculated then from eq.(7). Fig.(8), and electric conductivity is calculated from eq.(8),fig(9) ,our work shows that absorption coefficient and the extinction coefficient decreases with porosity increases.

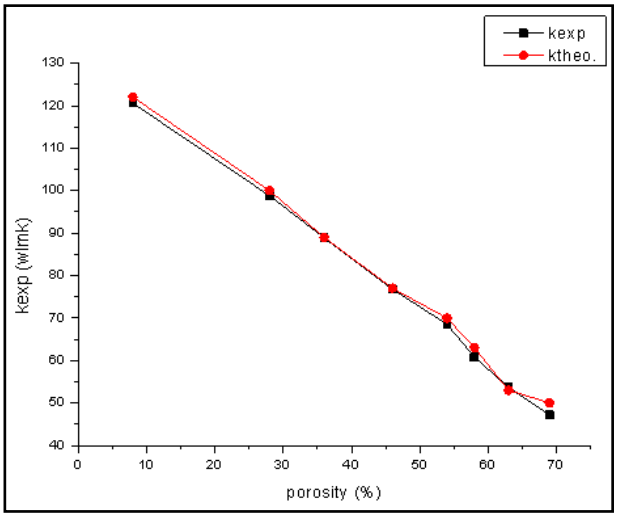


Figure4. the thermal conductivity of PS changes vs porosity

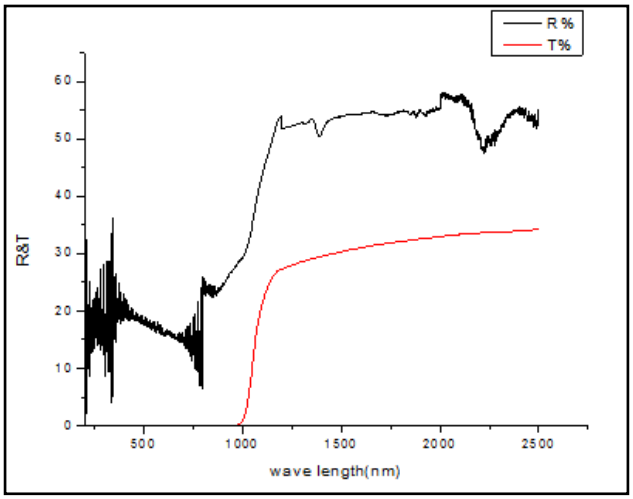


Fig.5 reflectance and transmittance as function of wave length for sample S01

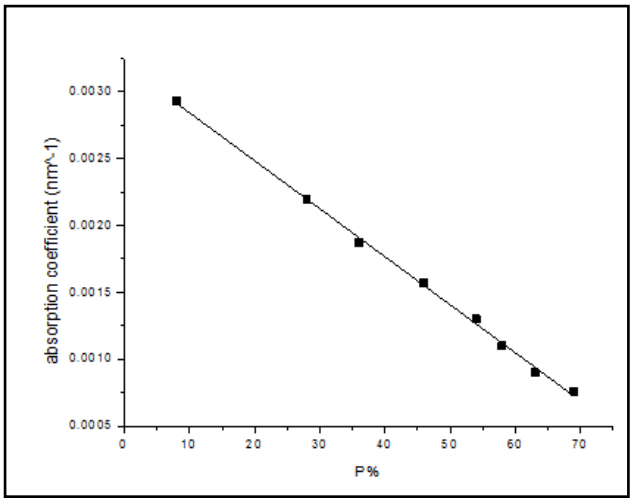


Figure 6. absorption coefficient vs. porosity

One can see that optical conductivity doesn't changes in our rang of porosity that means this is suitable material for optoelectric device . and that agrees with others results [11] where the variation of conductivity remains at zero up to photon energy of 5.35eV, while the electrical conductivity drops down because optical extinction coefficient decreases with porosity.

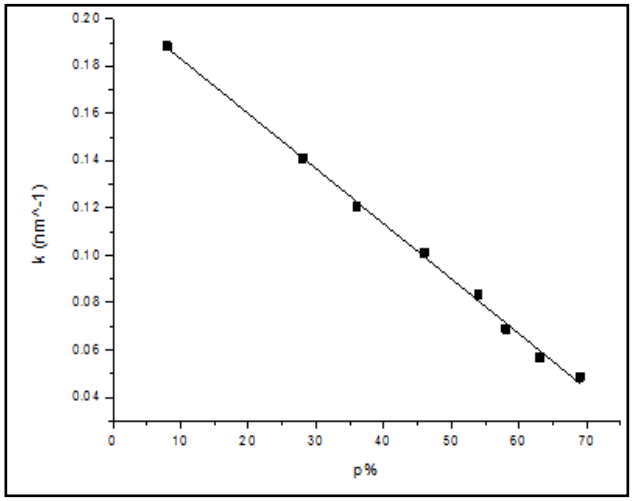


Figure7. Optical extinction coefficient vs. porosity

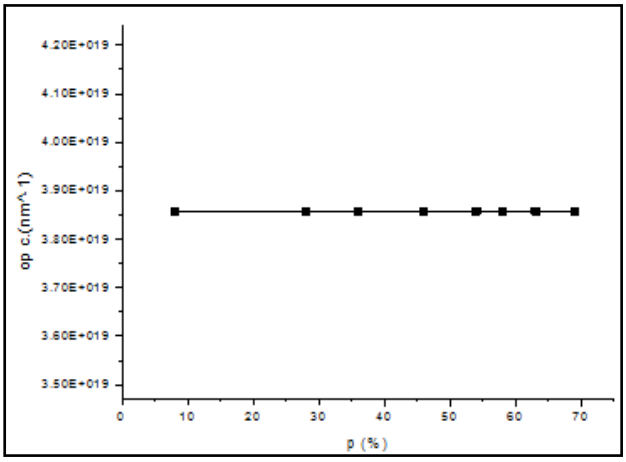


Figure 8. optical conductivity VS Porosity%

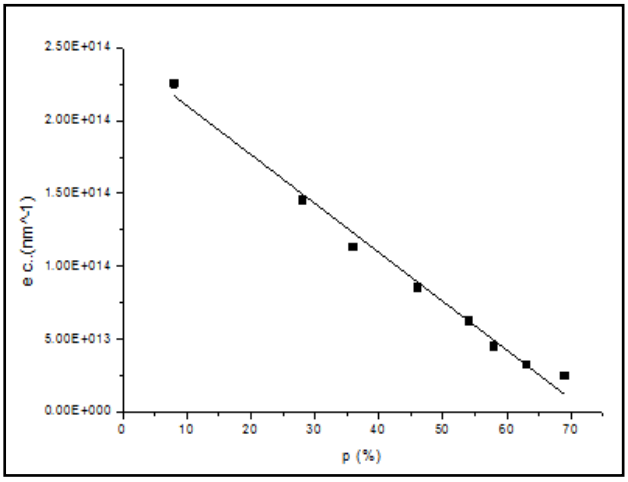


Figure 9. electric conductivity VS Porosity%

## 5. Conclusion

Porous silicon samples were prepared by electrochemical etching method , HF-ethanol concentration from 20% ,The current density was (10,..,50 mA/cm$^2$).Fabricating process done in a normal etching Teflon cell, Mirage effect in transverse photothermal deflection PTD ( skimming configuration) is used to determine effective thermal conductivity . It changed from120W/Mk for 8% porosity to 47.2 W/Mk for 69 % porosity. Experimental results of PS thermal conductivity with porosity was compared with theoretical results and it was almost the same . Absorption coefficient was calculated from transmittance T and reflectance R curve measured with UV-Vis-NIR Spectrophotometer was used to calculated extinction coefficient then to calculate electric conductivity and optical conductivity, our work shows that absorption coefficient and the extinction coefficient decreases with porosity increases. So is electric conductivity, while optical conductivity remains constant in rang of our porosity.

## References

[1] en.wikipedia.org/wiki/porous_silicon13/11/2011

[2] Gan'shina E. A., Kochneva M. Yu., and Podgorny D. A., (2005), Structure and Magneto-Optical Properties of Porous Silicon–Cobalt, Physics of the Solid State, Vol. 47, No. 7, p: 1383–1387.

[3] Torres-Costa v., Martý´n-Palma, R. J.,(2010), Application of nanostructured porous silicon in the field of optics. J. Mater Sci.Vo. 45, p: 2823–2838

[4] Jarimaviđūėžalionienė R., Grigaliūnas, V., Tamuleviđus,S., Guobienė A., (2003), Fabrication of Porous Silicon Microstructures using Electrochemical Etching. MATERIALS SCIENCE (MEDŽAGOTYRA). Vol. 9, No. 4,P:1392-1320

[5] Canham L., Malvern D.,(1997), Properties of Porous silicon. NSPEC, The Institution of Electrical Engineers, London, United Kingdom, p:18

[6] Nibu A.G. ,( 2012), Estimating the thermal properties of thin film and multilayer structures using photothermal deflection spectroscopy , Thesis submitted Presented to the in Partial Fulfillment of the Requirements for the Degree of Doctor of Philosophy, Faculty of the Graduate School of Cornell University .

[7] Beaudoin M., Chan I.C.W., Beaton D., Elouneg-Jamroz M., Tiedje T., Whitwick M. et.al, (2009), Bandedge absorption of GaAsN films measured by the photo- thermal deflection spectroscopy. Journal of Crystal Growth 311 : 1662–1665

[8] Jyotsna Ravi. J., Lekshmi S., Nair K.P.R., Rasheed T.M.A.,(2004) , A simple theoretical extension to the analysis of photothermal deflection signal for low thermal diffusivity evaluation . Jou.of Quan.Spect. & Radi. Transfer . 83 :193–202

[9] Jeona P.S., Kima J.H, Kimb H.J., Yoob J., (2008), Thermal conductivity measurement of anisotropic material using photothermal deflection method, Thermochimica Acta 477. 32–37

[10] Alvarez F. X., Jou D., Sellitto A., (2010), Pore-size dependence of the thermal conductivity of porous

silicon:A phonon hydrodynamic approach.APP. PH. LETTERS 97, P: 1-3

[11] Alfeel F., Awad F., Ibrahim Alghoraibi I., and Qamar F., (2012), Using AFM to Determine the Porosity in Porous Silicon. Journal of Materials Science and Engineering A 2 VO.9 P: 579-583

[12] G. Shankar G., Joseph P.S., YosuvaSuvakin M., and Sebastiyan A.,(2013), Optical reflectance, optical refractive index and optical band gap measurements of nonlinear optics for photonic applications, Optics Communications (2013)

[13] Shen Q, Toyodaa T., (2003), Dependence of thermal conductivity of porous silicon on porosity characterized by photoacoustic technique, Review of scientific instruments vol.74,NO.1, p:601-603.

[14] Wolf A. , Brendel R.,(2006), Thermal conductivity of sintered porous silicon films. Thin Solid Films 513.p:385–390.

[15] Pappacena K. E. , Faberw K. T., (2007), Thermal Conductivity of Porous Silicon Carbide Derived from Wood Precursors. J. A. C. S., Vol. 90, No. 9. 2855-2862